

DEVELOPMENT OF A GPS-BASED NAVIGATION AND GUIDANCE SYSTEM
FOR AN AUTOMATED GROUND VEHICLE

BY

MATHIEU JOERGER

Submitted in partial fulfillment of the
requirements for the degree of
Master of Science in Mechanical and Aerospace Engineering
in the Graduate College of the
Illinois Institute of Technology

Approved _____
Adviser

Chicago, Illinois
December 2002

ACKNOWLEDGEMENT

I surely owe my greatest thanks to my advisor, Professor Boris Pervan, for giving me the opportunity to work on this exciting project. Every piece of advice he provided resulted a flood of ideas which inspired what made the richness of this paper. His guidance and support have opened my eyes on numerous aspects of the engineer's life and I am sincerely eager to go on working under his supervision.

Then of course, I wish to express my gratitude to my lab colleagues, for their help, their support, and their availability. During those five months, F-C. Chang, I. Sayim, J. Christ, L. R. Gratton and M. B Heo proved to be not only great co-workers, but also priceless friends.

I am thankful to Pr. R. Dix, for his design advice and to Pr. S. Nair for his precious feedback on my work. A special thanks also to A. Plauchet, L. Ziaja, and J. Julius, who gave me the hardware needed to test the embedded computer.

I owe a debt to J. C. Berton and J. Sebastiao. Both have helped me in my researches, although their fields of study are different than mine. More importantly, they knew how to focus my attention on the way to success but brought the necessary distraction when needed.

My biggest debt is owed to Myriam, who I admire for her bravery as she kept on supporting me in spite of the 4,500 miles which separates us. Her daily (sometimes hourly) attention toward me is what carried me where I am.

Thanks to my family, who I know I can always count on.

TABLE OF CONTENTS

	Page
ACKNOWLEDGEMENT	iii
LIST OF TABLES	vi
LIST OF FIGURES	vii
ABSTRACT	x
CHAPTER	
I. INTRODUCTION	1
1.1 An Interdisciplinary Task	1
1.2 Historical Overview	2
1.3 Within the Scope of my Laboratory	3
II. BASELINE VEHICLE DESIGN	7
2.1 Setting Requirements	7
2.2 Choice of a general architecture	10
2.3 Hardware Selection and First Drawings	15
III. BASIC DYNAMIC MODEL	20
3.1 State Space Model for the Vehicle Only	20
3.2 Dynamic Model for the Motors	33
3.3 State Space Model for the Whole System Including Motors ..	39
3.4 Controllability, Observability and Stability	45
IV. NAVIGATION AND CONTROL	49
4.1 Introduction and Noise Modeling	49
4.2 Covariance Analysis for the Vehicle Only	57
4.3 Covariance Analysis for the Whole System including Motors	73
4.4 The Optimal Controller	78
4.5 Conclusion	84
VI. CONCLUSIONS AND PERSPECTIVES	87
5.1 Conclusions	87
5.2 Future Work	98
5.3 Closing	89

APPENDIX

A. SUPPLIERS' SPECIFICATION SHEETS	90
B. JOHN CHRIST'S DRAWINGS FOR THE VEHICLE	96
C. VERIFICATIONS OF THE DYNAMIC MODEL	100
BIBLIOGRAPHY	110

LIST OF TABLES

Table	Page
2.1 Spreadsheet Output for Design Selection using the AHP	14
2.2 Definition of Importance Ratings	14
2.3 Requirements and Achievements for the Embedded Computer	16
2.4 Leonard Specification Sheet (Courtesy of John Christ)	19
3.1 Notations for the Vehicle	21
3.2 Notations for the Motors	36
3.3 Notations for the Right and Left Motors	40
3.4 Values of the Quantities Describing the Model	45
4.1 Improvements Brought by the Encoders	77
4.2 Improvements Brought by a Lower Sample Time ($T_s=0.5s$ and $T_s=0.2s$)	82

LIST OF FIGURES

Figure	Page
1.1 The Global Positioning System (Left), the DGPS Technology (Right) ...	5
1.2 Helping Avoid Multi-Paths Disturbances	6
2.1 The Two Phases Necessary to Make Leonard Follow a Trajectory	8
2.2 General Scheme of an Engineered Servo-System	9
2.3 Main Parameters for “Car-like” (Left) and “Differential Drive” (Right) Designs	10
2.4 Applying the AHP to the Selection of a Design	13
2.5 Functional Scheme for Leonard	18
2.6 Side View of Leonard (Drawing Courtesy of John Christ)	19
3.1 Top View Representation of the Vehicle	22
3.2 Three-Dimensional Representation of the Vehicle	22
3.3 Free Body Diagram for the Vehicle	25
3.4 The Different Components of a DC Motor	35
3.5 Illustration of the System “Motor + Reducer + Load”	37
3.6 Electrical Representation of a DC Motor	38
3.7 Comparison and Stability Study for the Models With and Without Motors	46
3.8 Experimental Observations for Backward and Forward Motion	48
4.1 Process Noise Parameters Implied by the Non-Flatness of the Ground ...	53
4.2 Process Noise Parameters Implied by the Slip of a Wheel	54
4.3 Design through Controls, Optimized for Optimal Estimation	58
4.4 Conventions Used to Describe Leonard	59

Figure	Page
4.5 Convergence of the Covariance Propagation Process Over Time	60
4.6 States' Standard Deviations for Forward Motion (Vehicle Only)	62
4.7 States' Standard Deviations for Backward Motion (Vehicle Only)	63
4.8 Three Steps in the Propagation of the State Covariance Matrix	64
4.9 Four Cases for the Propagation of the State Covariance Matrix	66
4.10 Summary of Section 4.2.2.2: What Happens at the Singularity	67
4.11 Selection of the Location of the Center of Mass	69
4.12 Influence of S on the Cross Track Error for Different Positions of C	69
4.13 Three Dimensional Illustration of the Combined Influence of S and C ..	71
4.14 Different Perspective for the Figure 4.13	71
4.15 Cross Track Error vs. Position of S, for the Extreme Positions of C, for the Model With Torques as Inputs	72
4.16 Optimal Configuration for the System Without Motors	73
4.17 Cross Track Standard Deviation for the Best Configuration	73
4.18 Influence of the Location of the Center of Mass on the Poles of the System	75
4.19 Cross Track Error vs. Position of S, for the Extreme Positions of C, for the Model With Voltages as Inputs	76
4.20 Selection of the Encoder Based on its Resolution	78
4.21 Optimal Configuration for the Whole System	79
4.22 Final Results of the Covariance Analysis: Estimated Errors on Each State	80
4.23 Block Diagram of the Closed Loop-System	83
4.24 Results of the Closed-Loop Simulation Based on Lyapunov's Equations	84
4.25 Results of the Direct Closed-Loop Simulation, for $T_s=0.2s$	86

Figure	Page
4.26 General Method for Design through Controls	88
B.1 Leonard Assembly, Side View (Drawing Courtesy of John Christ)	99
B.2 Leonard Assembly, Top View (Drawing Courtesy of John Christ)	100
B.3 Leonard Assembly, Front View (Drawing Courtesy of John Christ)	101

ABSTRACT

Recent innovations in the Global Positioning System technology have enabled its use in the guidance of small mobile robots. Precision controlled Automatic Ground Vehicles (AGVs) can support a variety of highly-detailed missions that are unsafe or too difficult for human operation, such as the precise localization and removal of hazardous chemical, explosive, or radioactive waste.

“Leonard” is a prototype AGV, under development as part of this research, which uses a satellite-based navigation system as its primary sensor. The ongoing realization of Leonard serves as a benchmark example of the role of navigation and control system analysis in the identification and optimization of critical vehicle design parameters. In this regard, the vehicle pre-manufacturing phase is executed as a closed-loop design process to ensure the desired AGV dynamic performance.

In this work, a baseline differential-drive AGV architecture is established, and a dynamic model is derived for the resulting non-holonomic vehicle system (including motors). A linearized, state space representation of the dynamic model is then used as the basis to develop an AGV navigation and control system, which consists of a Kalman Filter and Linear Quadratic Regulator.

Detailed covariance analyses and closed-loop simulations are carried out to identify optimal operational values for critical vehicle design parameters. Ultimate predictions of the vehicle’s closed-loop dynamic performance are also obtained. Identified deficiencies with respect to required dynamic performance specifications are used to define and implement corrective changes in the baseline vehicle design.

CHAPTER I

INTRODUCTION

Finding valuable arguments to justify the selection of a design is one of the most hazardous tasks for the engineer if he fails to identify the critical parameters. The method proposed and illustrated in this paper helps pinpoint the decisive factors for a certain servo-system.

1.1 An Interdisciplinary Task

The motivation behind this work has multiple sources. Besides my laboratory's need for an experimental mobile platform, the application of navigation systems for automated outdoor ground vehicles with centimeter level accuracy is an attractive research area. Also, from an educational point of view, this project reveals a pertinent illustration of the use of control system analysis as a critical decision criteria for mechanical design.

“Leonard” is an Automated Ground Vehicle (AGV) which uses Global Positioning System (GPS) information to control its motion. The realization of its navigation system is organized in three steps.

To begin with, the necessary design choices have to be made so that the vehicle can be clearly pictured. Even though the purpose of this paper does not require exact quantitative dimensions for each mechanical feature, the existing alternatives are so numerous that the point must be reached where the first drawings can be established. This implies a lot of design decision making and several market surveys. These issues and Leonard's first drawings are presented in the second chapter.

Then, to get an understanding of the future behavior of the vehicle, a dynamic model is developed. The more accurate such a model is relative to the real device, the more robust the control system will be. Dynamic modeling for non-holonomic systems is an advanced task to which the third chapter is allocated.

Finally, modern control theory for Multiple Input, Multiple Output (MIMO) systems can be employed to achieve the ultimate goal of this paper: the development of a navigation system for the vehicle, presented in the fourth chapter. Analyses and simulations are carried out, the results of which are used to estimate the expected dynamic performance of the vehicle, even before it is manufactured.

These three steps are implemented in a closed loop design process. The last allows for the prediction of the behavior of the system which, if not satisfactory, can be modified by changing features in the first step.

Also, the analyses are carried out to a sufficient depth so that a clear understanding of the significant parameters which rule the system is acquired. This ensures a safe background to the manufacturing phase.

1.2 Historical Overview

Since the late 1980's, the tremendous improvements in computer science concerning embedded data processing have enabled efficient mobile robots in various industrial applications. One of the most relevant examples concerns AGV's following buried inductive wires, namely for the transport of materials in the automotive industry.

But there are many other fields where AGV's or ALV's (Autonomous Land Vehicles) can be useful. Their availability (they can operate 24 hours a day), safety considerations (for hazardous civil tasks for example) and the extreme conditions where they can operate open many opportunities for potential applications.

However, several important drawbacks still slow down the acceptance of outdoor vehicles as compared to indoor robots. Since the system must detect a wide variety of obstacles, it is difficult to find reliable enough sensors; in spite of important improvements in vision systems, the technology for outdoor robotics is still not mature enough [Han01]*. Then, the financial profitability is not ensured: the high cost of the equipment is often higher than the labor cost of a driver.

At the end of the 1990's, new GPS technologies enabled to achieve centimeter level accuracy in navigation systems. This innovation provided a revolutionary improvement in the efficiency of navigation systems for outdoor applications. Michael L. O'Connor was the first to implement these techniques for the guidance of an AGV, more precisely for the control of a tractor in order to perform agricultural tasks [O'C97]. With the improvements brought by Bell in 1999 [Bel99], their experiments lead to promising results making this area of study very attractive.

Potential applications of GPS navigation systems for land vehicles now include mine detection, topographic field mapping, ramming of ski runs or agricultural field plowing.

1.3 Within the Scope of my Laboratory

Within the framework of the Navigation and Guidance Laboratory of the Mechanical Materials, and Aerospace Engineering Department of the IIT, I was proposed to work on

* Corresponding to references in the Bibliography

the development of a Navigation and Control system for an Automated Ground Vehicle. The purpose of the lab is to advance the state of the art in navigation, mainly for GPS-based airborne applications. For the time being, the only navigation measurements available within the lab are from a fixed user. It will be useful to have a means to obtain experimental data from on a real moving device.

Therefore, the purpose of this work is to design an autonomous, mobile platform, whose navigation system would be based on GPS, but flexible enough to allow the addition of other sensors. For example, the navigation system could later be complemented with an inertial sensor to ensure navigation continuity when satellite signals are unavailable. Further projects also include synchronized tasks performed by several robots using GPS as the positioning sensor.

The GPS satellite navigation system is a tool which provides real time information about the position of the user (for example East-North-Up type of data). Compact and light receivers can be equipped on small rugged vehicles like Leonard. Basically, the position is estimated by evaluating the distance between the user and several satellites (Figure 1.1). For the purpose of this work, the details of the GPS sensor are not relevant, but a succinct presentation can help comprehension of this research.

The technology used to reach the critical centimeter level accuracy is called Carrier-Phase Differential GPS (CDGPS). In the past, it has been successfully employed in aerospace for landing of aircraft, but its first introduction into the world of AGV's dates from O'Connor's work referenced above [O'C97]. "Carrier-Phase" refers to the nature of the data analyzed. The Differential technique improves the measurements' accuracy

from tens of meters to centimeters [Mis99]. Basically, the correction is done by comparing the data received by the user to the ones at a reference station, situated at a fixed and known location close enough to the user (Figure 1.1). This correction eliminates various errors proper to the GPS signals and brings the necessary improvements to allow its use in a centimeter level real time navigation system. This is particularly important because it introduces the need of a (wireless) connection between the user and the reference station. This function is executed by a data link.

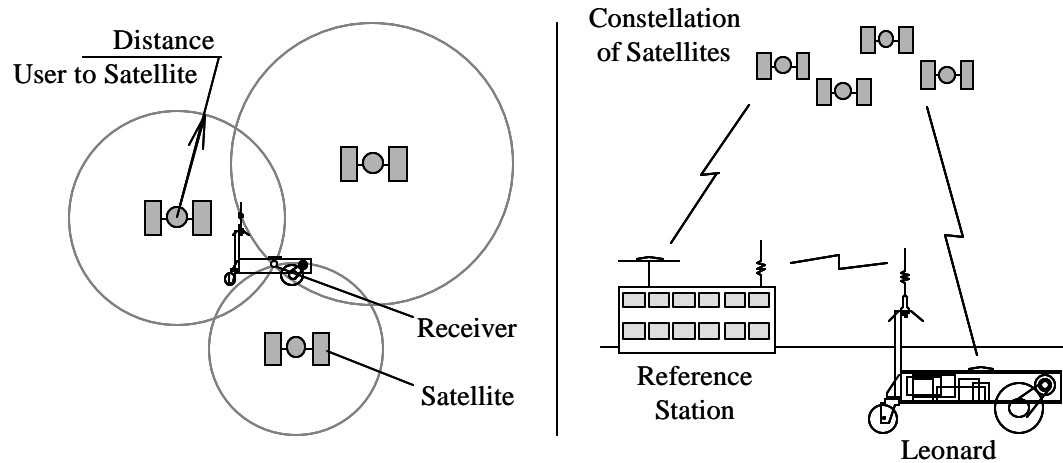


Figure 1.1. The Global Positioning System (Left), the DGPS Technology (Right)

In this work, it is assumed that the output of the GPS sensor is a two element vector whose elements are :

$$x_s \text{ and } y_s ,$$

defined in an inertial frame (East and North). These are given with a standard deviation

of :

$$\sigma_{\text{GPS}} \approx 2\text{cm} .$$

The GPS receiver tracking loop bandwidths limit the effective sample time such that:

$$T_s > 0.1\text{s} .$$

The last GPS feature of interest in this study is multipath. As illustrated in Figure 1.2, multipath is a source of ranging error, which happens when one signal comes to the receiver's antenna through different paths. Proper placement of the GPS antenna in the middle of a flat surface can mitigate this problem.

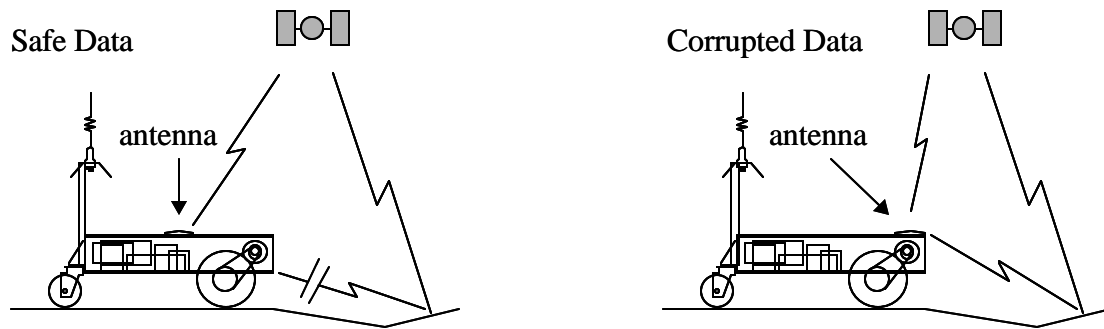


Figure 1.2. Helping Avoid Multipath Disturbances

The conception of the vehicle is spread into two parts: on the one hand, the manufacturing of the concrete device including most of the hardware issues which is performed by John Christ, whose contributions to this project will be detailed in an upcoming dissertation. In contrast, this work is focused on the creation of the navigation system and definition of key vehicle architectural elements to optimize navigation performance.

The fact that the hardware selection and the theoretical analysis are done in parallel results in an iterative process which allows for efficient results without wasting money in a trial and error process. Indeed, once a parameter is optimized through analysis, a market survey is performed to find the closest available device. But because industrial standards do not systematically meet our customized requirements, it is often necessary to iterate between what the analysis demands and what the industry can supply.

CHAPTER II

BASELINE VEHICLE DESIGN

The goal of this chapter is not to give a precisely detailed description of each part of the vehicle. It is intended to give sufficient qualitative and quantitative details about Leonard so that an accurate dynamic model can be derived (Chapter 3) and used in navigation and control system design (Chapter 4).

After introducing the objectives and requirements, an Analytical Hierarchy Process (AHP) helps choosing an appropriate design for the vehicle, especially for the steering system. Finally, the selected hardware and the current drawings are presented.

2.1 Setting Requirements

The main objective of this thesis is to develop a control system to have Leonard follow a desired trajectory. Note that this is performed without any obstacle detection device; such a system can be easily integrated later once the baseline navigation algorithms are built. As part of this study several critical vehicle design parameters are optimized based on error estimation techniques described in Chapter 4. In addition, the importance of the sense of motion, the position of the GPS antenna and the gain added by using encoders are also considered.

As mentioned before, what is meant when referring to a navigation system is a tool to have Leonard follow a predefined path (Figure 2.1). This consists in two steps: (1) the acquisition phase: Leonard must reach the path and orient itself into the right direction; (2) the regulation phase: Leonard must correct its trajectory in real time to remain as close as possible to the desired path. In this work, regulation is the principal focus.

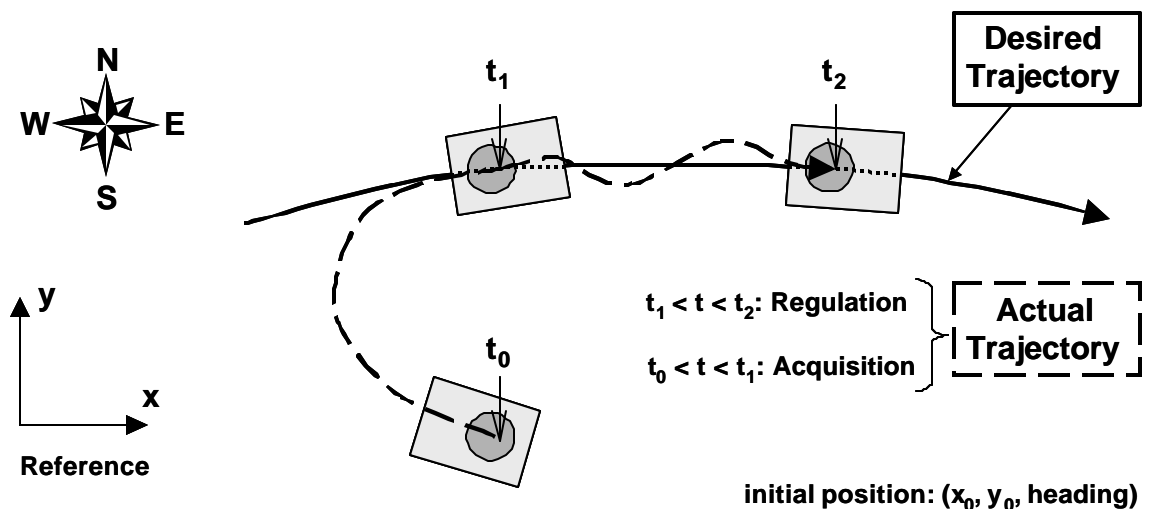


Figure 2.1. The Two Phases Necessary to Make Leonard Follow a Trajectory

Concerning the hardware, with no previous experience in building AGV's, the starting point is explained below.

First of all, Leonard must be a rugged ground vehicle, capable of performing on every type of outdoor terrain. Therefore, it can have three or four wheels, and should consist of a flexible platform, preferably oversized in order to accept the integration of additional equipment in the future. A motor may provide the mechanical energy allowing the motion of the vehicle, and the direction should be determined by a steering system. The nominal average speed has been set to be:

$$V_{y0} = 10 \text{ mph.}$$

An embedded computer is required, running under Linux (for compatibility with the GPS system's codes) for real time applications, with a flexible set of Input/Output ports. As mentioned before, the use of DGPS imposes the presence of a GPS receiver and of a data link. The antennas for those devices must be located on an unobstructed location (on top of Leonard). Appropriate interfaces have to be chosen.

The fact that Leonard is autonomous means that it has to carry its own power supply. A battery should provide power for both the computer and the actuators. It should last at least two to four hours of operating time.

Of course, size and weight may be the most constraining factors in the choice of each mechanical element.

All these components fit into the general representation for an engineered servo-system (Figure 2.2.): in this case, the actuators are the motors, the control system is the embedded computer, the sensors are the GPS system plus possibly either tachometers or encoders, the interfaces are relays and Digital to Analog converters connecting the computer and the other elements.

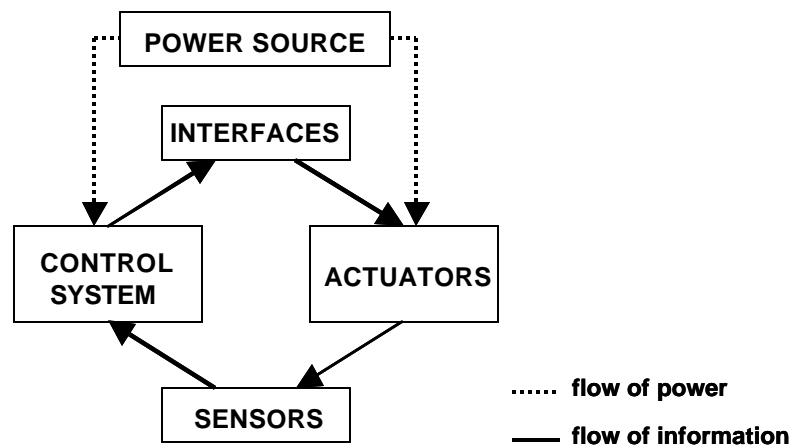


Figure 2.2. General Scheme of an Engineered Servo-System

Now that the main components have been summarized, the general vehicle design should be defined. This is the subject of the following section.

2.2 Choice of a General Architecture

There is a tremendous amount of literature concerning AGV's and ALV's. Two preferred designs are quickly selected: (1) the "car-like" design and (2) the differential-drive design. The main difference between these two options is the steering system (Figure 2.3).

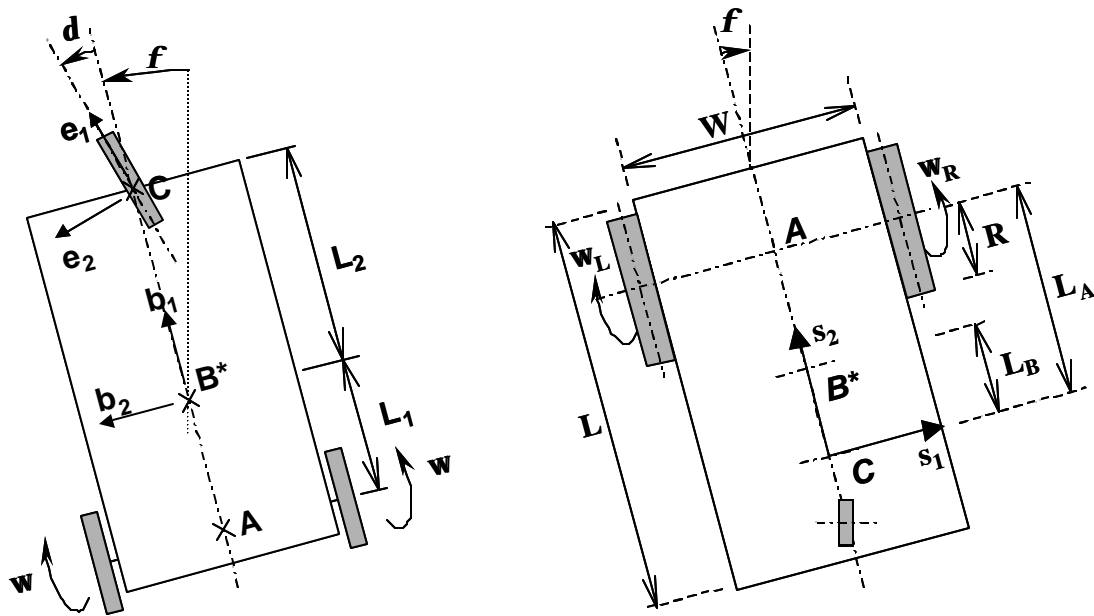


Figure 2.3. Main Parameters for "Car-like" (Left) and "Differential Drive" (Right) Designs

On the one hand, the steering system for "car-like" vehicles is based on the vertical rotation of one of the axles (like a car). Many issues are to be considered. They are listed succinctly below:

- The steering and the generation of motion are each performed on a separate axle.
- There must be different actuators for the steering and the generation of motion.
- Front or rear wheel drive must be chosen.

- Controlling the steering (vertical rotation of wheels) is easier when using only one wheel instead of an axle with a wheel at each end. The bulk is much smaller, but the stability of the vehicle is decreased.
- The steering requires a linear actuator or a system transforming rotational motion into linear motion.
- For adherence purposes, a differential may be necessary on the driving wheels' axle.

This is the type of vehicle used by O'Connor [O'C97]. Not choosing this design means putting more efforts into the dynamic modeling since the benefit of O'Connor's experience would be lost.

On the other hand, the steering system for "differential drive" vehicles is based on the difference in angular velocity between the two driving wheels (like a wheel chair or a supermarket cart). Elementary realizations of AGV's are usually done with this kind of vehicle because the design is much simpler. None of the preceding issues need to be considered. One axle is composed of two independently driven wheels while the other consists of a floating caster. In addition, differential drive vehicles are known to be better adapted to rugged terrains, and the zero-angle turn capability can be useful for about-turns in restrained spaces.

Though this system seems to win on all aspects, no documentation concerning GPS-based navigation of such a vehicle is available to our knowledge.

Thus, a design conflict exists between mechanical simplicity and controls uncertainty. To help guide this choice, Design Engineering provides a tool called the Analytic Hierarchy Process (AHP) [Slo92]. It is particularly valuable with complex, unstructured problems.

The AHP is a three-step method: (1) break down a complex choice by identifying its different parameters at several levels; (2) allocate relative importance to each parameter and goodness of each alternative toward the last level's parameters; (3) apply the calculations of normalized priorities to get the normalized overall goodness for each alternative.

First, the AHP model is set up (Figure 2.4): the first level is the selection of the design which is distributed into three factors at the second level: the dynamics and controls of the vehicle, the mechanics, and the cost. Sub-factors are identified in the third level. The dynamics are divided into the experience and innovation aspects; the experience corresponds to the amount of literature available for each alternative; the innovation stands for the challenge implied by the alternative and for the extent to which there might be an innovative gain. The ruggedness and stability provided by the design, its complexity (number of parts, assembly, number of issues to tackle), and the bulk of its steering system are the mechanical factors. The costs in terms of money and of time are finally underlined.

Secondly, the importance of each factor at each level is determined (Table 2.1) based on the importance ratings listed in the Table 2.2. For consistency purposes, once an importance rating is fixed between two parameters, its counterpart is its inverse (for more details, refer to [Slo92]). In Leonard's case, at the second level, the main trends are that

less value is given to the costs and that the mechanics is the priority. At the third level, the tendencies are less sharp, but still, in the dynamics part, experience is considered more important than the potential innovative profit. Goodness ratings are allocated to translate the fact that one design is better than the other with respect to a given parameter. Accordingly to the previous statements, the car-like design is better from a controls point of view whereas the differential drive design has most of the mechanical advantages.

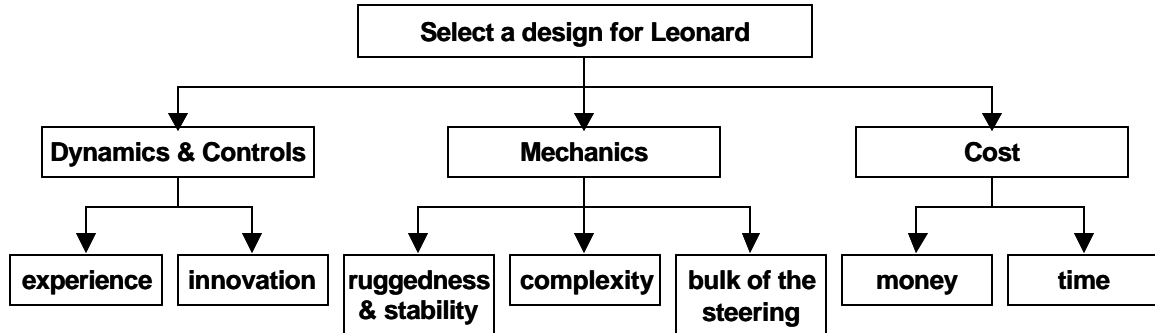


Figure 2.4. Applying the AHP to the Selection of a Design

Thirdly, the priorities are calculated and normalized, and the normalized weight of each last level's parameter is estimated. The overall goodness is deduced: as a result, the differential drive looks twice as good as the car-like type of design (Table 2.1, two last rows of the last column).

For this reason, a differential drive type of design is selected as the basis for Leonard.

Table 2.1. Spreadsheet Output for Design Selection Using the AHP

	Dyn/ Ctrl	Mechanics	Cost	Priority	N. Prior		Level 2
Dyn. & Ctrl	1.000	0.200	5.000	1.000	0.161		
Mechanics	5.000	1.000	25.000	5.000	0.806		
Cost	0.200	0.040	1.000	0.200	0.032		
Sum	6.200	1.240	31.000	6.200	1.000		

	Experience	Innovation	Priority	N. Prior	N. Wght		Level 3
Dyn. & Ctrl	1.000	7.000	2.646	0.875	0.141		
Experience	1.000	7.000	2.646	0.875	0.141		
Innovation	0.143	1.000	0.378	0.125	0.020		
Sum	1.143	8.000	3.024	1.000	0.161		

	Rug/ Stab	Complexity	Bulk	Priority	N. Prior	N. Wght		Level 3
Mechanics	1.000	2.000	3.000	1.817	0.545	0.440		
Rug & Stab	1.000	2.000	3.000	1.817	0.545	0.440		
Complexity	0.500	1.000	1.500	0.909	0.273	0.220		
Bulk	0.333	0.667	1.000	0.606	0.182	0.147		
Sum	1.833	3.667	5.500	3.331	1.000	0.806		

	Time	Money	Priority	N. Prior	N. Wght		Level 3
Cost	1.000	0.250	0.500	0.200	0.006		
Time	1.000	0.250	0.500	0.200	0.006		
Money	4.000	1.000	2.000	0.800	0.026		
Sum	5.000	1.250	2.500	1.000	0.032		

	Experience	Innovation	Rug/ Stab	Complexity	Bulk	Time	Money	Goodness	Norm. Overall
Design comparison									
car-like	9.000	3.000	3.000	1.000	1.000	3.000	1.000	3.062	0.324
differential	3.000	5.000	7.000	9.000	5.000	1.000	3.000	6.400	0.676

Table 2.2. Definition of Importance Ratings

Importance	Definition
1	equal importance
3	a little more important
5	more important
7	much more important
9	absolute importance

2.3 Hardware Selection And First Drawings

The information in this section may be subject to change once the manufacturing process is launched. However, at this point of the project, analyses have already been performed and market surveys have lead to the purchase of most of the elements. Therefore, the features presented here are likely to be very close to the final selections.

Appendix A contains the specification sheets for the motor and its encoders. These are used to apply numerical values to the model derived next chapter. John Christ's drawings are presented in the Appendix B. To help follow the review of the components, the Figure 2.5 shows a functional representation of the system.

To select the on-board computer for the AGV, a market survey was performed in order to find an integrated unit meeting all of our requirements (Table 2.3). The most constraining factors appeared to be the followings: (1) the size, (2) the number of I/O ports (Input/Output), (3) the power requirements which is a DC voltage, (4) the ruggedness, (5) the compatibility with Linux. One product appeared to be the most appropriate: the SC415PDC-C533-6S from the Canadian supplier SmallPC. A market research also revealed that it was cheaper and safer to get expansions cards integrated by the supplier directly.

The requirement of 10mph for the nominal vehicle speed was quite ambitious compared to other first projects in the literature. Therefore, the choice of the motors was certainly not an easy task. Moreover, their dimensions depend on the weight of the vehicle and determine the choice of the batteries. These batteries are, in turn, the heaviest parts of the vehicle. A careful iterative design process performed by John Christ resulted in the selection of the motor: C40-A-400-E from Magmotor (Appendix A).

Table 2.3. Requirements and Achievements for the Embedded Computer

Part	Characteristics	Requirements	SC415PDC
Processor	Type	PIII or Celeron	Celeron
	Speed (MHz)	>300	533
Memory	RAM (MB)	64	64(SDRAM)
	Flash Memory (MB)		
Drives	Hard Drive Capacity (GB)	10	10
	Other Drives	IDE slot (CD)	floppy/CD
I/O Interfaces	Ethernet	1	1
	Parallel Ports	1	1
	RS232	6	2 + 4 (PCI)
	RS422		
	RS485		
	USB		2
	VGA interface (supports)	1	1
	Keyboard int.	1	1
Expansion	Mouse	1	1
	Other		Sound
	ISA		
	PCI	1	2 1/2-size
	ISA/PCI shared		
	PCMCIA		
	PC/104 (PC/104 plus, EBX)		
	Other		
Power Supply	DC Power Supply	#12V or 24VDC	10-30VDC
	AC Power Supply		
Operating System		Linux	None
Features	Shielding	rugged	Panelmount
	Weighth (lbs)		
	Dimensions	200*300*100	203*216*89
Environment	Operating Temperature (C)	10-30	
	Operating Humidity (%)	20-80	

These motors are linked to the wheels through pulley-and-belt reducers with a ratio of 3.2727:1. They are also delivered with encoders: the M21 from Dynapar (Appendix A) with a resolution of 1000 PPR (pulses per revolution). The resolution has been selected according to the covariance analysis presented Chapter 4. The other primary sensor is composed of a GPS receiver (Pro Pak II from Novatel) and a data link (DGR-15W from FreeWave) and their respective antennas, both already existing in the Navigation Lab.

The two sensors (DGPS and encoders) have a digital signal as outputs so that no separate Analog to Digital Converter is needed. On the other hand, since the computer is not capable of supplying the necessary current to run the motors, a Digital to Analog Converter (DA C) is needed. It will be connected on the power supply, the computer, and the motors, so that when the computer sends a signal, the converter allows the necessary current from the batteries to go to the motors. This function is performed by the speed controller also selected by John Christ (65E40 from DartControls). This device also prevents current peaks due to accelerations in the motors.

The power needed is 24V DC with an estimated nominal total current draw of 16.2 Amperes. Two 12 V DC batteries were chosen instead of one of 24V DC because 12V battery chargers are more commonly available.

Finally, the structure of the vehicle is made of standard aluminum beams and enclosed with aluminum plates, allowing the antennas to be outside, but all other elements are protected from dust and humidity within a rugged box. Two floating casters are added to ensure stability. Analyses described in detail in Chapter 4 reveal that the optimal location of the GPS antenna, for which navigation errors are minimized, is the

middle of the top plate. This is a double advantage since this location avoids multipath effects, an important source of noise for GPS measurements (Figure 1.2).

All these components are summarized in Figure 2.5 and Leonard's specifications are listed in the Table 2.4. Vehicle design plans (courtesy of John Christ) are presented in Appendix B and Figure 2.6 (a side view of the vehicle).

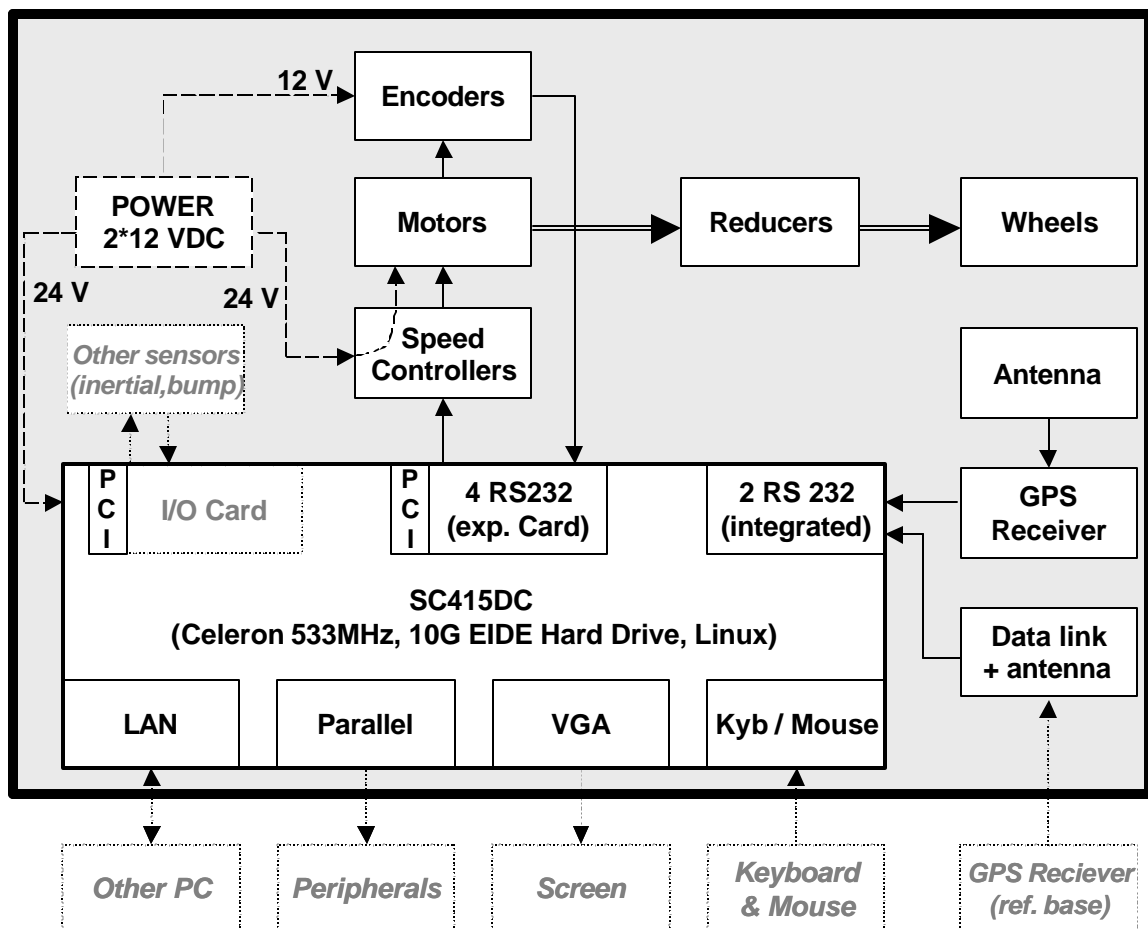


Figure 2.5. Functional Scheme for Leonard

Table 2.4. Leonard Specification Sheet (Courtesy of John Christ)

Feature	Value	Units
Top Speed	9.74	mph
Acceleration	1.467	ft/sec
Maximum Incline	15	degrees
Motor Torque	2480	in-oz
Drive Wheel	10	inches
Maximum Current Draw	80	amps DC
Operating Voltage	24	volts DC
Time Between charging	3.45	hours
Weight	182	pounds
Construction	Solid aluminum	
Dimensions	24 inches X 32 inches	

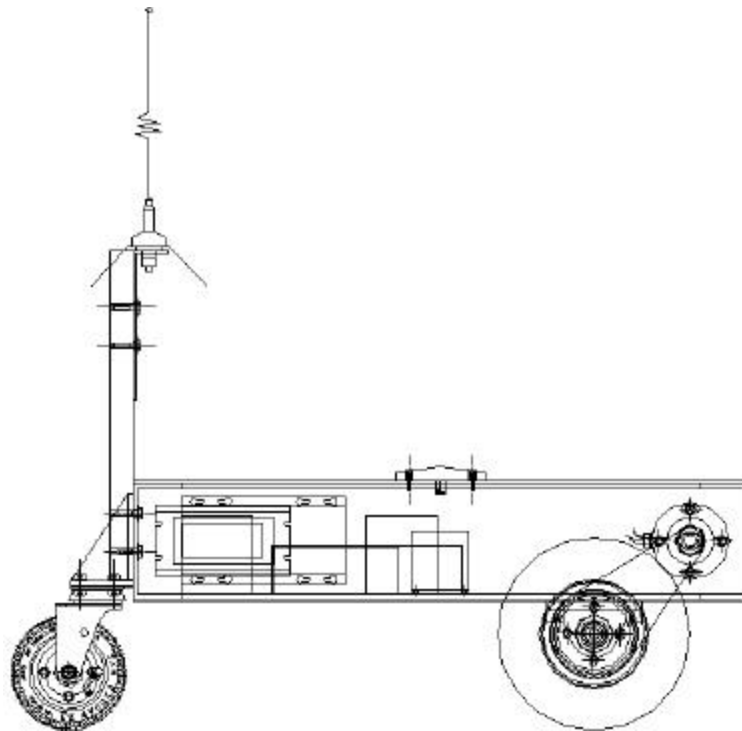


Figure 2.6. Side View of Leonard (Drawing Courtesy of John Christ)

CHAPTER III

BASIC DYNAMIC MODEL

Typically, kinematic equations are adopted for non-holonomic systems like this differential drive vehicle, because the final navigation system is usually sufficiently accurate [Pap00]. But with no previous empirical data when using GPS, we can not assume a-priori that a kinematic model is sufficient. In this regard, a full dynamic model is developed.

The vehicle's state space representation is actually derived in three steps: (1) the model for the vehicle only, (2) the model for the DC motors, (3) the state space representation for the whole system. A fourth part introduces the first analytical observations about these models.

3.1 State Space Model for the Vehicle Only

The first model assumes that the motors can be controlled by providing information about the resisting torque on the driving wheels. The sensors' outputs are the GPS measurements and the angular velocities of the wheels.

In order to build a state space model, the equations must be derived in terms of position and orientation state variables. In a first attempt to build and control the vehicle, it is assumed that Leonard runs on a flat horizontal surface. The non-flatness of the ground will later be explicitly considered as a source of process noise (Section 4.1).

Then, for the vehicle itself, it is assumed that: (1) the wheels are massless disks, (2) the wheels roll without slip (this assumption will also be relaxed via process noise), (3) the casters are perfectly floating, (3) the body of the vehicle can be modeled as a

rectangular parallelepiped with a uniformly distributed mass (the moment of inertia can later be modified with experimental data). The Figures 3.1 and 3.2 should help visualize the system. The Table 3.1 defines the relevant notations. In this analysis, Leonard is called “rigid body B”.

Table 3.1. Notations for the Vehicle

Notations	Definition
<i>Frames and Points:</i>	
{I}	the inertial frame: $(\vec{i}_1, \vec{i}_2, \vec{i}_3)$
{S}	the body frame, attached to the body B (Leonard): $(\vec{s}_1, \vec{s}_2, \vec{s}_3)$
B*	the center of mass of the rigid body B
A	intersection between the wheels’ axis and the axis of symmetry of the body B
C	the control point: we want this point to follow the predefined trajectory
S	the sensor point is the point where the GPS antenna is located
A _L and A _R	the centers of respectively the left and right wheels
<i>Lengths and Angles:</i>	
L	the length of the body B
W	the width of the body B
R	the radius of the front wheels
L _A	the signed distance from point C to point A
L _B	the signed distance from point C to point B*
L _S	the signed distance from point C to point S
ϕ	the heading angle
ω_R and ω_L	the angular rates of respectively the right and left wheels
J _{zz}	the moment of inertia of the body B at point B* about i_3
J _A	the moment of inertia of the body B at point A about i_3
<i>Magnitude of Forces</i>	
F _R and F _L	the forces exerted by the ground in the s_2 direction respectively on the right and left wheels
F _{NR} and F _{NL}	the forces exerted by the ground in the s_1 direction respectively on the right and left wheels, also called “constraint forces”

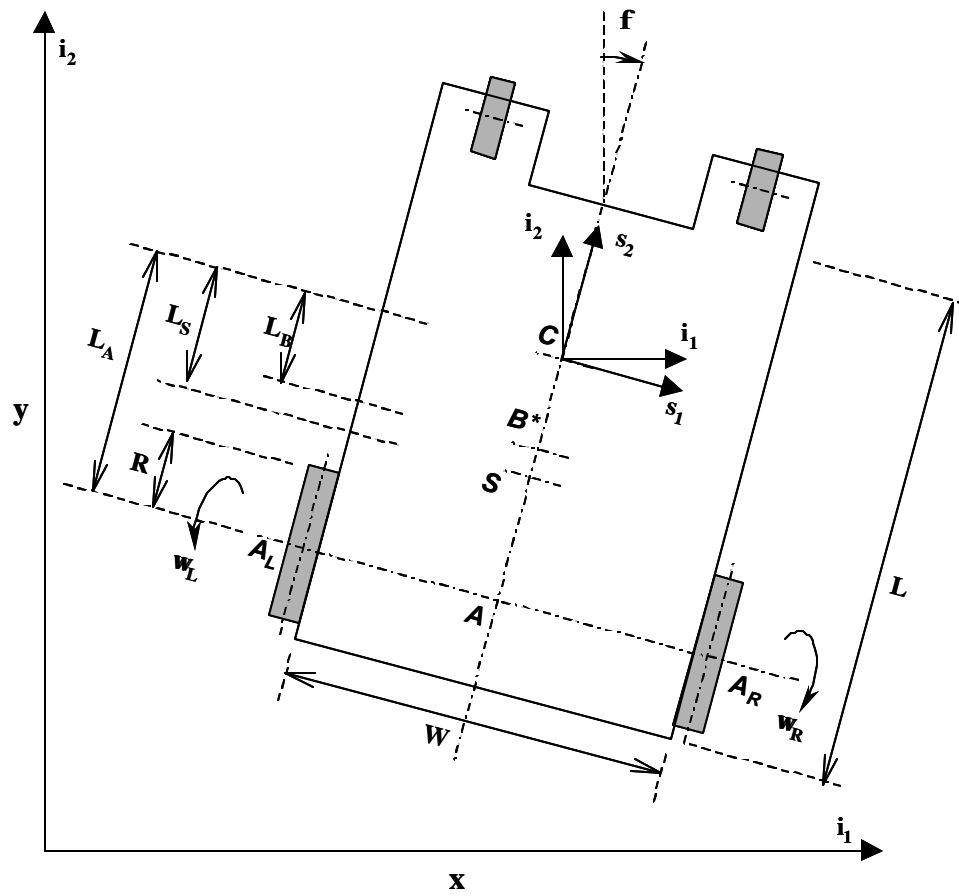


Figure 3.1. Top View Representation of the Vehicle

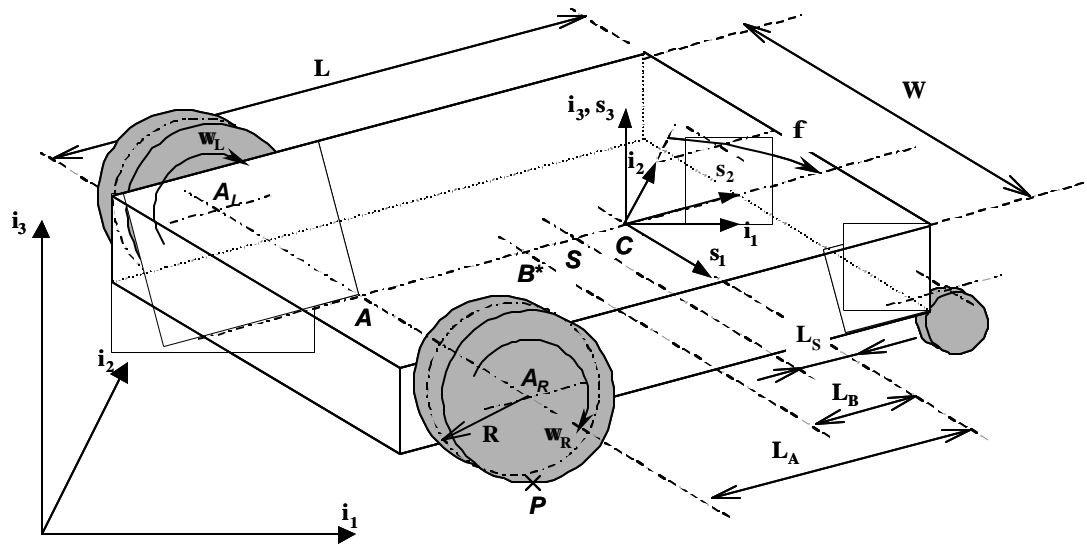


Figure 3.2. Three-Dimensional Representation of the Vehicle

Note that there are three distinct points of interest on the vehicle:

- the point C, called *control point*, is the point on the vehicle which should track the specified trajectory. Its position projected on \hat{i}_1 and \hat{i}_2 is defined respectively by x and y. This point can be subject to change from task to task, unlike points S and B* which are fixed once chosen.
- The point S, called *sensor point*, indicates the location of the GPS antenna. Its position projected on \hat{i}_1 and \hat{i}_2 is defined respectively by x_S and y_S .
- The point B* is the center of mass of the vehicle. Given the previous assumptions, it is located in the middle of the parallelepiped B.

3.1.1 Dynamic Model. In this first part of the dynamic analysis, the equations of motion for the model presented above are derived with the Newton-Euler method. The results are confirmed using Lagrange's and Kane's methods in Appendix C. Four steps are necessary to Newton's method; (1) we need to establish kinematic relationships (2) to estimate the forces and momentum, (3) and to derive the Newton-Euler equations of motion and (4) the constraint equations.

3.1.1.1 Kinematics. The use of Newton's laws requires knowledge of velocities and accelerations at different points:

- the velocity of the center of mass B* of Leonard with respect to the inertial frame {I} and expressed in the body frame {S} coordinates:

$${}^I\overline{\mathbf{V}}^{B^*} = {}^I\overline{\mathbf{V}}^S + {}^I\overline{\boldsymbol{\omega}}^B \wedge \overline{\mathbf{S}}B^* = \dot{x}_1\overline{\mathbf{i}}_1 + \dot{y}_1\overline{\mathbf{i}}_2 + \left(-\dot{\phi}L_B\right)\left(\overline{\mathbf{s}}_3 \wedge \overline{\mathbf{s}}_2\right) = \dot{x}_1\overline{\mathbf{i}}_1 + \dot{y}_1\overline{\mathbf{i}}_2 + \dot{\phi}L_B\overline{\mathbf{s}}_1$$

$$\overline{{}^I \mathbf{V}^{B^*}} = \begin{matrix} \hat{\mathbf{e}} & \dot{x} \cos \phi - \dot{y} \sin \phi + \dot{\phi} L_B & \dot{u} \\ \hat{\mathbf{e}} & \dot{x} \sin \phi + \dot{y} \cos \phi & \dot{u} \\ \hat{\mathbf{e}} & 0 & \dot{u}_s \end{matrix} \quad (1)$$

- the acceleration of the center of mass B^* of Leonard with respect to the inertial frame $\{I\}$ and expressed in the local frame $\{S\}$ coordinates:

$$\overline{{}^I \mathbf{a}^{B^*}} = \begin{matrix} \hat{\mathbf{e}} & \ddot{x} \cos \phi - \ddot{y} \sin \phi + \ddot{\phi} L_B & \ddot{u} \\ \hat{\mathbf{e}} & \ddot{x} \sin \phi + \ddot{y} \cos \phi - \dot{\phi}^2 L_B & \ddot{u} \\ \hat{\mathbf{e}} & 0 & \ddot{u}_s \end{matrix} \quad (2)$$

- the acceleration of point A with respect to the inertial frame $\{I\}$ and expressed in the local frame $\{S\}$ coordinates:

$$\overline{{}^I \mathbf{a}^A} = \begin{matrix} \hat{\mathbf{e}} & \ddot{x} \cos \phi - \ddot{y} \sin \phi + \ddot{\phi} L_A & \ddot{u} \\ \hat{\mathbf{e}} & \ddot{x} \sin \phi + \ddot{y} \cos \phi - \dot{\phi}^2 L_A & \ddot{u} \\ \hat{\mathbf{e}} & 0 & \ddot{u}_s \end{matrix} \quad (3)$$

- the angular velocity and acceleration of the body B with respect to the frame $\{I\}$

$$\overline{{}^I \boldsymbol{\omega}^B} = -\dot{\phi} \overline{\mathbf{i}}_3 \quad (4)$$

$$\overline{{}^I \boldsymbol{\alpha}^B} = -\ddot{\phi} \overline{\mathbf{i}}_3 \quad (5)$$

3.1.1.2 Calculation of the forces exerted on Leonard. It is assumed that Leonard operates on a flat horizontal surface; therefore, there is no concern at present for the forces exerted in the z direction (due to gravity). Also, the front wheels are perfectly floating, that is why the ground does not exert any force on them in the (x,y) plane (Figure 3.3). Assume that:

- $\overline{\mathbf{F}}$ is the resultant of all external forces applied on Leonard

$$\overline{\mathbf{F}} = (\mathbf{F}_{NR} + \mathbf{F}_{NL}) \overline{\mathbf{s}}_1 + (\mathbf{F}_R + \mathbf{F}_L) \overline{\mathbf{s}}_2$$

- $\overline{\mathbf{M}}_{B^*}$ is the resultant of all external torques applied on the body B

$$\overline{\mathbf{M}}_{B^*} = \frac{W}{2} (\mathbf{F}_R - \mathbf{F}_L) \overline{\mathbf{s}}_3 - (\mathbf{L}_A - \mathbf{L}_B) (\mathbf{F}_{NR} + \mathbf{F}_{NL}) \overline{\mathbf{s}}_3$$

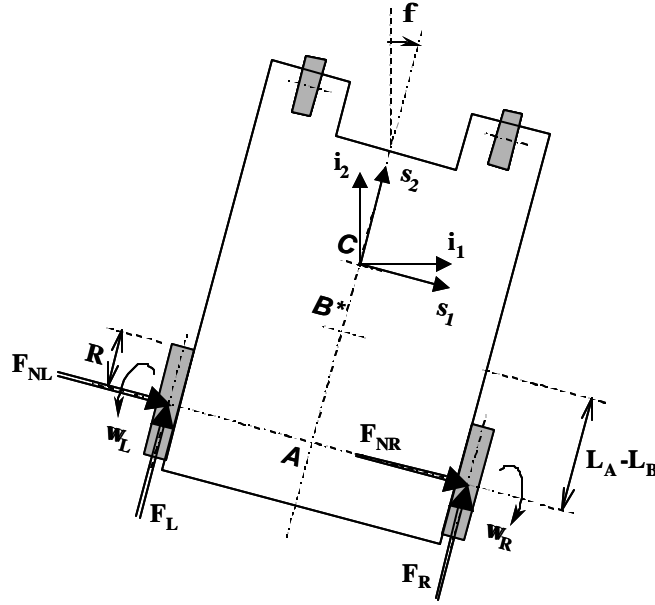


Figure 3.3. Free Body Diagram for the Vehicle

As F_{NR} and F_{NL} are always used as a sum, we note:

$$F_N \bar{s}_1 = (F_{NR} + F_{NL}) \bar{s}_1$$

F_N is called the constraint force since it is the one that imposes the constraint of no slip in the direction of the wheels' axis. (more about the constraint in Section 3.1.1.4.)

Therefore

$$\bar{F} = F_N \bar{s}_1 + (F_R + F_L) \bar{s}_2 \quad (6)$$

$$\bar{M}_{B^*} = \frac{\mathbf{x}^W}{\mathbf{c}} \frac{W}{2} (F_R - F_L) - (L_A - L_B) F_N \bar{s}_3 \quad (7)$$

3.1.1.3 Newton Euler's equations . Using (4), the angular momentum of the body B about point A in frame {I} is established (\bar{J}_A^B is the inertia dyadic of the body B at A in {I} and J_A is the moment of inertia of body B at A about \bar{i}_3):

$$\bar{H}_A^B = \bar{J}_A^B \times \bar{\omega}^B = -\dot{\phi} J_A \bar{i}_3$$

And its differentiated form with respect to time in frame {I} is:

$$\overline{^I \dot{H}_A^B} = \frac{^B d \overline{^I H_A^B}}{dt} + \overline{^I \omega^B} \wedge \left(\overline{^I H_A^B} \right) = -\ddot{\phi} J_A \vec{i}_3 \quad (8)$$

Using the parallel axis theorem, the relation between J_A and J_{zz} (the moment of inertia of body B at B^* about \vec{i}_3) is derived. The value of J_{zz} is extracted from tables [Moo98]

$$J_A = J_{zz} + m(L_A - L_B)^2 \quad (9)$$

$$J_{zz} = \frac{1}{12} m(L^2 + W^2) \quad (10)$$

so that, using (8):

$$\overline{^I \dot{H}_A^B} = -\ddot{\phi} (J_{zz} + m(L_A - L_B)^2) \vec{i}_3 \quad (11)$$

Now, using (2) and (6), Newton's second law is written for Leonard:

$$\vec{F} = m \overline{^I a^{B^*}}$$

$$\begin{array}{ccc} \hat{e} & F_N & \dot{u} \\ \hat{e} & (F_R + F_L) & \dot{u} \\ \hat{e} & 0 & \dot{u}_s \end{array} = m \begin{array}{ccc} \hat{e} & \ddot{x} \cos \phi - \ddot{y} \sin \phi + \ddot{\phi} L_B & \dot{u} \\ \hat{e} & \ddot{x} \sin \phi + \ddot{y} \cos \phi - \dot{\phi}^2 L_B & \dot{u} \\ \hat{e} & 0 & \dot{u}_s \end{array}$$

and using (3) and (11), the Newton-Euler equation projected on i_3 is:

$$\overline{M_A} = \overline{^I \dot{H}_A^B} - \overline{^I a^A} \wedge m \overline{AB^*}$$

$$\ddot{\phi} \times (J_{zz} + m(L_A - L_B)^2) = m(L_A - L_B) (\ddot{x} \cos \phi - \ddot{y} \sin \phi + \ddot{\phi} L_A) - \frac{W}{2} (F_R - F_L)$$

Thus, a set of three equations is obtained, where the first and the third are the two equations of motion, F_N in the second being the unknown constraint force.

$$m (\ddot{x} \sin \phi + \ddot{y} \cos \phi - \dot{\phi}^2 L_B) = (F_R + F_L) \quad (12)$$

$$m (\ddot{x} \cos \phi - \ddot{y} \sin \phi + \ddot{\phi} L_B) = F_N \quad (13)$$

$$\ddot{\phi} \times (J_{zz} - mL_B(L_A - L_B)) = m(L_A - L_B) (\ddot{x} \cos \phi - \ddot{y} \sin \phi) - \frac{W}{2} (F_R - F_L) \quad (14)$$

3.1.1.4 The Constraint Equation. In addition of the two equations of motion derived above, a constraint equation completes the dynamic model. This equation is a mathematical expression of the assumption that the vehicle does not cross slide along its driving axle.

At first, it is considered that the wheels roll without slip; therefore, $\overrightarrow{V^{P_L}} = \overrightarrow{V^{P_R}} = \vec{0}$, where P_L and P_R are the points of contact for respectively the left and right wheel.

$$\text{Besides, } \overrightarrow{V^{P_L}} = \overrightarrow{V^{A_L}} + \omega_L \overrightarrow{s_1} \wedge \overrightarrow{A_L P_L} \quad \text{therefore} \quad \overrightarrow{V^{A_L}} = \omega_L \overrightarrow{R s_2} \quad (15)$$

$$\text{Similarly, } \overrightarrow{V^{P_R}} = \overrightarrow{V^{A_R}} + \omega_R \overrightarrow{s_1} \wedge \overrightarrow{A_R P_R} \quad \text{therefore} \quad \overrightarrow{V^{A_R}} = \omega_R \overrightarrow{R s_2} \quad (16)$$

Now, $\overrightarrow{V^A}$ can be written in terms of $\overrightarrow{V^{A_L}}$ and $\overrightarrow{V^{A_R}}$:

$$\begin{aligned} \overrightarrow{V^A} &= \overrightarrow{V^S} + \overrightarrow{\omega^B} \wedge \overrightarrow{S A} \\ &= \dot{x} \vec{i}_1 + \dot{y} \vec{i}_2 + \dot{\phi} \overrightarrow{L_A s_1} \end{aligned} \quad (17)$$

$$\begin{aligned} \overrightarrow{V^{A_L}} &= \overrightarrow{V^S} + \overrightarrow{\omega^B} \wedge \overrightarrow{S A_L} \\ &= \dot{x} \vec{i}_1 + \dot{y} \vec{i}_2 + \dot{\phi} \overrightarrow{L_A s_1} + \frac{W}{2} \overrightarrow{x s_2} \end{aligned} \quad (18)$$

$$\begin{aligned} \overrightarrow{V^{A_R}} &= \overrightarrow{V^S} + \overrightarrow{\omega^B} \wedge \overrightarrow{S A_R} \\ &= \dot{x} \vec{i}_1 + \dot{y} \vec{i}_2 + \dot{\phi} \overrightarrow{L_A b_1} - \frac{W}{2} \overrightarrow{b_2} \end{aligned} \quad (19)$$

From (17) (18) and (19), it is deduced that:

$$\overrightarrow{V^A} = \frac{\overrightarrow{V^{A_L}} + \overrightarrow{V^{A_R}}}{2} \quad (20)$$

Then, substituting (15) and (16) into (20),

$$\overrightarrow{V^A} = R \frac{(\omega_L + \omega_R)}{2} \overrightarrow{b_2}$$

Now substituting this last result back into (17):

$$\dot{x}_1 \vec{i}_1 + \dot{y}_1 \vec{i}_2 + \dot{\phi} L_A \vec{s}_1 = R \frac{(\omega_L + \omega_R)}{2} \vec{s}_2$$

And a set of two equations is obtained, where the first is the relevant constraint equation:

$$\dot{x} \cos \phi - \dot{y} \sin \phi + L_A \dot{\phi} = 0 \quad (21)$$

$$\dot{x} \sin \phi + \dot{y} \cos \phi - R \frac{(\omega_L + \omega_R)}{2} = 0 \quad (22)$$

Thus, the three equations of motion for this model are (12), (14) and (21). Again, these results are confirmed independently with Lagrange's and Kane's methods in the Appendix C.

For the moment, equation (22) is not used; it will be employed later when information concerning the angular velocities of the wheels $(\omega_L + \omega_R)$ is needed, namely when dealing with the motors and the encoders. The constraint equation (21) describes the fact that the velocity in the direction of the driving wheels' axis is zero. Its differentiated form will later be useful:

$$\ddot{x} \cos \phi - \ddot{y} \sin \phi - \dot{x} \dot{\phi} \sin \phi - \dot{y} \dot{\phi} \cos \phi + L_A \ddot{\phi} = 0 \quad (23)$$

It is also convenient to consider the resisting torques on the wheels as inputs rather than the forces exerted by the ground. In this regard:

- C_R is the resisting torque due to the force F_R exerted on the right wheel.
- C_L is the resisting torque due to the force F_L exerted on the left wheel.

and assuming massless wheels:

$$F_R = \frac{C_R}{R} \quad \text{and} \quad F_L = \frac{C_L}{R}$$

Finally:

$$m(\ddot{x}\sin\phi + \ddot{y}\cos\phi - \dot{\phi}^2 L_B) = \frac{C_R + C_L}{R} \quad (24)$$

$$\ddot{\phi} \times (J_{zz} - mL_B(L_A - L_B)) = m(L_A - L_B)(\ddot{x}\cos\phi - \ddot{y}\sin\phi) - \frac{W}{2} \frac{\mathbf{a}^{C_R} - C_L}{\xi} \frac{\bar{\mathbf{0}}}{R} \frac{\dot{\phi}}{\theta} \quad (25)$$

$$\dot{x}\cos\phi - \dot{y}\sin\phi + L_A \dot{\phi} = 0 \quad (21)$$

3.1.2 Kinematics. Besides the equations of motion, the control algorithm requires the derivation of equations to link the sensor outputs to the state variables.

At first, the data for the encoders are considered:

$$\text{From (15) and (16):} \quad \overline{{}^I\mathbf{V}^{A_L}} - \overline{{}^I\mathbf{V}^{A_R}} = \mathbf{R}(\omega_L - \omega_R) \overline{\mathbf{b}_2} \quad (26)$$

$$\text{From (18) and (19):} \quad \overline{{}^I\mathbf{V}^{A_L}} - \overline{{}^I\mathbf{V}^{A_R}} = \dot{\phi} \mathbf{W} \overline{\mathbf{b}_2} \quad (27)$$

$$\text{Substituting (26) into (27):} \quad (\omega_L - \omega_R) \mathbf{R} = \dot{\phi} \mathbf{W} \quad (28)$$

Equation (22) is an expression of the sum of the angular velocities $(\omega_L + \omega_R)$. Since the expression for the difference is now also available (28), each encoder angular velocity can be expressed independently in terms of the vehicle state variables:

$$\omega_L = \frac{1}{R} \frac{\mathbf{a}}{\xi} \ddot{x}\sin\phi + \ddot{y}\cos\phi + \dot{\phi} \frac{W}{2} \frac{\bar{\mathbf{0}}}{\theta} \quad (29)$$

$$\omega_R = \frac{1}{R} \frac{\mathbf{a}}{\xi} \ddot{x}\sin\phi + \ddot{y}\cos\phi - \dot{\phi} \frac{W}{2} \frac{\bar{\mathbf{0}}}{\theta} \quad (30)$$

Recall that the point S $(x_S, y_S$ in $\{I\})$ refers to the location of the GPS antenna whereas the point C $(x, y$ in $\{I\})$ indicates the point which should follow the desired trajectory. Therefore, the position of the sensor point (x_S, y_S) is actually the information

given by the DGPS measurements. These coordinates are linked to the state variables with geometric relations:

$$x_s = x + L_s \sin \phi \quad (31)$$

$$y_s = y + L_s \cos \phi \quad (32)$$

3.1.3 State Space Model. In this section, the equations above are linearized about a nominal straight line trajectory to establish the final state space representation. (Future work may require linearizations about more complex trajectories.)

3.1.3.1 The Input Equation. Assume that it is desired to have point C follow a straight line, for example along the y axis, with a constant nominal velocity, called V_{y0} .

$$\dot{y} = V_{y0} + \delta \dot{y} \quad \dot{x} = \delta \dot{x}$$

$$\ddot{y} = \delta \ddot{y} \quad \ddot{x} = \delta \ddot{x}$$

where all the δ 's stand for small quantities and the angle ϕ remains very small, so that:

$$\sin \phi \approx \phi \quad \text{and} \quad \cos \phi \approx 1$$

these equations are substituted into the equations of motion (21), (22) and (23) and the second and higher order δ 's are neglected. This results in (referring to notations without δ 's):

$$\ddot{y} = \frac{1}{m} \mathbf{a}^C_R + \frac{C_L}{R} \ddot{\theta} \quad (33)$$

$$\ddot{\phi} \mathbf{x} (J_{zz} - mL_B (L_A - L_B)) = m (L_A - L_B) \ddot{x} - \frac{W}{2} \mathbf{a}^C_R - \frac{C_L}{R} \ddot{\theta} \quad (34)$$

$$\dot{x} = V_{y0} \phi - L_A \dot{\phi} \quad (35)$$

These are the linearized equations of motion. To compose a state space model, the highest order differentiate of the state variable (\ddot{x} and $\ddot{\phi}$) must be decoupled. Substituting the linearized form of (23) into (30) results in (with (9)):

$$\ddot{\phi} = \frac{1}{J_A} \hat{e} m (L_A - L_B) V_{y0} \dot{\phi} - \frac{W}{2} \frac{\mathbf{x} C_R}{\hat{e} R} - \frac{C_L}{R} \frac{\mathbf{o} \dot{u}}{\hat{e} \dot{u}} \quad (36)$$

now assume:

$$\alpha = \frac{m(L_A - L_B) V_{y0}}{J_A} \quad (37)$$

$$\beta = \frac{W}{2 \mathbf{x} J_A} \quad (38)$$

finally, adding the linearized constraint equation:

$$\ddot{y} = \frac{1}{m} \frac{\mathbf{x} C_R}{\hat{e} R} + \frac{C_L}{R} \frac{\mathbf{o}}{\hat{e}} \quad (39)$$

$$\ddot{\phi} = \alpha \mathbf{x} \dot{\phi} - \beta \mathbf{x} \frac{C_R}{R} + \beta \mathbf{x} \frac{C_L}{R} \quad (40)$$

$$\dot{x} = V_{y0} \phi - L_A \dot{\phi} \quad (41)$$

in matrix form:

$$\begin{array}{l} \hat{e} \dot{y} \dot{u} \\ \hat{e} \dot{\phi} \dot{u} \\ \hat{e} \dot{x} \dot{u} \\ \hat{e} \dot{y} \dot{u} \\ \hat{e} \dot{\phi} \dot{u} \end{array} = \begin{array}{l} \hat{e} 0 \\ \hat{e} 0 \\ \hat{e} 0 \\ \hat{e} 1 \\ \hat{e} 0 \end{array} \begin{array}{l} 0 \\ \alpha \\ -L_A \\ 0 \\ 1 \end{array} \begin{array}{l} 0 \\ 0 \\ 0 \\ 0 \\ 0 \end{array} \begin{array}{l} 0 \\ 0 \\ V_{y0} \\ 0 \\ 0 \end{array} \begin{array}{l} \dot{u} \hat{e} \dot{y} \dot{u} \\ \dot{u} \hat{e} \dot{\phi} \dot{u} \\ \dot{u} \hat{e} \dot{x} \dot{u} + \hat{e} \\ \dot{u} \hat{e} \dot{y} \dot{u} \\ \dot{u} \hat{e} \dot{\phi} \dot{u} \end{array} + \begin{array}{l} \hat{e} \frac{R}{m} \\ \hat{e} -R\beta \\ \hat{e} 0 \\ \hat{e} 0 \\ \hat{e} 0 \end{array} \begin{array}{l} \frac{R}{m} \dot{u} \\ R\beta \dot{u} \\ \hat{e} C_R \dot{u} \\ \hat{e} C_L \dot{u} \\ \hat{e} \dot{u} \end{array} \quad (42)$$

(42) is the state space input equation, written in the form:

$$\dot{\vec{x}} = F\vec{x} + G\vec{u}$$

where: \vec{x} is the state vector
 F is the system matrix
 G is the input matrix
 \vec{u} is the input vector.

3.1.3.2 The Output Equation. In the same way, equations (29) to (32) are

linearized and written in matrix form in order to get the output equation:

The linearized equations are:

$$\omega_L R = \dot{\phi} \frac{W}{2} + V_{y0} + \dot{y} \tag{43}$$

$$\omega_R R = V_{y0} + \dot{y} - \dot{\phi} \frac{W}{2} \tag{44}$$

$$x_s = x + \phi L_s \tag{45}$$

$$y_s = y + L_s \tag{46}$$

and in matrix form:

$$\begin{bmatrix} \hat{e} \\ \hat{e} \\ \hat{e} \\ \hat{e} \\ \hat{e} \\ \hat{e} \end{bmatrix} \begin{bmatrix} \omega_L \\ \omega_L \\ \omega_R \\ \omega_R \\ x_s \\ y_s \end{bmatrix} - \begin{bmatrix} V_{y0} \\ V_{y0} \\ V_{y0} \\ V_{y0} \\ x_s \\ y_s \end{bmatrix} \frac{\hat{u}}{R} = \begin{bmatrix} \hat{e} \\ \hat{e} \\ \hat{e} \\ \hat{e} \\ \hat{e} \\ \hat{e} \end{bmatrix} \begin{bmatrix} 1 \\ 1 \\ 1 \\ 1 \\ 0 \\ 0 \end{bmatrix} \frac{1}{R} + \begin{bmatrix} W \\ -W \\ 0 \\ 0 \\ 0 \\ 0 \end{bmatrix} \frac{\hat{u}}{2R} + \begin{bmatrix} 0 \\ 0 \\ 0 \\ 0 \\ L_s \\ 0 \end{bmatrix} \hat{u} + \begin{bmatrix} 0 \\ 0 \\ 0 \\ 0 \\ 0 \\ 0 \end{bmatrix} \dot{\hat{u}} + \begin{bmatrix} 0 \\ 0 \\ 0 \\ 0 \\ 0 \\ 0 \end{bmatrix} \dot{\hat{y}} + \begin{bmatrix} 0 \\ 0 \\ 0 \\ 0 \\ 0 \\ 0 \end{bmatrix} \dot{\hat{\phi}} \tag{47}$$

(47) is an equation equation of the form:

$$\vec{y} = H\vec{x}$$

where: \vec{y} is the output vector

H is the output matrix

The components of \vec{y} are known in real time: the first two elements from the top are given by the right and left encoders whereas the two others are given by the GPS measurements (remember that L_s , V_{y0} and R are all fixed and known).

If only the GPS system is used, the output equation is:

$$\begin{bmatrix} \hat{e}_x \\ \hat{e}_y - L_s \hat{u} \\ \hat{e}_\phi \\ \hat{e}_H \end{bmatrix} = \begin{bmatrix} 0 & 0 & 1 & 0 \\ 0 & 0 & 0 & 1 \\ L_s \hat{u} & \hat{e}_x & \hat{e}_y & \hat{e}_\phi \\ 0 & \hat{e}_x & \hat{e}_y & \hat{e}_H \end{bmatrix} \begin{bmatrix} x_s \\ y_s \\ \phi \\ H \end{bmatrix} \quad (48)$$

3.2 Dynamic Model for the Motors

The previous model of Leonard assumed that the inputs of the system were the resistant torques resulting from the actions of the ground on the vehicle. Actually, two DC motors are used to drive the wheels, and the information given to them is a voltage. The goal of this section is to establish a model for the motors linking the input voltage to the torques due to the load.

The mathematical modeling of a DC motor is a common case study of system dynamics [Lon00], [Whi 97]; the model derived here takes the reducer into account. This model will be incorporated into the vehicle dynamic model in the next section.

3.2.1 Functioning of a DC Motor. This first subsection introduces the main features of a DC motor.

The use of electromechanical actuators is particularly appropriate for Leonard because of their accuracy for the control of speed, their compactness and their adapted power level. Those characteristics are especially true for the permanent magnet DC motor.

A permanent magnet DC motor is a mechanism which converts electrical power to mechanical power via magnetic coupling. The electrical power is provided by a voltage source (batteries), while the mechanical power is provided by a spinning rotor.

A very basic DC motor is constructed of two main components: the rotor and the stator. The rotor (or armature) rotates within the framework of the stationary stator (Figure 3.4). The stator consists of permanent magnets which create a magnetic field. The rotor consists of an electromagnet created by a coil wound around an iron core. It rotates due to the phenomenon of attracting and opposing forces. A magnetic field is generated by this rotor thanks to the current circulating in the coil and the polarity is constantly changed by alternating this current (also known as commutation) causing the rotor to rotate.

The commutator is made up of two semi circular copper segments mounted on the shaft at the end of the rotor. Each extremity of the rotor coil is connected to a copper segment. Stationary brushes ride on the copper segments whereby the rotor coil is connected to a stationary DC voltage supply by a near frictionless contact.

The motion of the rotor makes the current in the coil change its direction at each rotation and thus change the polarity of the magnetic field.

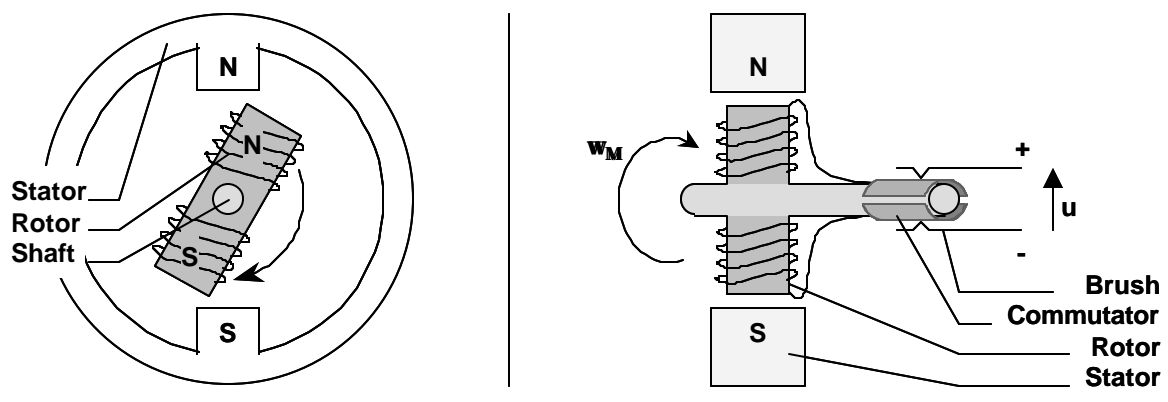


Figure 3.4. The Different Components of a DC Motor

3.2.2 Dynamic Model. At first, the mechanical equations for the motor and reducer are derived, then the ones related to the electrical characteristics. Also, it is usual to do the following assumptions: (1) no induced magnetic reaction and conservation of energy (2) no centrifugal coupling or Coriolis terms (3) constant masses (4) constant geometry versus time and temperature variations. The relevant notation is defined in Table 3.2.

The mechanical equations are established according to the model presented Figure 3.5.

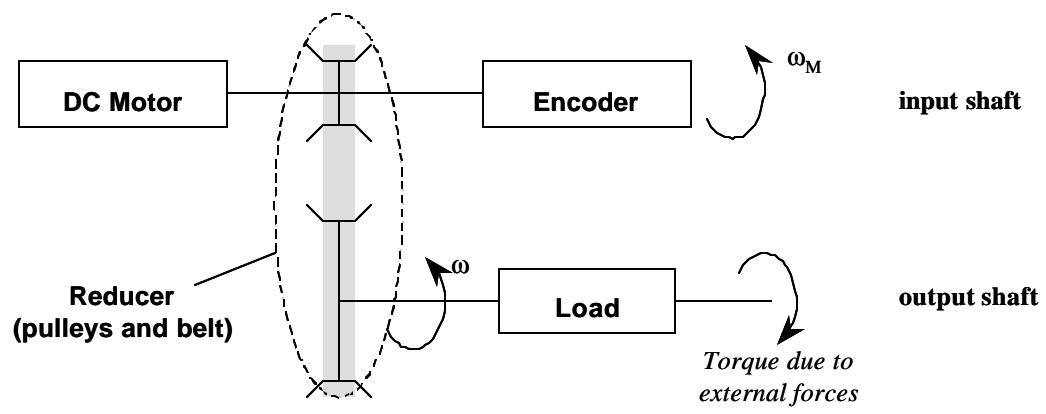


Figure 3.5. Illustration of the System "Motor + Reducer + Load"

Table 3.2. Notations for the Motors

Notations	Definition
<i>DC Motor:</i>	
u	: tension supplied by the voltage source
i	: (induced) current in the rotor
L_a, R_a	: inductance and resistance in the rotor (armature)
J_M	: motor inertia
k_T, k_E	: respectively: electromechanical torque and voltage constants
ϕ_M	: position of the motor shaft
ω_M	$= \dot{\phi}_M$: angular velocity of the motor's shaft
T_M	: electromagnetic torque (torque supplied by the motor)
<i>DC Motor + Reducer:</i>	
T_{SM}	: torque due to static friction on the motor's shaft
f_{VM}	: (viscous friction) damping coefficient on the motor's shaft
<i>Load:</i>	
$\phi, \dot{\phi}$: angular position and velocity of the load; we note: $\dot{\phi} = \omega$
J_L	: moment of inertia for the load
T_E	: torque due to external forces
T_{SL}	: torque due to static friction on the output's shaft
f_{VL}	: damping coefficient on the output's shaft
T_R	: resisting torque on the output's shaft
<i>Reducer:</i>	
N	$= \frac{\phi_M}{\phi}$: reduction ratio
J_R	: moment of inertia of the reducer's parts on the motor's shaft
T_{RM}	: resisting torque on the motor's shaft
<i>DC Motor + Reducer + Load:</i>	
J	: moment of inertia for the rotor, the reducer and the mechanical load referenced to the motor's shaft
f_v	: damping coefficient associated with the mechanical rotational system of the machine referenced to the motor's shaft
T_S	: global static friction torque referenced to the motor's shaft
T_L	: global torque due to static friction and external forces referenced to the motor's shaft

The Newton Euler equations are applied to each element.

For the load:
$$\mathbf{T}_R = \mathbf{J}_L \cdot \dot{\boldsymbol{\omega}} + \mathbf{f}_{VL} \cdot \boldsymbol{\omega} + \mathbf{C}_{SC} + \mathbf{T}_E \quad (49)$$

For the reducer:
$$\mathbf{T}_{RM} = \mathbf{T}_R / N \quad (50)$$

For the motor:
$$\mathbf{T}_M = (\mathbf{J}_M + \mathbf{J}_R) \cdot \dot{\boldsymbol{\omega}}_M + \mathbf{f}_{VM} \cdot \boldsymbol{\omega}_M + \mathbf{T}_{SM} + \mathbf{T}_{RM} \quad (51)$$

And consider
$$\boldsymbol{\omega}_M = N \cdot \boldsymbol{\omega} \quad \dot{\boldsymbol{\omega}}_M = N \cdot \dot{\boldsymbol{\omega}} \quad (52)$$

Using (52) and substituting (49) into (50), and the result into (51):

$$\mathbf{T}_M = \left(\mathbf{J}_M + \mathbf{J}_R + \frac{\mathbf{J}_L}{N^2} \right) \cdot \dot{\boldsymbol{\omega}}_M + \left(\frac{\mathbf{f}_{VL}}{N^2} + \mathbf{f}_{VM} \right) \cdot \boldsymbol{\omega}_M + \frac{\mathbf{T}_E}{N} + \frac{\mathbf{T}_{SL}}{N} + \mathbf{T}_{SM} \quad (53)$$

According to the definitions (Table 3.2):

$$\mathbf{J} = \mathbf{J}_M + \mathbf{J}_R + \frac{\mathbf{J}_L}{N^2}$$

$$\mathbf{f}_V = \frac{\mathbf{f}_{VL}}{N^2} + \mathbf{f}_{VM}$$

$$\mathbf{T}_S = \frac{\mathbf{T}_{SL}}{N} + \mathbf{T}_{SM} \quad \text{hence} \quad \mathbf{T}_L = \frac{\mathbf{T}_E}{N} + \mathbf{T}_S \approx \frac{\mathbf{T}_E}{N}$$

And (52) becomes:
$$\mathbf{T}_M = \mathbf{J} \cdot \dot{\boldsymbol{\omega}}_M + \mathbf{f}_V \cdot \boldsymbol{\omega}_M + \mathbf{T}_L \quad (54)$$

The electrical equations establish the relationship between torque and voltage with the intermediary of the current. First of all, the torque constant is defined by:

$$\mathbf{T}_M = k_T \cdot \mathbf{i}$$

and substituting this equation into (54) leads to the “mechanical equations”:

$$k_T \cdot \mathbf{i} = \mathbf{J} \cdot \dot{\boldsymbol{\omega}}_M + \mathbf{f}_V \cdot \boldsymbol{\omega}_M + \mathbf{T}_L \quad (55)$$

The derivation of the electrical equations is based on Figure 3.6: a DC motor can be represented by a voltage source (U) across the coil of the rotor. The electrical equivalent

of the rotor's coil can be described as a resistance (R_a) in series with an inductance (L_a) in series with an induced voltage (U_C) opposed to the voltage source and often called the back electromotive force (back emf).

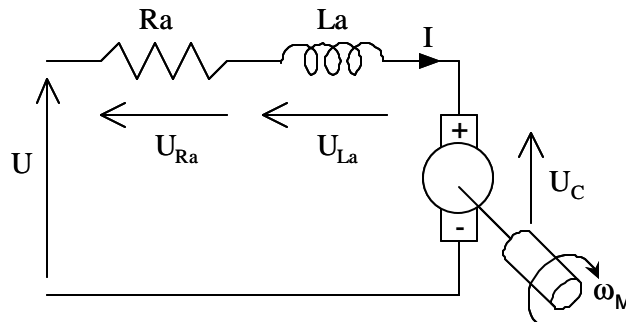


Figure 3.6. Electrical Representation of a DC Motor

Kirchoff's voltage law states that the sum of all voltages around a loop must equal zero:

$$u - u_{L_a} - u_{R_a} - u_C = 0 \quad (56)$$

where

$$u_{R_a} = R_a \cdot i \quad u_{L_a} = L_a \cdot \frac{d}{dt}i \quad u_C = k_E \cdot \omega_M$$

back to (56):

$$u = L_a \cdot \frac{d}{dt}i + R_a \cdot i + k_E \cdot \omega_M \quad (57)$$

As a conclusion, the goal of expressing the resisting torque exerted by the ground on the wheels (T_L) in terms of the input voltage (u) is reached with the introduction of the current (i), thanks to the mechanical equation (55) and to the electrical equations (57)

$$(55) \rightarrow k_T \cdot i = J \cdot \dot{\omega}_M + f_v \cdot \omega_M + T_L$$

$$(57) \rightarrow u = L_a \cdot \frac{d}{dt}i + R_a \cdot i + k_E \cdot \omega_M$$

These equations will be used to model the two motors on each driving wheel.

Several notations and dimensions are used by the suppliers of DC motors (Appendix

A). Among those dimensions, three characteristic time constants can be underlined:

$$\tau_e = \frac{L_a}{R_a} \quad : \text{electrical time constant}$$

$$\tau_m = \frac{J}{f_V} \quad : \text{mechanical time constant}$$

$$\tau_{em} = \frac{(J \cdot R_a)}{(k_E \cdot k_T)} \quad : \text{electromechanical time constant}$$

3.3 State Space Model for the Whole System Including Motors

The results of the two preceding sections are now combined to obtain a model for the whole system, with voltages as inputs for the right and left motors. The sensors' outputs are still the position of the sensor point (S), and the angular velocities of both motors.

Again, equations (39), (40) and (41) (Section 3.1) describe the dynamic model with the state variables, and with torques as inputs (C_R and C_L). Equations (55) and (57) above give expressions of the motor's input voltage in terms of its torque. Several manipulations are necessary because the motor's equations are referenced to the motor shaft, while the input torques in the first section are referenced to the wheels axis. The reducer connects them together. Assuming that the motors on the two wheels are identical, consider the notations of the Table 3.3. With these notations,

$$C_R = N \cdot T_{LR} \quad \text{and} \quad C_L = N \cdot T_{LL} \quad (58)$$

$$\omega_{MR} = N \cdot \omega_R \quad \text{and} \quad \omega_{ML} = N \cdot \omega_L \quad (59)$$

Note that a reducer is a speed reducer but a torque amplifier.

Table 3.3. Notations for the Right and Left Motors

Notations	Definition
u_R, u_L	: tension supplied by the voltage source respectively to the right and left hand side motors
i_R, i_L	: (induced) current in the rotor from respectively the right and left hand side motors
T_{LR}, T_{LL}	: torque of the mechanical load supplied by respectively on the right and left hand side motors
ω_{MR}, ω_{ML}	: angular velocities respectively of the right and left hand side motor
$\dot{\omega}_{MR}, \dot{\omega}_{ML}$: angular accelerations respectively of the right and left hand side motors

If the equation (57) is kept in this form, the current (i) has to be considered as a state because it is present in more than one degree of differentiation with respect to time. In order to avoid the addition of this supplementary state variable, the following assumption is made. Recall the equation:

$$(57) \rightarrow L_a \cdot \frac{di}{dt} + R_a \cdot i = u - k_E \cdot \omega_M$$

Consider the right hand side terms as an input. It is assumed that the kinematics of the motors is such that a change in this input would instantaneously be translated into a change in the current (i). This means that the role of $\frac{di}{dt}$ is negligible. Indeed, this is acceptable because, for all motors proposed by different suppliers, $L_a \ll R_a$. In other words, the electrical time constant (previously noted $\tau_e = \frac{L_a}{R_a}$) is more than 100 times lower than the lowest sample time which could be selected, so that eventually the system

will not be sensitive at all to the small kinematic effect induced by term $L_a \cdot \frac{di}{dt}$. And

$$(57) \text{ becomes: } \quad i = \frac{1}{R_a} u - \frac{k_E}{R_a} \omega_M \quad (58)$$

Now the current is, as desired, written in terms of input (u) and output (ω_M).

Applying the notations from Table 3.3 to (58)

$$\begin{array}{cc} \text{LEFT hand side} & \text{RIGHT hand side} \\ i_L = \frac{1}{R_a} u_L - \frac{k_E}{R_a} \omega_{ML} & i_R = \frac{1}{R_a} u_R - \frac{k_E}{R_a} \omega_{MR} \end{array} \quad (59)$$

Then again, for the right and left hand side, substituting these results into (55) gives (60):

$$T_{LL} = \frac{k_T}{R_a} u_L - J \cdot \dot{\omega}_{ML} + \left(\frac{k_T \cdot k_E}{R_a} - f_v \right) \omega_{ML} \quad T_{LR} = \frac{k_T}{R_a} u_R - J \cdot \dot{\omega}_{MR} + \left(\frac{k_T \cdot k_E}{R_a} - f_v \right) \omega_{MR}$$

Also, the encoders actually read the angular velocities on the motors' shafts, ω_{MR} and ω_{ML} . Therefore, these quantities have to be expressed in terms of state variables; substituting (52) into (43) and (44):

$$\omega_{ML} = \frac{NV_{y0}}{R} + \frac{N}{R} \dot{y} + \frac{NW}{2R} \dot{\phi} \quad \omega_{MR} = \frac{NV_{y0}}{R} + \frac{N}{R} \dot{y} - \frac{NW}{2R} \dot{\phi} \quad (61)$$

Differentiating these results:

$$\dot{\omega}_{ML} = \frac{N}{R} \ddot{y} + \frac{NW}{2R} \ddot{\phi} \quad \dot{\omega}_{MR} = \frac{N}{R} \ddot{y} - \frac{NW}{2R} \ddot{\phi} \quad (62)$$

Substituting these equations into (60) and the result into (58):

$$\text{RIGHT} \quad C_R = Nk_T \cdot i_R - \frac{N^2 J}{R} \left(\ddot{y} - \frac{W}{2} \ddot{\phi} \right) - \frac{N^2 f_v}{R} \cdot \left(V_{y0} + \dot{y} - \frac{W}{2} \dot{\phi} \right) \quad (63)$$

$$\text{LEFT} \quad C_L = Nk_T \cdot i_L - \frac{N^2 J}{R} \left(\ddot{y} + \frac{W}{2} \ddot{\phi} \right) - \frac{N^2 f_v}{R} \cdot \left(V_{y0} + \dot{y} + \frac{W}{2} \dot{\phi} \right) \quad (64)$$

Then (61) is substituted into (58), and with

$$\chi = \frac{Nk_E}{R_a R} :$$

$$\text{RIGHT} \quad i_R = \frac{1}{R_a} u_R - \chi \left(V_{y0} + \dot{y} - \frac{W}{2} \dot{\phi} \right) \quad (65)$$

$$\text{LEFT} \quad i_L = \frac{1}{R_a} u_L - \chi \left(V_{y0} + \dot{y} + \frac{W}{2} \dot{\phi} \right) \quad (66)$$

Finally, substituting (65) into (63) and (66) into (64):

$$\text{RIGHT} \quad C_R = \frac{Nk_T}{R_a} \cdot u_R - \frac{N^2 J}{R} \left(\ddot{y} - \frac{W}{2} \ddot{\phi} \right) - \left(Nk_T \chi + \frac{N^2 f_V}{R} \right) \cdot \left(V_{y0} + \dot{y} - \frac{W}{2} \dot{\phi} \right) \quad (67)$$

$$\text{LEFT} \quad C_L = \frac{Nk_T}{R_a} \cdot u_L - \frac{N^2 J}{R} \left(\ddot{y} + \frac{W}{2} \ddot{\phi} \right) - \left(Nk_T \chi + \frac{N^2 f_V}{R} \right) \cdot \left(V_{y0} + \dot{y} + \frac{W}{2} \dot{\phi} \right) \quad (f68)$$

Now that C_R and C_L are at last written in terms of state and input variables, it is possible to come back to the linearized equations of motion, (39), (40) and (41) from Section 3.1. A few manipulations lead to the following results:

(39) becomes:

$$\ddot{y} = \frac{RNk_T}{(mR^2 + 2N^2 J) R_a} (u_R + u_L) - 2 \times \frac{N^2 f_V + NRk_T \chi}{mR^2 + 2N^2 J} (V_{y0} + \dot{y})$$

$$\text{or} \quad \ddot{y} = \zeta \times (u_R + u_L) + \gamma \times (V_{y0} + \dot{y}) \quad (69)$$

$$\text{with} \quad \gamma = -2 \times \frac{N^2 f_V + NRk_T \chi}{mR^2 + 2N^2 J}$$

$$\text{and} \quad \zeta = \frac{RNk_T}{(mR^2 + 2N^2 J) R_a}$$

and (40) becomes:

$$\ddot{\phi} = \frac{R\beta N k_T}{(R^2 + \beta N^2 J W) R_a} \times (u_L - u_R) + \frac{\alpha R^2 - \beta W N (N f_V + R k T \chi)}{R^2 + \beta N^2 J W} \times \dot{\phi}$$

or
$$\ddot{\phi} = \beta' \times (u_L - u_R) + \alpha' \times \dot{\phi} \quad (70)$$

with
$$\beta' = \frac{R\beta N k_T}{(R^2 + \beta N^2 J W) R_a}$$

$$\alpha' = \frac{\alpha R^2 - \beta W N (N f_V + R k T \chi)}{R^2 + \beta N^2 J W} \quad (71)$$

and
$$\alpha = \frac{m(L_A - L_B) V_{y0}}{J_A}$$

$$\beta = \frac{W}{2 \times J_A}$$

with
$$J_A = \frac{1}{12} m (L^2 + W^2) + m (L_A - L_B)^2$$

Also note that (41) remains unmodified:

$$(41) \rightarrow \dot{x} = V_{y0} \phi - L_A \dot{\phi}$$

Writing the equations (69), (70) and (41) in matrix form results in the input state space equation for the whole system including motors:

$$\begin{array}{cccccccccccc} \hat{e} & \ddot{y} & \dot{u} & \hat{e} \gamma & 0 & 0 & 0 & 0 & \dot{u} \hat{e} \dot{y} + V_{y0} \dot{u} & \hat{e} & \zeta & \zeta \dot{u} \\ \hat{e} & \ddot{\phi} & \dot{u} & \hat{e} 0 & \alpha' & 0 & 0 & 0 & \dot{u} \hat{e} \dot{\phi} & \dot{u} & \hat{e} -\beta' & \beta' \dot{u} \\ \hat{e} & \dot{x} & \dot{u} & \hat{e} 0 & -L_A & 0 & 0 & V_{y0} & \dot{u} \hat{e} x & \dot{u} + \hat{e} & 0 & 0 \dot{u} \hat{e} u_R \dot{u} \\ \hat{e} & \dot{y} + V_{y0} \dot{u} & \dot{u} & \hat{e} 1 & 0 & 0 & 0 & 0 & \dot{u} \hat{e} y & \dot{u} & \hat{e} & 0 \dot{u} \hat{e} u_L \dot{u} \\ \hat{e} & \dot{\phi} & \dot{u} & \hat{e} 0 & 1 & 0 & 0 & 0 & \dot{u} \hat{e} \phi & \dot{u} & \hat{e} & 0 \dot{u} \hat{e} \end{array} \quad (72)$$

The output equation, with the encoders reading the motors' angular velocities:

$$\begin{aligned}
 \begin{bmatrix} \dot{e}_x \\ \dot{e}_y \\ \dot{e}_\phi \end{bmatrix} &= \begin{bmatrix} \omega_{ML} & \dot{u} \\ \omega_{MR} & \dot{u} \\ x_s & \dot{u} \\ y_s - L_s & \dot{u} \end{bmatrix} = \begin{bmatrix} \frac{N}{2R} & \frac{NW}{2R} \\ -\frac{N}{2R} & -\frac{NW}{2R} \\ 0 & 0 \\ 0 & 0 \end{bmatrix} \begin{bmatrix} \dot{\theta}_R \\ \dot{\theta}_L \end{bmatrix} + \begin{bmatrix} \dot{y}_0 + V_{y0} \\ \dot{\phi} \\ x \\ y \\ \phi \end{bmatrix} \begin{bmatrix} \dot{u} \\ \dot{u} \\ \dot{u} \\ \dot{u} \\ \dot{u} \end{bmatrix}
 \end{aligned} \tag{73}$$

and without encoders:

$$\begin{aligned}
 \begin{bmatrix} \dot{e}_x \\ \dot{e}_y \\ \dot{e}_\phi \end{bmatrix} &= \begin{bmatrix} x_s & \dot{u} \\ y_s - L_s & \dot{u} \\ \dot{u} \end{bmatrix} = \begin{bmatrix} 0 & 0 & 1 & 0 \\ 0 & 0 & 0 & 1 \\ L_s & 0 & 0 & 0 \end{bmatrix} \begin{bmatrix} \dot{u} \\ \dot{u} \\ \dot{u} \\ \dot{u} \end{bmatrix} + \begin{bmatrix} \dot{y}_0 + V_{y0} \\ \dot{\phi} \\ x \\ y \\ \phi \end{bmatrix} \begin{bmatrix} \dot{u} \\ \dot{u} \\ \dot{u} \\ \dot{u} \\ \dot{u} \end{bmatrix}
 \end{aligned} \tag{74}$$

Note that system dynamics can be decoupled into “in track” and “cross track” components:

- “Cross track”: regrouping x , ϕ and $\dot{\phi}$
- “In track”: for y and \dot{y}

For now, we may consider such decoupling as merely a convenience, but in further work, the distinction will become important.

The model composed of equations (72) and (73) (or (74)) is what is called “the Plant” in controls theory. The more accurate the plant model is, the more robust the navigation system will ultimately be.

3.4 Controllability, Observability and Stability

This section aims to validate the previous state space representation. Numerical values (Table 3.4) can be applied and it is possible to carry out the first analyses. Note that the Table 3.4 is established for a certain position of the control point (point C) and of the GPS antenna (point S), but the tests are performed for all possible values.

Table 3.4. Values of the Quantities Describing the Model

Dimension		Value	Unit
L_A	=	0.2032	m
L_B	=	0.4064	m
L_S	=	0.4064	m
L	=	0.8128	m
W	=	0.6096	m
R	=	0.127	m
m	=	82.74	kg
V_{yo}	=	9.7401	miles per hour
	=	1.3542	$m.s^{-1}$
R_a	=	0.28	Ohms
k_T	=	0.215	N.m/A
k_E	=	1.344	V.s
J	=	$2.33 \cdot 10^{-4}$	N.m.sec ²
f_V	=	0.003	N.m.sec
N	=	3.2727	

3.4.1 Observability and Controllability. Observability and controllability are necessary conditions for control system design. This verification does not give any quantitative results, but avoids pursuit of a model which cannot be implemented.

Basically, the observability check ensures that each state can be estimated by use of the sensors' measurements. The controllability is a way to express that the inputs are sufficient to reach any desired state in a finite time [Fra98]. Using the Matlab functions ("ctrb" and "obsv"), it is easy to confirm that the state space representation is fully controllable and observable, both with and without encoders, for any positions of C and S on Leonard.

3.4.2 Stability. The Figure 3.8 summarizes the study of stability. The stability for the model including motors is studied Section 4.3.1, once the analysis of model without motors has brought the first useful conclusions.

	<i>Model Without Motors</i>	<i>Model With Motors</i>
<i>System Matrix</i>	$\begin{matrix} \dot{e}_0 & 0 & 0 & 0 & 0 \\ \dot{e}_1 & \alpha & 0 & 0 & 0 \\ \dot{e}_2 & -L_A & 0 & 0 & V_{y0} \\ \dot{e}_3 & 0 & 0 & 0 & 0 \\ \dot{e}_4 & 1 & 0 & 0 & 0 \end{matrix} \begin{matrix} \dot{u} \\ \dot{u} \\ \dot{u} \\ \dot{u} \\ \dot{u} \end{matrix}$	$\begin{matrix} \dot{e}_\gamma & 0 & 0 & 0 & 0 \\ \dot{e}_0 & \alpha' & 0 & 0 & 0 \\ \dot{e}_1 & -L_A & 0 & 0 & V_{y0} \\ \dot{e}_2 & 0 & 0 & 0 & 0 \\ \dot{e}_3 & 1 & 0 & 0 & 0 \end{matrix} \begin{matrix} \dot{u} \\ \dot{u} \\ \dot{u} \\ \dot{u} \\ \dot{u} \end{matrix}$
<i>Poles</i>	$\{\alpha \ 0 \ 0 \ 0 \ 0\}$	$\{\alpha' \ \gamma \ 0 \ 0 \ 0\}$
<i>Stability</i>	<p style="text-align: center;"><u>Forward</u> motion ($\alpha < 0$) → The system is marginally stable</p> <p style="text-align: center;"><u>Backward</u> motion ($\alpha > 0$) → The system is unstable</p>	<p style="text-align: center;">$\gamma < 0$ is always true</p> <p style="text-align: center;">α' is studied in detail Section 4.3.1</p>

Figure 3.7. Comparison and Stability Study for the Models With and Without Motors

For the model without motors, the stability depends on the sign of α . Recall that:

$$(37) \rightarrow \alpha = \frac{m(L_A - L_B)V_{y0}}{J_A}$$

First, assume that the statement: $L_A - L_B < 0$ is always true. The reverse statement would signify that most of the mass is placed on the other side of the driving axle, which would unbalance the vehicle. Then, the sign of α is determined by the sign of V_{y0} , in other words by the sense of motion:

- $V_{y0} > 0$, the system is stable, we call that the “forward” motion.
- $V_{y0} < 0$, the system is unstable, we call that the “backward” motion.

The choice of the sense of motion is the first point of interest in the next chapter’s analyses. It will be revealed, whether or not open-loop stability is an important issue and to what extent.

A first idea can be given by physical experience, given that the model without motors describes the dynamics of a supermarket-cart or of a wheelchair. Experiments have been carried out and the observations are presented Figure 3.7. A cart was observed while it ran down a slight slope: in the “forward” unforced motion, it showed little waves about a linear trajectory; in the “backward” unforced motion, the cart repeatedly rotated on itself and almost overturned. The analogy to Leonard’s dynamics are not extended because it is believed that other factors may have a role. But the distinction between “forward” and “backward” behaviors is demonstrated.

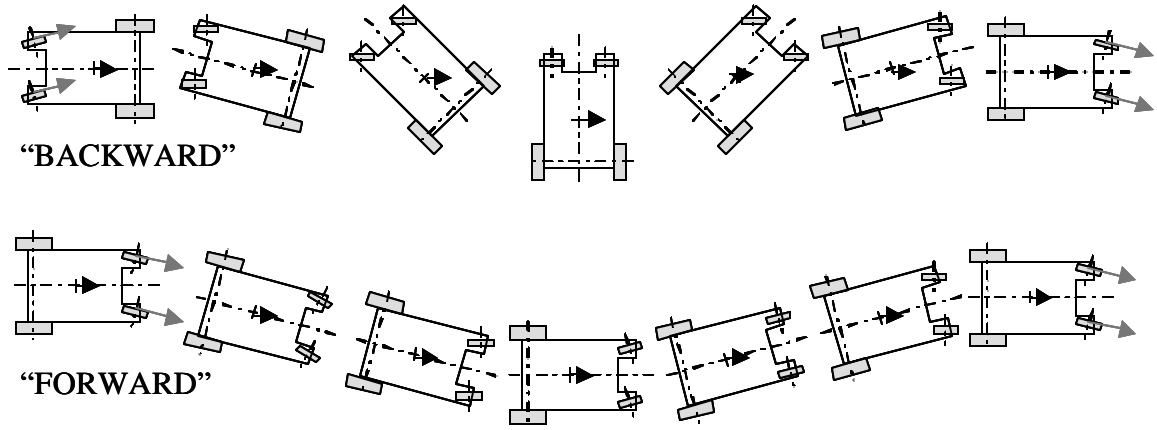


Figure 3.8. Experimental Observations for Backward and Forward Motion

CHAPTER IV

NAVIGATION AND CONTROL

Given the state space dynamic model derived in the last chapter, Modern Control theory for MIMO systems can be used to design an optimal navigation system. In this regard, a Linear Quadratic Gaussian regulator (LQG regulator), composed of a Kalman Filter and of a Linear Quadratic Regulator (LQR), will be designed. It fulfills the function described Figure 2.1 required to make Leonard follow a predefined trajectory.

In the early sections, the optimal estimator (Kalman filter) is designed and Covariance Analyses provide useful information concerning the vehicle's configuration. This is performed, first for the model without motors, then for the whole system. At the end of the chapter, statistical tools are used to tune the optimal controller and to predict results on the behavior of Leonard in closed-loop operation.

4.1 Introduction and Noise Modeling

In absence of any empirical data, the estimation of errors is the only way to get an insight in the future behavior of Leonard.

The preceding chapter ended up with an observable and controllable continuous state space model (72) and (73), or (72) and (74) in the general form:

$$\vec{\dot{x}} = F\vec{x} + G\vec{u}$$

$$\vec{y} = H\vec{x}$$

But this model ignored the effects of certain noise sources which will exist in practical operation. In addition, the use of digital technology for control imposes the need to discretize the model. The following system describes the linear discrete state

space equations corresponding to the previous continuous system, including process and sensor noises.

$$\overrightarrow{x}_{k+1} = \Phi \overrightarrow{x}_k + \Gamma \overrightarrow{u}_k + \Gamma_d \overrightarrow{w}_k \quad (75)$$

$$\overrightarrow{y}_k = H \overrightarrow{x}_k + \overrightarrow{v}_k \quad (76)$$

where: Φ : is the discrete state matrix (obtained with the Matlab function ‘‘c2d’’)

Γ : is the discrete input matrix (idem)

Γ_d : is the process noise matrix defined below

\overrightarrow{x}_k : state vector at time $k \cdot T_s$, where T_s is the sample time.

\overrightarrow{y}_k : output vector at $k \cdot T_s$

\overrightarrow{u}_k : input vector at $k \cdot T_s$

\overrightarrow{w}_k : is the process noise vector at $k \cdot T_s$

\overrightarrow{v}_k : is the sensor noise vector at $k \cdot T_s$

It is assumed that the noise vectors have zero means, are independent of each other, independent between samples, and are derived from a Gaussian random distribution with a fixed and known covariance.

While the sensor covariance values are quite easy to determine thanks to the suppliers’ specifications, the process disturbance estimation requires some modeling. Usually, experimental data are very useful to identify process noise characteristics [O’C97]. At this stage of the design however, the best that can be done is to build a model as accurate as possible. This leaves room for rectifications once Leonard is put in real life situations.

4.1.1 Sensor Noise. The sensor covariance is defined on the bases of the standard deviations of the GPS and of the encoder's measurements.

The carrier phase DGPS system should provide measurements with an accuracy as low as [Mis99]:

$$\sigma_{\text{GPS}} = 0.02\text{m} .$$

For the encoders (used as angular velocity sensors), the limiting factors are the resolution and the accuracy. The supplier ensures that the sensor never misses a pulse. Therefore, over one sample time, there are only three ways of getting an error on the measurement: (1) the sampling period can begin just after a pulse has been triggered, so that the angle corresponding to this pulse would not be accounted, (2) same situation for the last pulse, (3) the accuracy on the starting pulse and on the last one results in an error equivalent to one pulse (width about 10 arc-min). (See Appendix A.)

Finally, the standard deviation due to the encoders can be written as:

$$\sigma_{\text{ENC}} = \frac{3}{\text{RPS} \cdot \text{resolution} \cdot T_s} \omega_M$$

with:
$$\text{RPS} = \frac{V_{y0}}{2\pi R} N$$

and
$$\omega_M = \frac{V_{y0}}{R} N$$

$$\sigma_{\text{ENC}} = \frac{3 \cdot 2\pi}{\text{resolution} \cdot T_s}$$

where the “resolution” is the number of pulses per revolution that the encoder delivers (we chose a 1000 PPR encoder according to the analysis Section 4.3.3)

4.1.2 Process Noise. Computing the process noise requires a few more steps. Because it is dependent on the position of the point we wish to control (point C), the process noise is derived at point A, fixed on Leonard. Then, it is transferred to C using a state transformation matrix.

There were two main assumptions used to derive the dynamic model, which we take into account here: (1) the flatness of the ground and (2) the slip of the wheels. Indeed, in real life, the ground may not be perfectly flat. And Leonard's wheels may slip for many reasons, for example a lack of adherence or a hit into an obstacle.

The non-flatness of the ground is modeled according to the Figure 4.1. Two parameters are identified: θ_G : the angle of the ground's slope (referenced to the horizon) and A_z : the azimuth of the vehicle on the slope. Assume that the slope angle is small:

$$\sin\theta_G \approx \theta_G \text{ and } \cos\theta_G \approx 1$$

Also, since we want to model all possible scenarios, the azimuth must be chosen such that its effects be representative of the average behavior of the vehicle: A_z is such that:

$$0^\circ < A_z < 180^\circ$$

Simulations have shown that average behavior is exhibited when

$$A_z = 45^\circ .$$

The force exerted by the gravity is the term which introduces an error in the dynamic model derived earlier (equations (21), (24) and (25)). Now, let δx , δy , $\delta\phi$, and their differentiated forms, be the errors on the states due to neglecting gravity.

We have: $\delta\ddot{y} = -g\theta_G \cos A_z$ and $\delta\ddot{\phi} = \beta mg\theta_G \sin A_z$

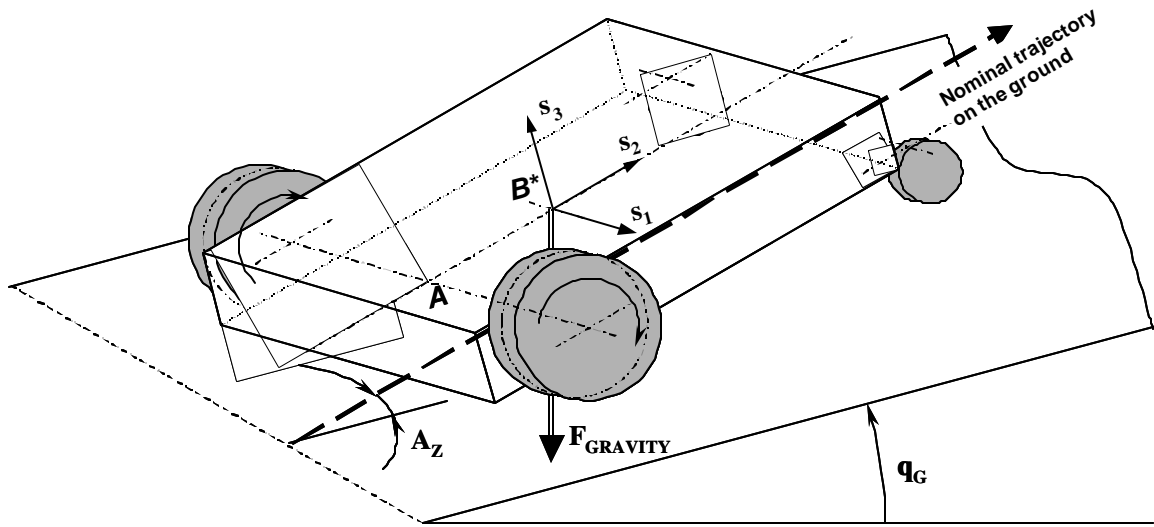


Figure 4.1. Process Noise Parameters Implied by the Non-Flatness of the Ground

Integrating the two preceding equations over the sample time T_s (with initial errors at zero) results in:

$$\delta y = -T_s g \theta_G \cos A_z \quad (77)$$

$$\delta \dot{\phi} = T_s \beta m g \theta_G \sin A_z \quad (78)$$

And again, integrating over T_s :

$$\delta y = -\frac{T_s^2}{2} g \theta_G \cos A_z \quad (79)$$

$$\delta \phi = \frac{T_s^2}{2} \beta m g \theta_G \sin A_z \quad (80)$$

Also, over T_s ,

$$\delta x = -V_{y0} T_s \delta \phi,$$

therefore:

$$\delta x = -V_{y0} \frac{T_s^3}{2} \beta m g \theta_G \sin A_z \quad (81)$$

The skidding of the wheels can occur for many reasons (loss of adherence, obstacle, etc.); it is modeled according to Figure 4.2. The assumed scenario is the following: one of the wheels slips instantaneously, at time $t=t_0$, by an amount θ_s radians, and the disturbance's effects are maintained till $t=t_0+T_s$.

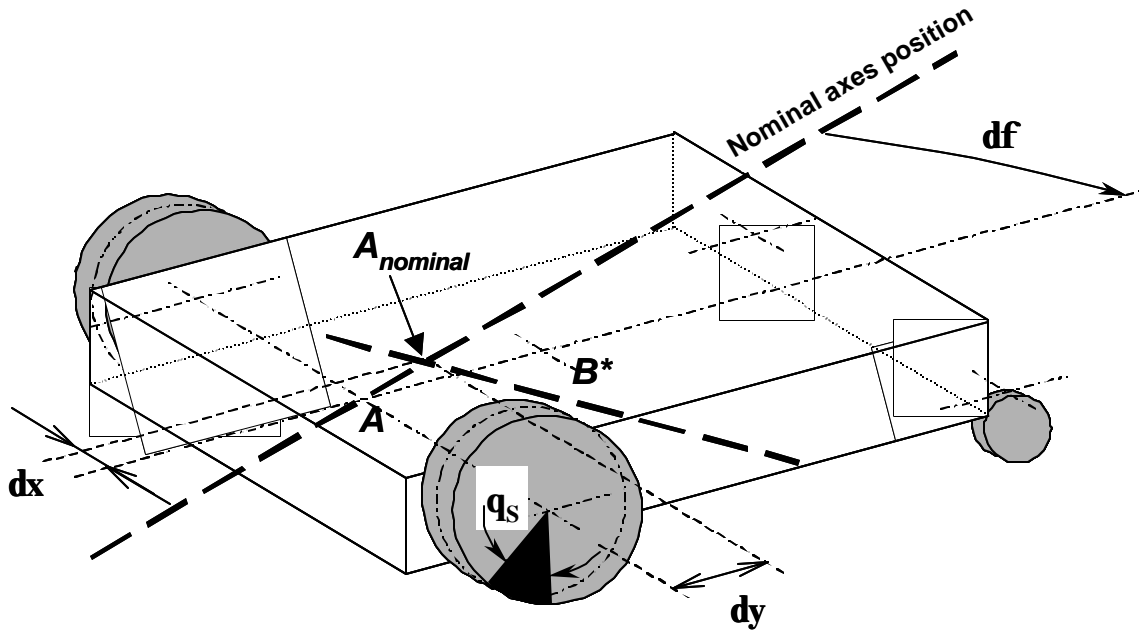


Figure 4.2. Process Noise Parameters Implied by the Slip of a Wheel

Assume that θ_s remains small: $\sin \theta_s \approx \theta_s$ and $\cos \theta_s \approx 1$.

For the position state variables, the instantaneous slip (at $t=t_0$) creates:

$$\delta y = -\frac{R}{2} \theta_s, \quad \delta \phi = \frac{R}{W} \theta_s, \quad \delta x = 0$$

Which, at $t=t_0+T_s$, results in:

$$\delta y = -\frac{R}{2} \theta_s \quad (82)$$

$$\delta \phi = \frac{R}{W} \theta_s \quad (83)$$

$$\delta x = V_{y0} T_s \delta \phi = V_{y0} \frac{R T_s}{W} \theta_s \quad (84)$$

In the velocity domain:

$$\delta \dot{y} = \frac{\delta y}{T_s} = -\frac{R}{2T_s} \theta_s \quad (85)$$

$$\delta \dot{\phi} = \frac{\delta \phi}{T_s} = \frac{R}{WT_s} \theta_s \quad (86)$$

4.1.3 Covariance Equations. Now, putting (77) to (86) in matrix form, $\overrightarrow{\delta x_k}$ being the error on the state vector:

$$\overrightarrow{\delta x_{k+1}} = \Gamma_d \overrightarrow{w_k} = \begin{bmatrix} -T_s \cdot g \cos A_z & -\frac{R}{2T_s} \\ T_s \cdot \beta m g \sin A_z & \frac{R}{WT_s} \\ -V_{y0} \frac{T_s^3}{2} \cdot \beta m g \sin A_z & -V_{y0} T_s \frac{R}{W} \\ -\frac{T_s^2}{2} \cdot g \cos A_z & -\frac{R}{2} \\ \frac{T_s^2}{2} \cdot \beta m g \sin A_z & \frac{R}{W} \end{bmatrix} \begin{bmatrix} \theta_G \\ \theta_s \end{bmatrix} \quad (87)$$

Then, given the input process noise covariance matrix (W), the process noise covariance matrix at point A on the states (Q_A) is established:

$$W = E \left[\overrightarrow{w_k} \cdot \overrightarrow{w_k}^T \right] = \begin{bmatrix} \sigma_{\theta_G}^2 & 0 \\ 0 & \sigma_{\theta_s}^2 \end{bmatrix},$$

$$Q_A = \Gamma_d W \Gamma_d^T$$

Standard deviations of $\sigma_{\theta_G} = 5^\circ$ and $\sigma_{\theta_s} = 10^\circ$ will be considered as being representative of the ground where Leonard evolves. These can be later modified and tuned experimentally.

Finally, the process noise covariance at point C on the states (Q_C) is obtained thanks to the state transformation matrix (T):

$$T = \begin{bmatrix} 1 & 0 & 0 & 0 & 0 \\ 0 & 1 & 0 & 0 & 0 \\ 0 & 0 & 1 & 0 & -L_A \\ 0 & 0 & 0 & 1 & 0 \\ 0 & 0 & 0 & 0 & 1 \end{bmatrix}$$

$$Q_C = TQ_A T^T$$

Back to (75) and (76), the covariance equations become:

$$X_{k+1} = \Phi \times X_k \times \Phi^T + \Gamma \times U_k \times \Gamma^T + Q_C$$

$$Y_k = H \times X_k + V$$

where: X_k : is the discrete state covariance matrix

Y_k : is the discrete output covariance matrix

U_k : is the discrete input covariance matrix

V : is the sensor noise covariance matrix:

$$V = E[V_k V_k^T] = \begin{bmatrix} \sigma_{ENC}^2 & 0 & 0 & 0 \\ 0 & \sigma_{ENC}^2 & 0 & 0 \\ 0 & 0 & \sigma_{GPS}^2 & 0 \\ 0 & 0 & 0 & \sigma_{GPS}^2 \end{bmatrix}$$

with the standard deviations σ_{ENC} and σ_{GPS} defined in the section 4.1.1.

Now that the necessary elements are evaluated, the Kalman filter can be developed.

For ease of explanation, first the model for the vehicle only (from Section 3.1), then the model with the motors (from Section 3.3), will be studied. Since the system is to be optimized for GPS measurements, the models without encoders will be used in a first place. The encoders will be added at the very end.

4.2 Covariance Analysis for the Vehicle Only

This section aims to provide sufficient arguments to fix most of the geometrical parameters of the vehicle while designing the Kalman filter. Eventually, an ideal configuration for Leonard is proposed and the expected errors on each state are estimated.

4.2.1 The Kalman Filter. The Kalman filter aims to provide an optimal estimation of the states given some measurements and a model of the plant [Fra98], [tTS74]. In Leonard's case, the measurements are provided by the GPS system and the discrete plant is modeled with the equations (75) and (76) derived previously.

The Kalman filter is a recursive process, which consists of two steps: (1) a measurement update, and (2) a time update, which can be expressed in terms of covariance by the following equations:

$$\hat{P}_k = \bar{P}_k - \bar{P}_k H^T (V + H \bar{P}_k H^T)^{-1} H \bar{P}_k \quad (88)$$

$$\bar{P}_{k+1} = \Phi \hat{P}_k \Phi^T + Q \quad (89)$$

where \hat{P}_k : is the estimated state covariance matrix at time $k \cdot T_s$

\bar{P}_k : is the propagated state covariance matrix at time $k \cdot T_s$

In this study, the steady-state Kalman filter is used (the covariance matrices are often referred to as \hat{P}_∞ and \bar{P}_∞).

In a first assumption, the sample time is taken such that:

$$T_s = 0.5s.$$

Also note that the standard deviation on \dot{x} can be computed, although it is not a state in the model considered, thanks to the relationship:

$$\sigma_{\dot{x}}^2 = \begin{bmatrix} -L_A & V_{y0} \end{bmatrix} \begin{bmatrix} \sigma_{\dot{\phi}}^2 & \sigma_{\dot{\phi}}\sigma_{\phi} \\ \sigma_{\dot{\phi}}\sigma_{\phi} & \sigma_{\phi}^2 \end{bmatrix} \begin{bmatrix} -L_A \\ V_{y0} \end{bmatrix}$$

At steady state, equations (88) and (89) can be used to determine the quality of the observation system (i.e. the standard deviations of the state estimate error). Sensitivity analyses can emphasize the influence of several factors on this observation system. Among those factors are: (1) the sense of motion, (2) the position of the GPS antenna. Both of them will be chosen to minimize the errors on the states. This method is schematized in the Figure 4.3.

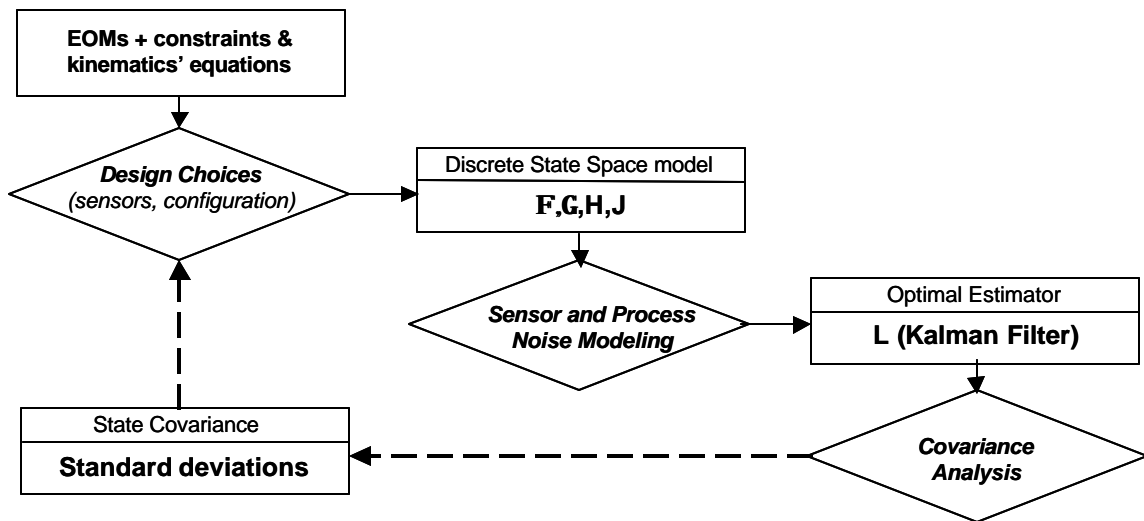


Figure 4.3. Design through Controls, Optimized for Optimal Estimation

Also, for clarity purposes, we assume the conventions symbolized in the Figure 4.4:

- the back of the vehicle is where the driving axle is
- the front is where the casters are
- driving forward (FWD) corresponds to a motion from back to front
- driving backward (BKWD) is the reverse motion.

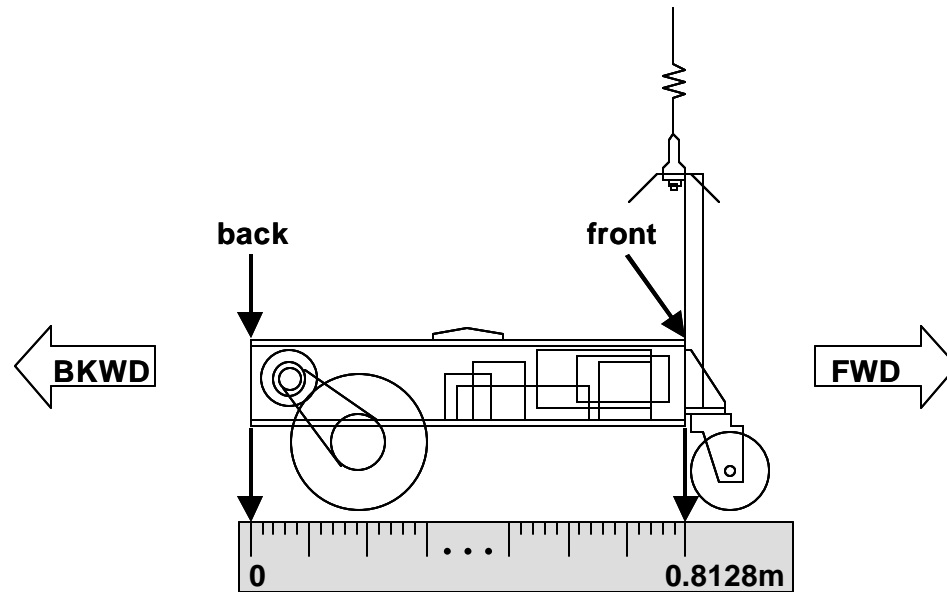


Figure 4.4. Conventions Used to Describe Leonard

The convergence of the covariance propagation process over time, for a given configuration of the vehicle, is presented in the Figure 4.5. Only three iterations are necessary to have the process reach its final value. Only steady states results are presented in the rest of the study, but it is important to understand that the convergence over time is not systematically guaranteed, namely if the system is not observable or unstable (see the next section).

The standard deviation on x , the cross track error, is the parameter we wish to minimize principally, and therefore, is of the main interest.

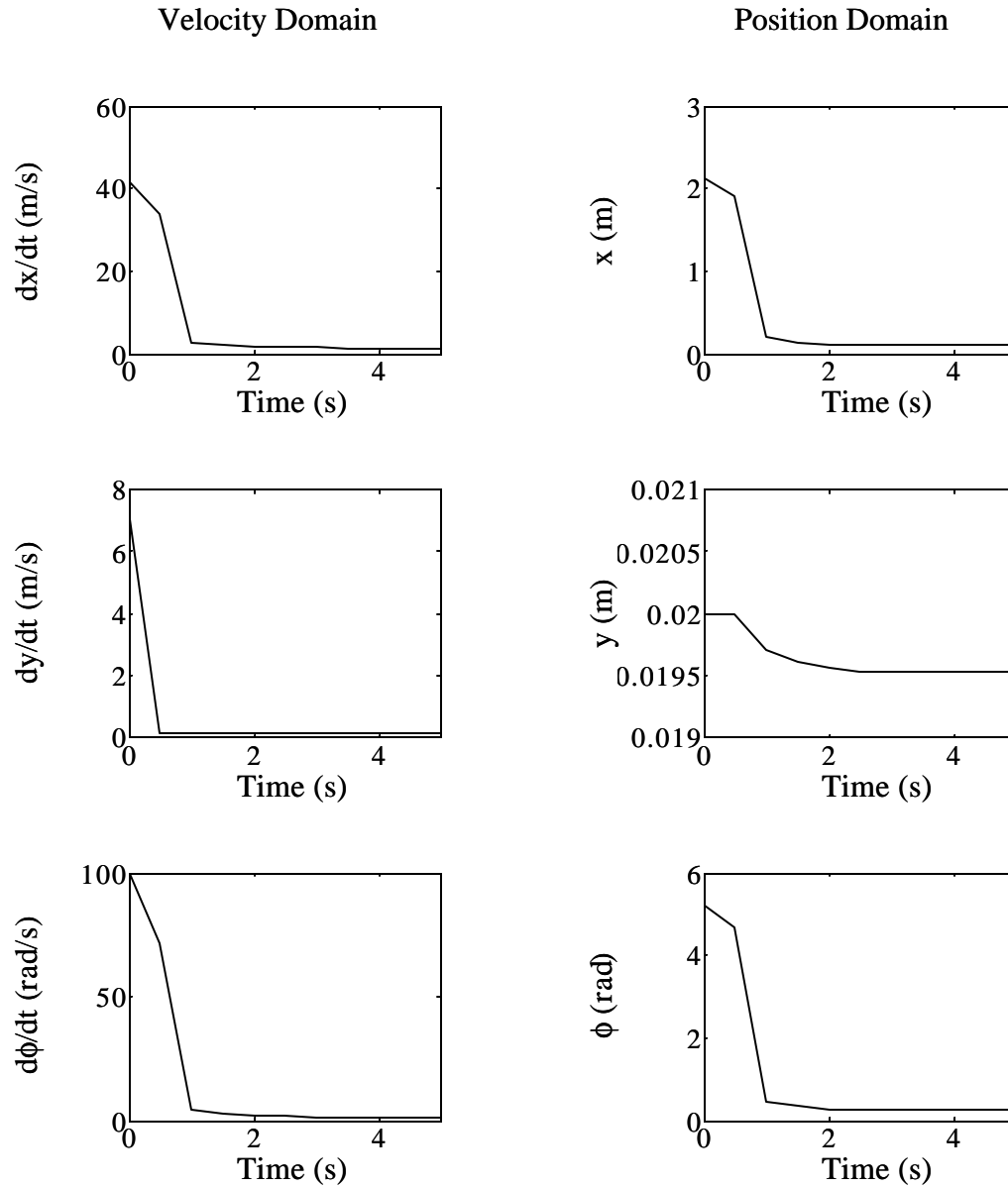


Figure 4.5. Convergence of the Covariance Propagation Process Over Time

4.2.2 Choice of a Sense of Motion. Recall that the location of the GPS antenna position (point S), the center of mass (B^*) and the point we wish to control (C) are distinct from one another. In this section, the plots are generated for a given position of C (C in the back) while the GPS antenna is moved all along the vehicle.

First, Figure 4.6 introduces the results for the forward motion. The cross track error, even in the worst case (S in the front), remains below 10cm. Its best value (2cm) corresponds to the point where S and C are coincident. In this case, the GPS system directly measures the cross track position.

Figure 4.7 shows the same plots for the backward motion. This time, the GPS antenna is moved farther in the front in order to include the evident singularity. Indeed, for an antenna location of about 0.83m of abscissa, all states' errors relative to the cross track ($\dot{x}, \dot{\phi}, x, \phi$: refer to Section 3.4.2) are subjected to a tremendous increase.

4.2.2.1 Point of Unobservability in Backward Motion. The exact location of this singularity is determined numerically per dichotomy; it reveals that, at this precise point, the system is unobservable. In order to obtain an analytical expression for the location of this singularity, recall the definition of observability: a system is said to be (state) observable if it is possible to determine the state vector $x(t_0)$ given observations of $y(t)$ over a finite time interval: $t_0 < t < t_f$.

In other words, for the cross track, the system is observable if it is possible to derive the three states x, ϕ and $\dot{\phi}$ from x_S and its differentiated forms. Using the sensor equation (45), the constraint equation (41) and the equation of motion for $\dot{\phi}$ (40), the preceding statement is translated into the observability equations:

The sensor equation \rightarrow (45)

$$x_S = x + L_S \phi$$

Differentiating it and substituting (41) for \dot{x}

$$\dot{x}_S = V_{y0} \phi + (L_S - L_A) \dot{\phi} \quad (90)$$

Differentiating it again and substituting (40) for $\ddot{\phi}$

$$\ddot{x}_S = (V_{y0} + \alpha(L_S - L_A)) \dot{\phi} \quad (91)$$

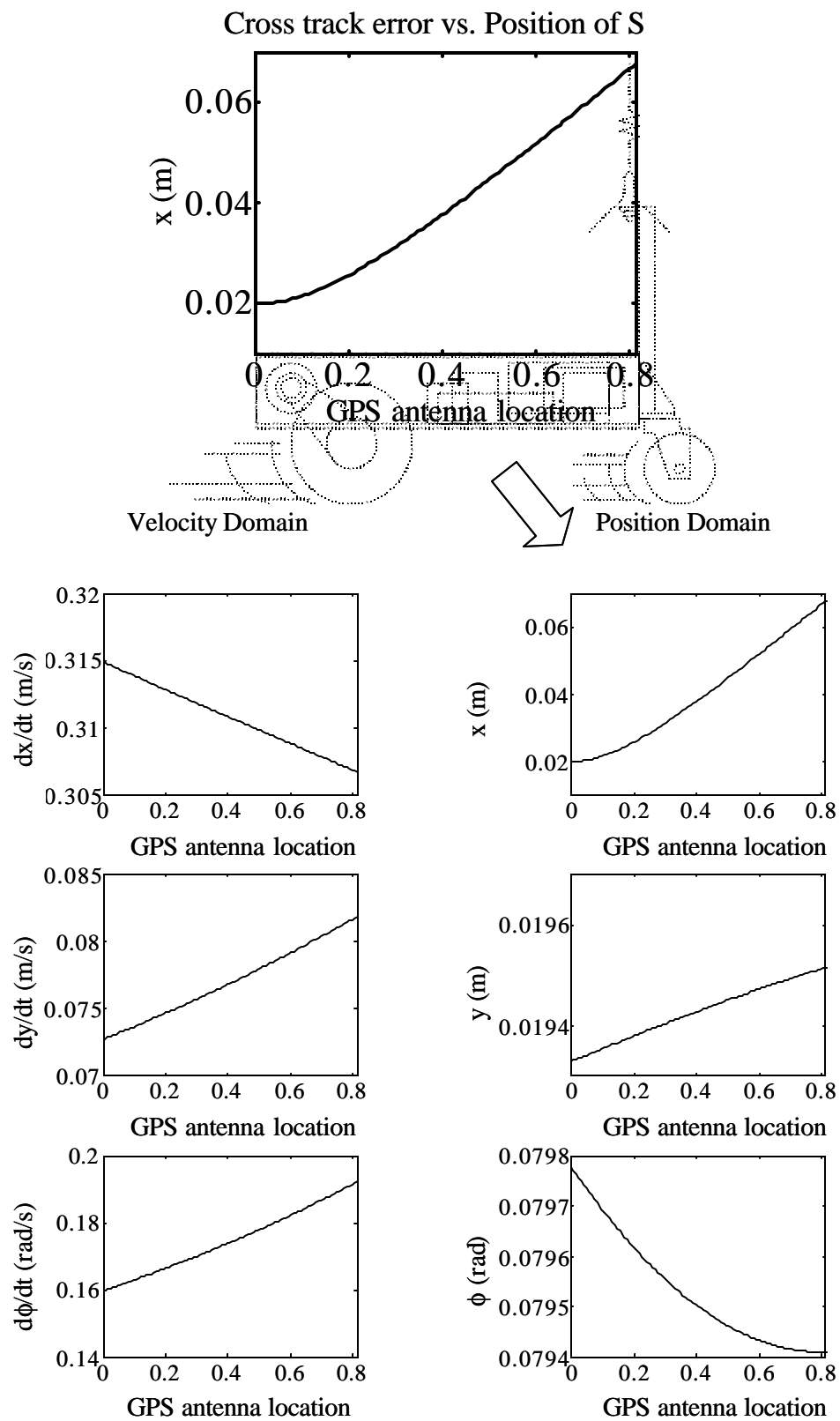


Figure 4.6. States' Standard Deviations for Forward Motion (Vehicle Only)

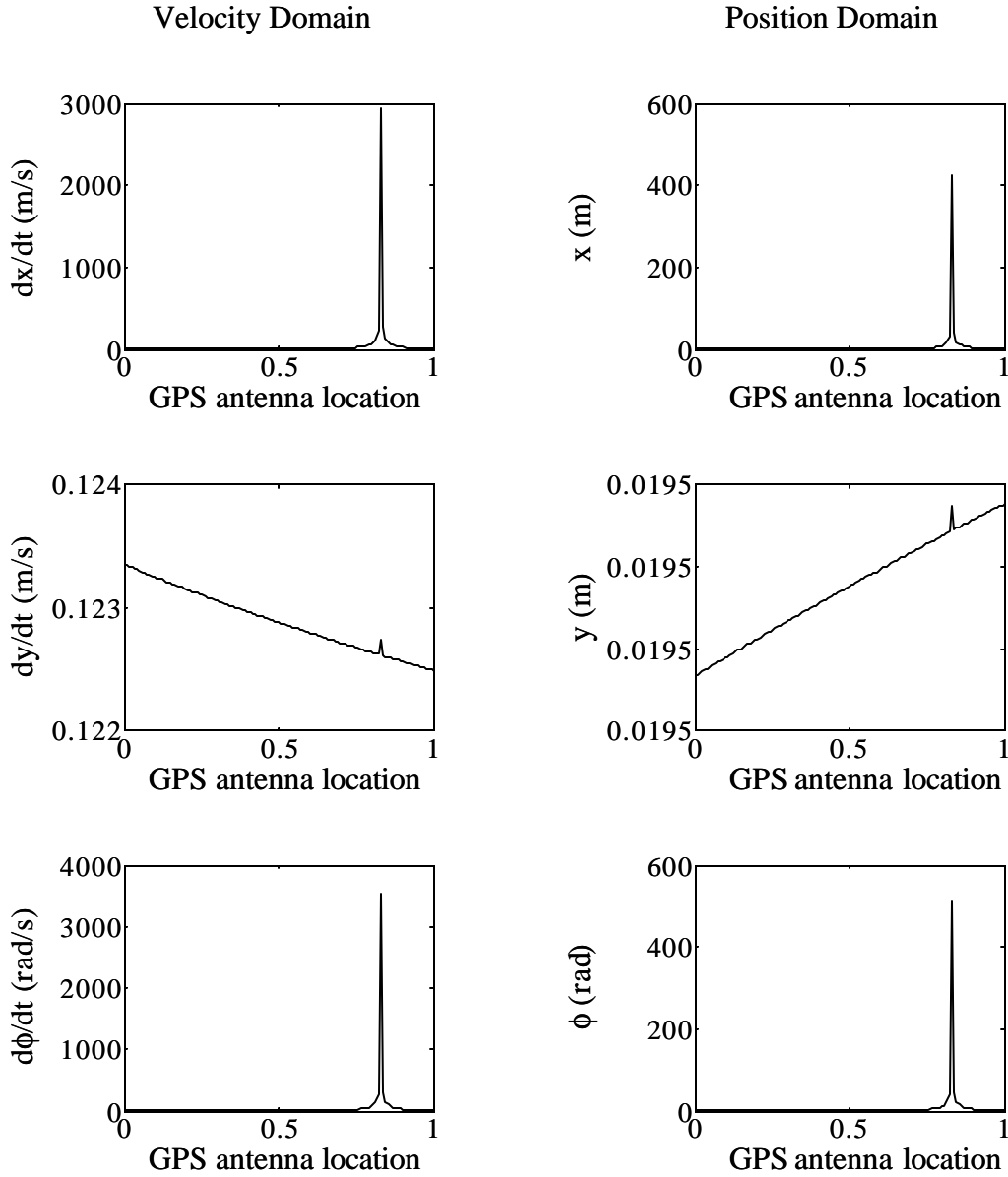


Figure 4.7. States' Standard Deviations for Backward Motion (Vehicle Only)

The three states are the three unknowns to be determined with those three equations. If one of these equations annihilates, there is no solution. There is one value for L_S (one position of the GPS antenna) for which the third equation's right term goes to zero:

$$0 = V_{y0} + \alpha(L_S - L_A) \quad \rightarrow \quad L_S = L_A - \frac{V_{y0}}{\alpha} \quad (92)$$

This is how the numerical value determined before ($L_S=0.8297\text{m}$) is recovered analytically. And this explains why the system is unobservable for this location of the GPS antenna. But this fact is valid in both senses of motion, so there must be a reason to why the unobservability is significant in backward motion and not in forward motion.

4.2.2.2 No Singularity in Forward Motion. Substituting the expression of α (37) into (92) underlines the non-dependency of the singularity with respect to the sense of motion:

$$L_S = L_A - \frac{J_A}{L_A - L_B}$$

Therefore, in forward motion, the system is unobservable as well as in backward motion, for this same location of the GPS antenna. The fact that this does not affect the results in one sense, whereas it does in the reverse motion, is related to stability. This subsection explains how the convergence of the state covariance matrix (illustrated Figure 4.5) depends on stability. Though the argument involves several stages, the mechanisms involved are worth studying since they will critically influence the results, namely depending on the choice of the motor (Section 4.3). To help the understanding, a summarizing scheme is proposed at the end of this section (Figure 4.10).

Consider Figure 4.8 recalling the covariance equations (88) and (89). Three steps are labeled (this is valid in a general case):

$$\hat{P}_k = \bar{P}_k - \bar{P}_k H^T (V + H \bar{P}_k H^T)^{-1} H \bar{P}_k$$

Step 3

$$\bar{P}_{k+1} = \Phi \hat{P}_k \Phi^T + Q$$

Step 1 Step 2

Figure 4.8. Three Steps in the Propagation of the State Covariance Matrix

- Step 1: the state covariance is propagated using the system transition matrix Φ
- Step 2: the process noise is added
- Step 3: the term associated with the new measurements is subtracted

In absence of measurements (no “Step 3”), the convergence of the state covariance (\hat{P}_k) depends on whether it is inflated or deflated by the transition matrix in “Step 1” as shown Figure 4.9. If it is deflated, the deflation itself is sufficient to compensate for the addition of process noise (from “Step 2”) and thus, to reach a steady state (lower right case on Figure 4.9). If it is inflated, the covariance diverges (lower left case). The system exhibits a stable or unstable behavior, respectively, for the lower right or left case. Note that this way of defining stability is consistent with the considerations of Section 3.4.2.

In order to apply these general statements to Leonard’s case, consider the state transition matrix:

$$\Phi = e^{F T_s} = \begin{bmatrix} 1 & 0 & 0 & 0 & 0 \\ 0 & e^{(T_s \alpha)} & 0 & 0 & 0 \\ 0 & -L_A \frac{(e^{(T_s \alpha)} - 1)}{\alpha} + \frac{V_{y0} (e^{(T_s \alpha)} - 1 + T_s \alpha)}{\alpha^2} & 1 & 0 & V_{y0} T_s \\ T_s & 0 & 0 & 1 & 0 \\ 0 & \frac{e^{(T_s \alpha)} - 1}{\alpha} & 0 & 0 & 1 \end{bmatrix}$$

Thus, the covariance propagation can be studied state by state. As a result, states x and ϕ always have a behavior corresponding to the left column in Figure 4.9. For $\dot{\phi}$ however, the propagation depends on the sense of α . The time-update covariance equation for $\dot{\phi}$ is:

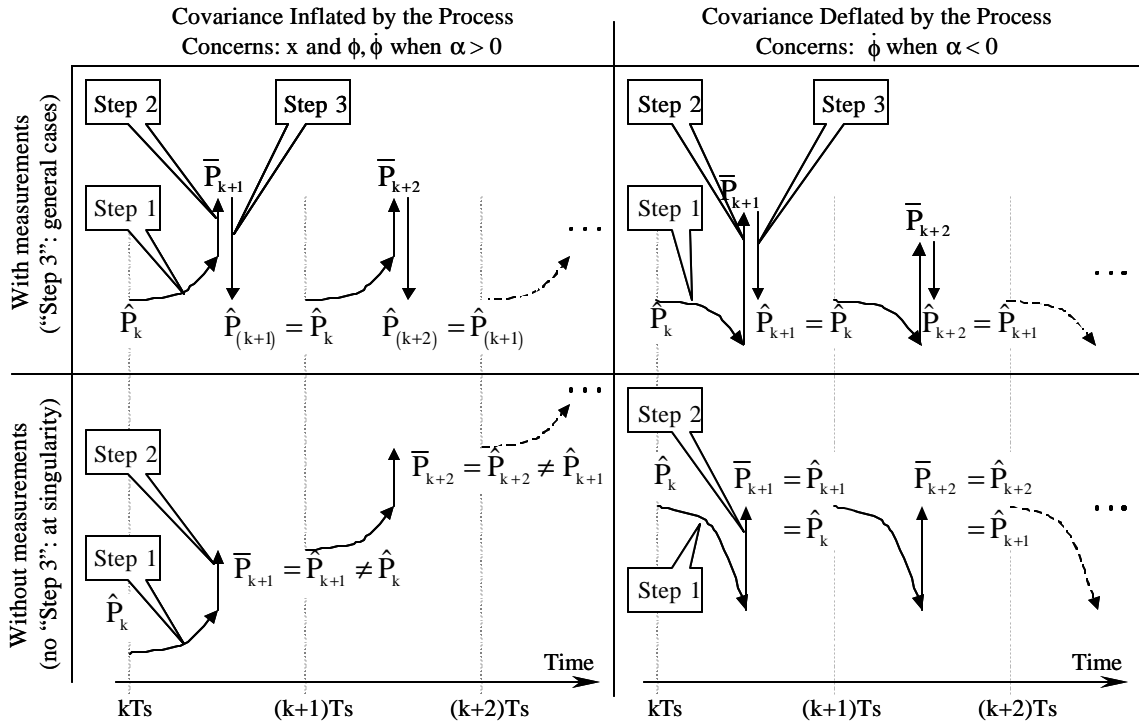


Figure 4.9. Four Cases for the Propagation of the State Covariance Matrix

$$\bar{P}_{k+1}(\dot{\phi}) = e^{2(T_s\alpha)} \cdot \hat{P}_k(\dot{\phi}) + \sigma_{\dot{\phi}}^2$$

where $\sigma_{\dot{\phi}}$ is the process noise standard deviation on $\dot{\phi}$.

- with α negative, \bar{P}_{k+1} is deflated (right column Figure 4.9)
- with α positive, \bar{P}_{k+1} is inflated (left column Figure 4.9)

In addition, consider the observability equations expressed at the location of the singularity (substitute (92) into (45), (90) and (91)):

$$x_S = x + \left(L_A - \frac{V_{y0}}{\alpha} \right) \phi \quad (93)$$

$$\dot{x}_S = V_{y0}\dot{\phi} - \frac{V_{y0}}{\alpha}\dot{\phi} \quad (94)$$

$$\ddot{x}_S = 0 \quad (95)$$

The fact that $\dot{\phi}$ reaches a steady state (when $\alpha < 0$) is sufficient to obtain the convergence for ϕ (from (94)) and for x (from (93)). On the other hand, if the covariance for $\dot{\phi}$ diverges, it also diverges for x and ϕ , and the unobservability expresses itself with infinite peaks (Figure 4.7).

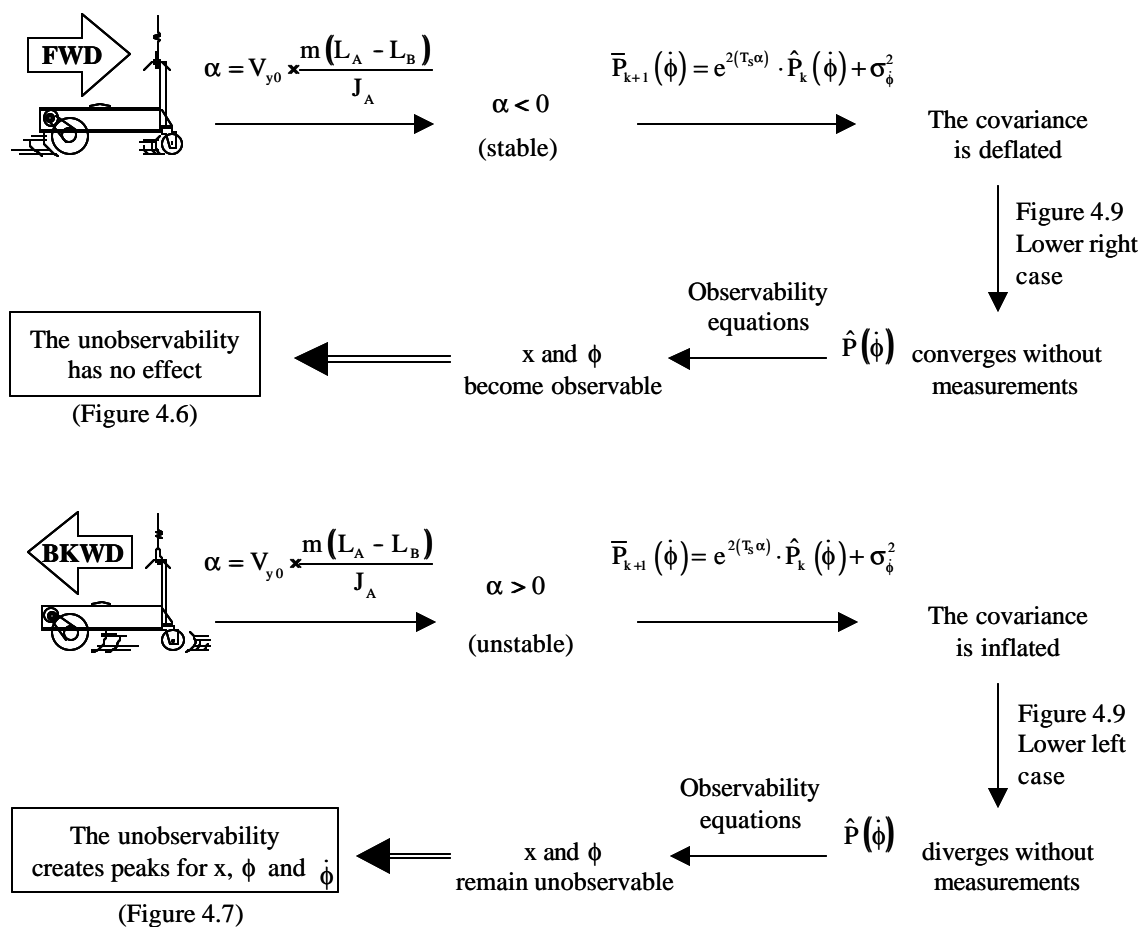


Figure 4.10. Summary of Section 4.2.2.2: What Happens at the Singularity

4.2.2.3 Changes in Position for B^* Modify Results in Backward Motion.

Equation (37) highlights the fact that modifying B^* is the only way the singularity can be pushed away in backward motion (V_{y0} is fixed). The larger the distance between the GPS antenna and the point of unobservability is, the lower the error on the cross track estimation will be. The idea here is to put most of the mass into half the total volume and to move it along the vehicle so that the center of mass changes. The result is the plot of the position of the singularity against the location of B^* (Figure 4.11).

Obviously, it is not possible to move all the mass in the very back of Leonard, otherwise the vehicle is unbalanced and tilts about the driving axle (black-hashed area).

The GPS antenna should be placed as far as possible from the singularity (black continuous-line). To symbolize the effect of the unobservability peak, an arbitrary threshold of 30cm on the cross track error is set: the gray area shows for which values of S and B^* , the errors are higher than 30cm.

Also, it is desirable to keep the GPS antenna on the main frame of the vehicle (i.e. without additional support to separate it from the singularity's location). Therefore only the area below the dashed line is considered.

Finally, only the white area below the dashed line is left. Note that even in this area, close to the threshold, the errors on the cross track remain close to 30cm. Given that it is not an easy task to manage the distribution of mass and to fix precisely the location of B^* , it is chosen to leave it in the middle and to clearly privilege forward motion. Proper placement of C and S could also improve the results.

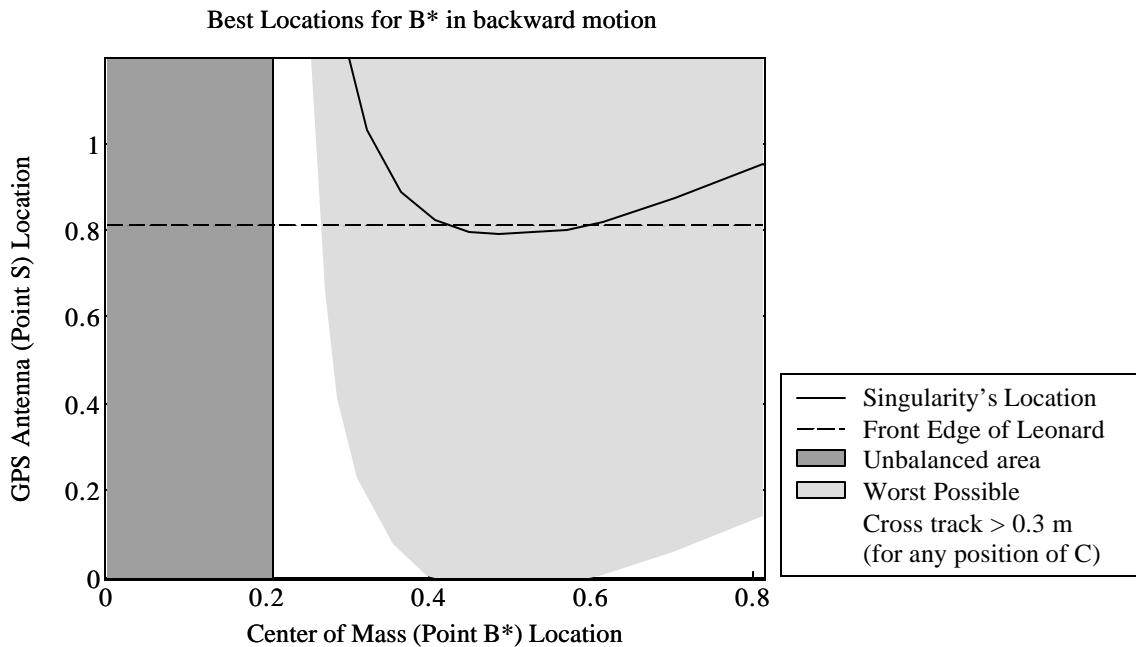


Figure 4.11. Choice for the Location of the Center of Mass

4.2.3 Optimal Position for S. For Figures 4.6 and 4.7, the control point (point C) was fixed in the back and the GPS antenna (point S) was moved along the vehicle. However, the position of C is relevant for the cross track error (x) as shown Figure 4.12.

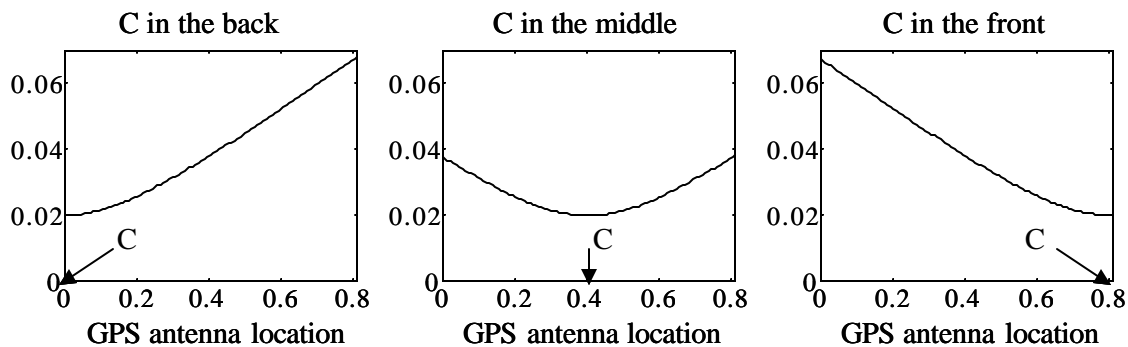


Figure 4.12. Influence of S on the Cross Track Error for Different Positions of C

It is desirable to maintain freedom in the choice of the control point: we may later want to control an embedded tool-point which may be subject to change depending on the mission. The goal then is to optimize S , considering all the possible locations of C . A three dimensional plot is generated in order to illustrate the combined effects of C and S on the cross track error (Figure 4.13). The three curves presented Figure 4.12 are highlighted in their respective planes.

Note the trough along the diagonal corresponding to the values where S and C are coincident. There, the cross track error actually corresponds to the GPS sensor standard deviation ($\sigma_{\text{GPS}} = 2\text{cm}$).

In order to obtain the optimized value for the GPS antenna location for any given position of C , the perspective indicated by the black arrow in Figure 4.13 is considered and presented Figure 4.14. This last figure shows the cross track error as a function of S for all possible values of C . The value of S for which this curve is at its lowest (abscissa

0.4m) is the one that minimizes the cross track errors for any position of C . Actually, this point is the intersection of the curves for the extreme positions of C on Leonard (C in the front and C in the back). This is how the exact value of the optimal abscissa for S is determined (Figure 4.15, left hand side).

For backward motion, the same study is performed. A three dimensional representation reveals that the extreme positions of C also fix the boundaries of the cross track error. In this case, the optimal position of S is in the back (Figure 4.15, right hand side). However, the difference in the cross track error, between placing the antenna in the back or in the middle, is less than one centimeter out of a total of 30cm of error. In contrast, in the forward motion case, placing the antenna in the back causes the cross

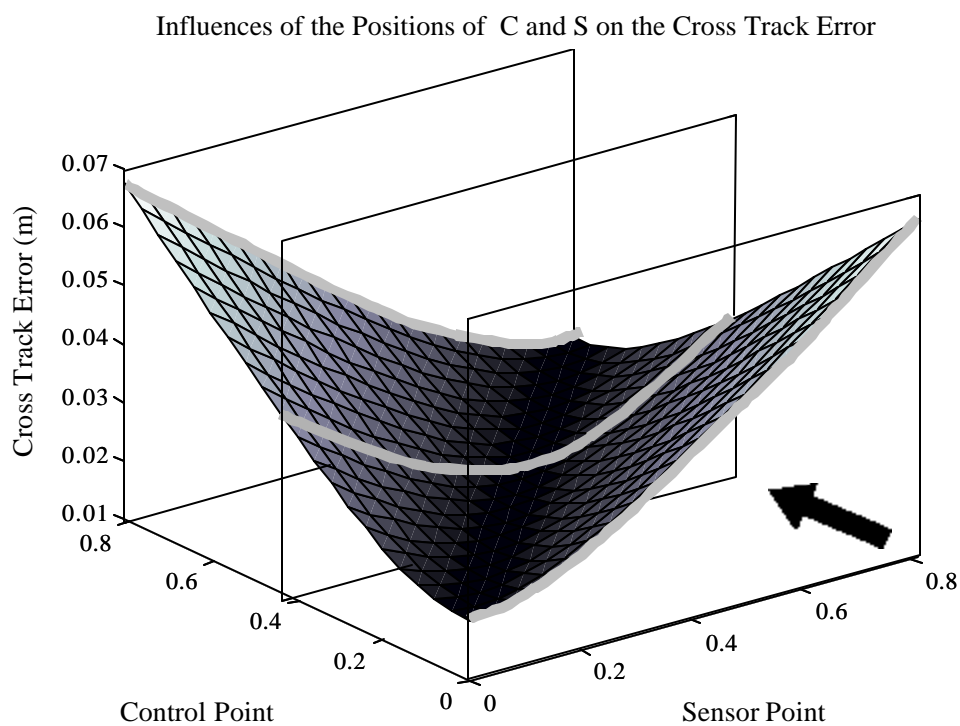


Figure 4.13. Three Dimensional Illustration of the Combined Influence of S and C

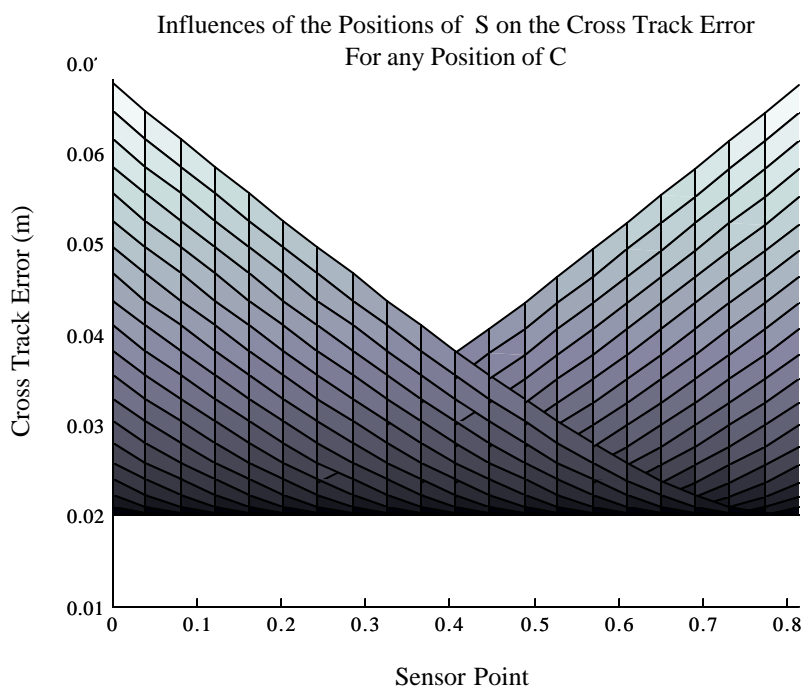


Figure 4.14. Different Perspective for the Figure 4.13

track error to nearly double from about 4 to 7cm. In this regard, the GPS antenna is finally fixed in the middle and the forward motion is privileged. This choice for antenna location has the additional advantage of being the best location on the vehicle to keep multipath effects low (Section 1.3).

4.2.4 Conclusions. The optimal configuration for the model without motors is summarized Figure 4.16.

For this given configuration, Figure 4.17 shows the cross track error against the position of C and highlights how much better the results are in forward motion. Note that, placing C in the middle makes the results insensitive to the direction of motion.

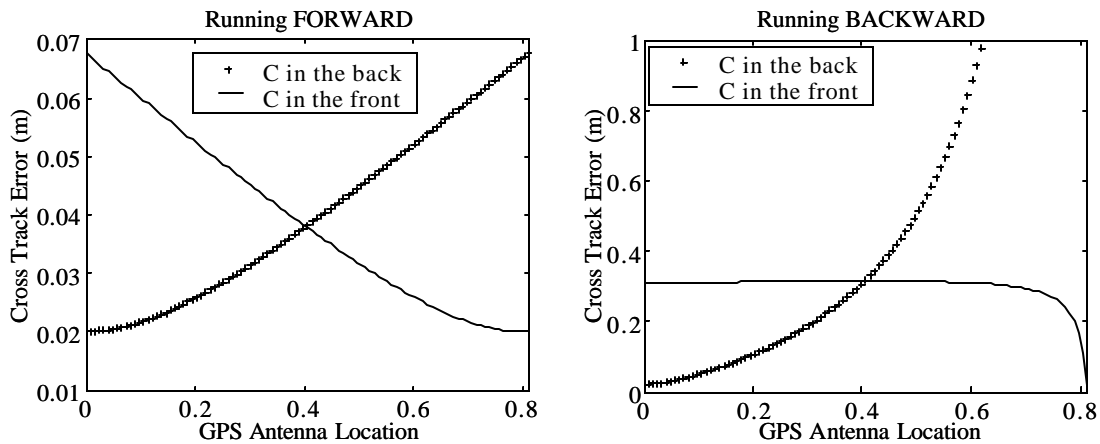


Figure 4.15. Cross Track Error vs. Position of S, for the Extreme Positions of C, for the Model With Torques as Inputs

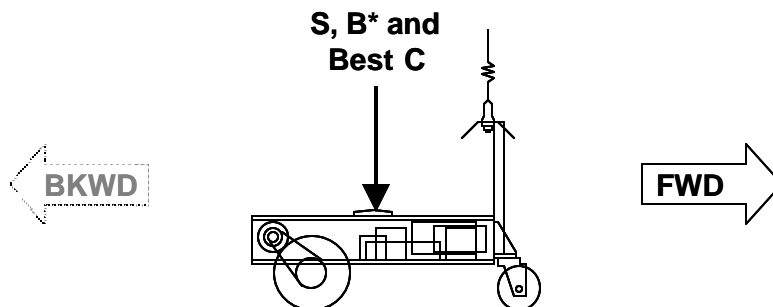


Figure 4.16. Optimal Configuration for the System Without Motors

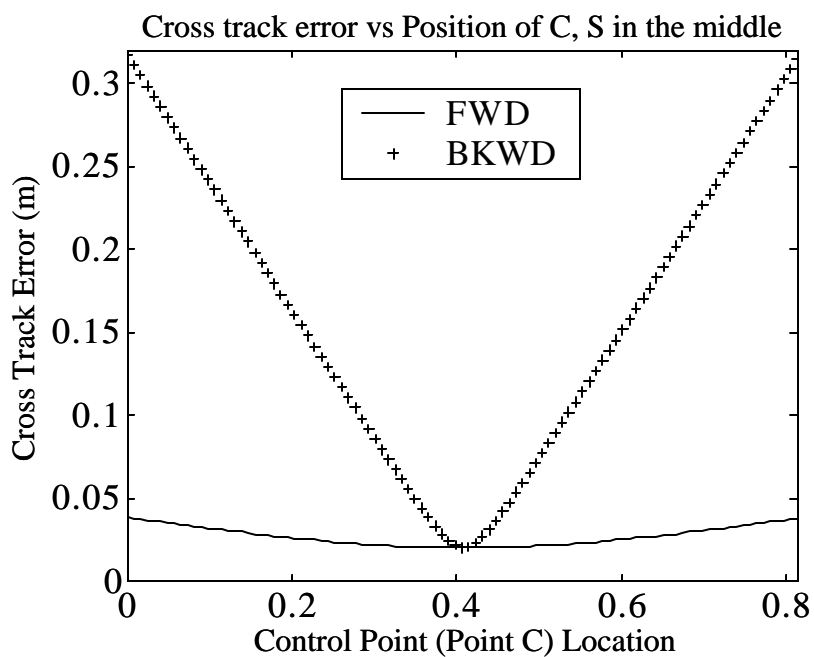


Figure 4.17. Cross Track Standard Deviation for the Best Configuration

4.3 Covariance Analysis for the Whole System including Motors

Depending on the motors selected, the behavior of the system can be modified compared to the one described above. Again, the positions of the GPS antenna, the center of mass and the sense of motion are optimized.

4.3.1 Comparison with the Preceding Analysis. The addition of motors can substantially improve the stability of the vehicle. The study of stability in Section 3.4 introduces the comparison between the two models (Figure 3.8). When the motors are included in the model, one of the poles (γ) is always negative, which improves the open loop system stability, and the parameter corresponding to α in the previous motor-free model, α' in equation (71), is modified to include motor parameters.

When going forward, α' is negative and the system is marginally stable, just like the motor-free model. In backward motion, for given motors, the only parameter which can change the sign of α' is again the location of the center of mass. Figure 4.18 shows how it influences the sign of the pole, the white area corresponding to the values for which the system is stable. Leaving B^* by the middle ensures stability in backward motion.

This characteristic is a considerable improvement compared to the system without motors where open loop system stability was not achievable in the backward motion. Indeed, now that the vehicle is stable in both senses of motion, unobservability issues are no longer significant. Actually, the results are so similar in either sense of motion (Figure 4.19) that only the forward motion case will be considered in the rest of the study.

It is noteworthy, however, that depending on the selection of the motor, the system can actually be quite similar to the motor-free model. An early attempt had been carried out using specifications for a “Magmotor C21-H-400”. In this case, the armature resistance (R_a) was 20 times lower than for the final selection. This caused $\alpha' > 0$ in backward motion, and the observability analysis of part 4.2.2 had to be taken into account. In the case where manufacturing reasons would impose a future change of motor, the necessary analytic tools are now available to anticipate any situation.

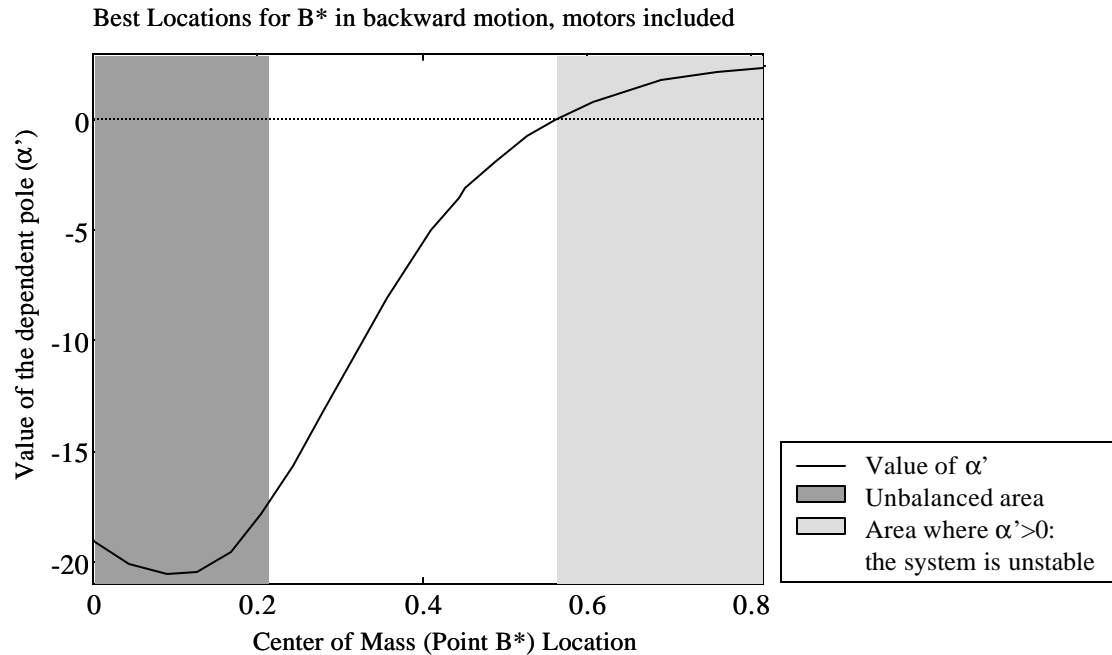


Figure 4.18. Influence of the Location of the Center of Mass on the Poles of the System

4.3.2 Optimal Position for S. In the same manner as for the Section 4.2.3, the location of the GPS antenna which minimizes the cross track error for any position of C can be determined (Figure 4.19): three dimensional plots show that the worst cases correspond again to the locations of C in the front and in the back. It results that the optimal location for S, for both backward and forward motion, is in the middle of the vehicle.

4.3.3 Improvements Brought by the Encoders. The first issue here was to determine whether adding the encoders could indeed improve the results. Again, the covariance analysis was used to answer this question in a quantitative way.

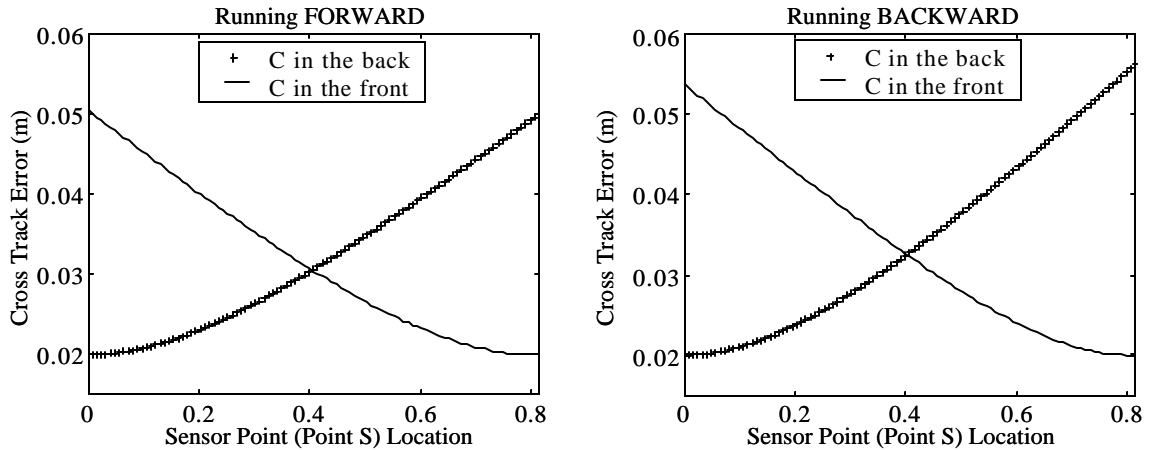


Figure 4.19. Cross Track Error vs. Position of S, for the Extreme Positions of C, for the Model With Voltages as Inputs

The Table 4.1 summarizes the gain brought by the encoders for each state. The numerical values are evaluated for a 1000 Pulses Per Revolution (PPR) encoder. There are minimum and maximum values for x and \dot{x} because the results are derived from simulations with all possible control point positions. The encoders are especially efficient in the velocity domain, which can be very important in the Kalman filter's iterative process in order to predict on-coming behaviors.

The supplier (Magmotor) delivers integrated encoders with the motors, with available resolutions of 500, 1000 and 2000 PPR. The Figure 4.20 shows the influence of the encoders' resolution on the errors. Although the 2000 PPR encoder gives the best results, there is actually little improvement in cross track (x) error (i.e., the error in the most critical state) relative to the 1000 PPR encoder. The marginal improvement in performance brought by a better encoder was judged not to be worth the additional cost.

Table 4.1. Improvements Brought by the Encoders

State	Without encoders		With encoders		Average Improvement Rate (%)
	Min.	Max.	Min.	Max.	
dx/dt (m/s)	0.2205	0.3252	0.0878	0.0953	66.45
dy/dt (m/s)		0.0572		0.003146	94.50
$d\phi/dt$ (rad/s)		0.1289		0.009232	92.84
x (m)	0.02	0.0305	0.0185	0.0222	19.41
y (m)		0.0183		0.007363	59.77
ϕ (rad)		0.0566		0.0206	63.60

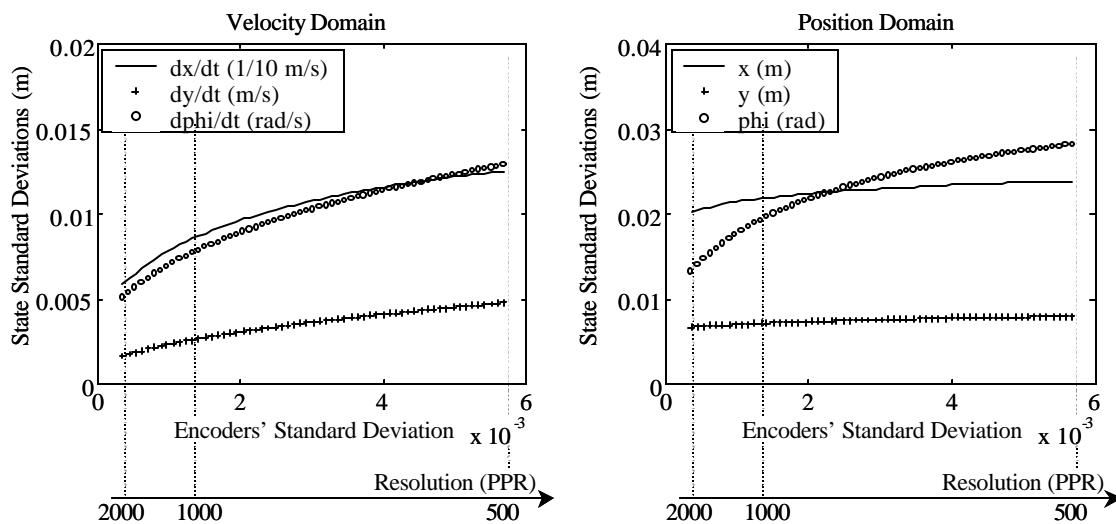


Figure 4.20. Selection of the Encoder Based on its Resolution

4.3.4 Conclusion of the Covariance Analysis. Finally, the standard deviations for each state are plotted in Figure 4.22 against the position of the control point, with and without encoders. The continuous lines indicate the final estimation of the errors, also listed in Table 4.1.

The final configuration, which will be concretely applied for the manufacturing of the prototype vehicle, is illustrated Figure 4.21. The location of the control point (C) may vary with vehicle application, with little performance impact as seen in Figure 4.22.

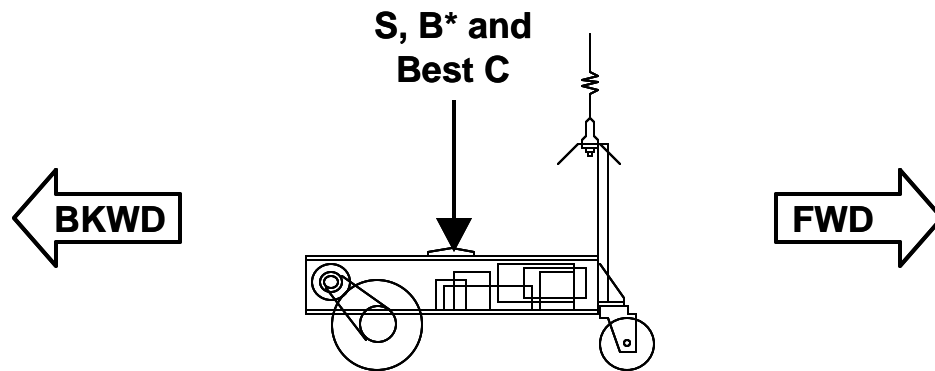


Figure 4.21. Optimal Configuration for the Whole System

4.4 The Optimal Controller

The Kalman filter has been determined in the preceding section. In order to complete the navigation system, the optimal controller is yet to be designed. Again, along with the elaboration of the controller, simulations will be performed in order to optimize the different design parameters, and a best configuration will be established, this time optimized for state control. Finally, a direct simulation will confirm the closed-loop analysis results.

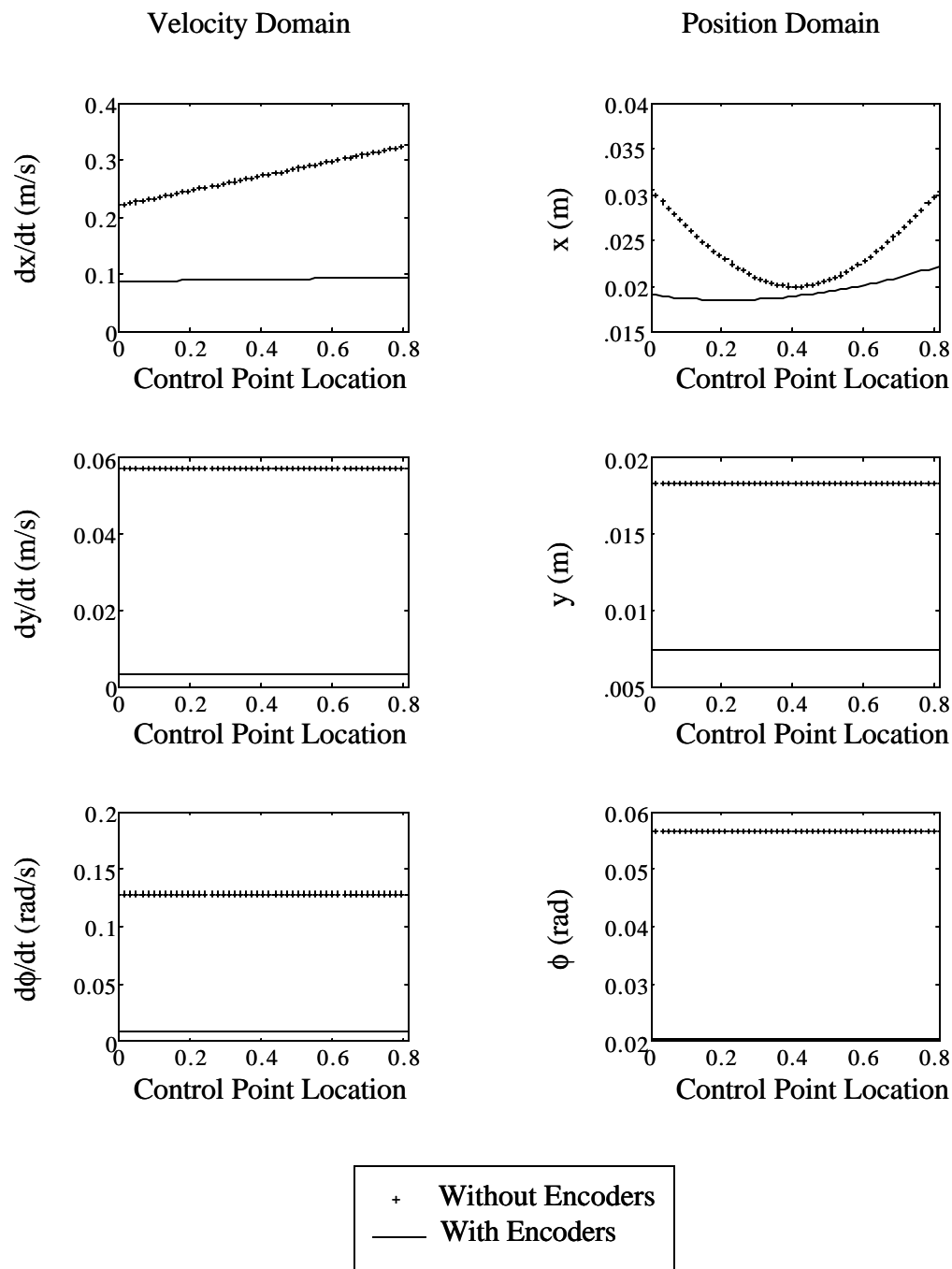


Figure 4.22. Final Results of the Covariance Analysis: Estimated Errors on Each State

4.4.1 Introduction and Determination of the Weighting Matrices. One particularly appropriate solution to control MIMO systems with state feedback is the use of a Linear Quadratic Regulator (LQR) [Fra98],[Bry75]. It is based on the control law:

$$\bar{u}_k = -K \cdot \bar{x}_k \quad (96)$$

where the feedback gain K is established by minimizing the cost function:

$$J = \frac{1}{2} \sum_{k=0}^{\infty} \bar{x}_k^T Q_1 \bar{x}_k + \bar{u}_k^T Q_2 \bar{u}_k$$

Q_1 and Q_2 are called the weighting matrices. Their relative choice fixes a balance between dynamic performances and actuator effort. Each matrix also weights the relative importance of each element of the state and control input vectors. In Leonard's case, it is desired to minimize the cross track error, whereas in track error is relatively less important (because the prescribed ground path will still be followed).

Designing the LQR basically consists in establishing the values of Q_1 and Q_2 . Sources (e.g. [Fra98]) recommend, as a first attempt, to pick Q_1 and Q_2 as diagonal matrices, where the non zero terms would be the inverse of the squared maximum desired values for each variable.

$$Q_1 = \begin{bmatrix} 1/\dot{y}_{\max}^2 & 0 & 0 & 0 & 0 \\ 0 & 1/\dot{\phi}_{\max}^2 & 0 & 0 & 0 \\ 0 & 0 & 1/x_{\max}^2 & 0 & 0 \\ 0 & 0 & 0 & 1/y_{\max}^2 & 0 \\ 0 & 0 & 0 & 0 & 1/\phi_{\max}^2 \end{bmatrix} \quad Q_2 = \begin{bmatrix} 1/u_{R\max}^2 & 0 \\ 0 & 1/u_{L\max}^2 \end{bmatrix}$$

The weighting matrices are modified until they lead to appropriate results, as determined by the closed-loop simulation.

A first attempt with the weighting matrices described above shows that the elements of the in track (states y and \dot{y}) have much better results than the other states; therefore it was decided to allocate less effort to control them by modifying Q_1 . After several iterations, the values for Q_1 and Q_2 are selected:

$$Q_1 = \begin{bmatrix} 0 & 0 & 0 & 0 & 0 \\ 0 & 50 & 0 & 0 & 0 \\ 0 & 0 & 400 & 0 & 0 \\ 0 & 0 & 0 & 0.01 & 0 \\ 0 & 0 & 0 & 0 & 100 \end{bmatrix} \quad Q_2 = \begin{bmatrix} 0.0017 & 0 \\ 0 & 0.0017 \end{bmatrix}$$

Real data from the vehicle in operating conditions may require modification of these values depending on the actual behavior of the vehicle.

4.4.2 Steady State Mean Square Performance of the Closed Loop System. The block diagram for the closed-loop system is presented Figure 4.23. The LQR and the Kalman filter are combined to create a Linear Quadratic Gaussian regulator (LQG regulator) which is the core of the navigation system. In this pre-manufacturing phase, the “Plant” stands for the real vehicle, and the random noises reflect the expected (but unknown) disturbances.

Lyapunov’s equations provide a tool to obtain the average value of the state standard deviation for the closed-loop system [Bry75]. After having tuned the weighting matrices as described above, sensitivity analyses can be performed. Again, optimal positions for the center of mass (B^*), the sensor point (S) and the control point (C) can be selected. It turns out that the configuration optimized for state estimation (Figure 4.21) is optimized for state control as well. The results are presented Figure 4.24.

Even though the weighting matrices have been tuned, the results are still poor: an approximation of the average cross track standard deviation gives about 40cm. Decreasing the sample time (T_s) improves this result; indeed, a closer look at the noise matrices reveals that it is an important parameter: it is actually cubed in the process noise matrix (87). Until now, it was fixed at $T_s=0.5s$, and there is a lower limit of 0.1s imposed by the GPS system. Taking $T_s = 0.2s$ results in an average cross track error less than 10cm. The improvements brought by this modification are listed Table 4.2.

Table 4.2. Improvements Brought by a Lower Sample Time ($T_s=0.5s$ and $T_s=0.2s$)

State	$T_s=0.5s$		$T_s = 0.2s$		Average Improvement Rate (%)
	Min.	Max.	Min.	Max.	
dx/dt (m/s)	0.3082	0.7192	0.0203	0.1072	87.59
dy/dt (m/s)		0.3045		0.1336	56.12
$d\phi/dt$ (rad/s)		0.7283		0.3422	53.01
x (m)	0.3755	0.4572	0.0706	0.0822	81.65
y (m)		0.4397		0.1707	61.18
ϕ (rad)		0.301		0.092	69.44

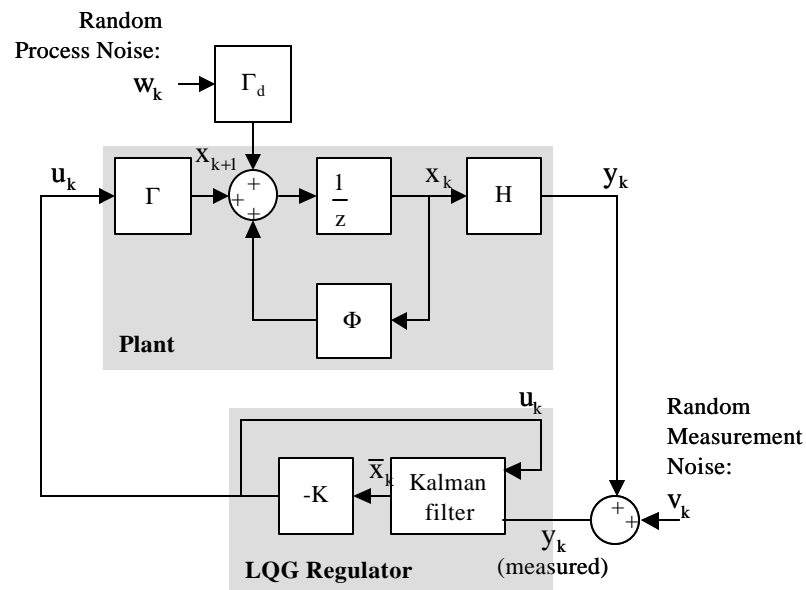


Figure 4.23. Block Diagram of the Closed Loop System

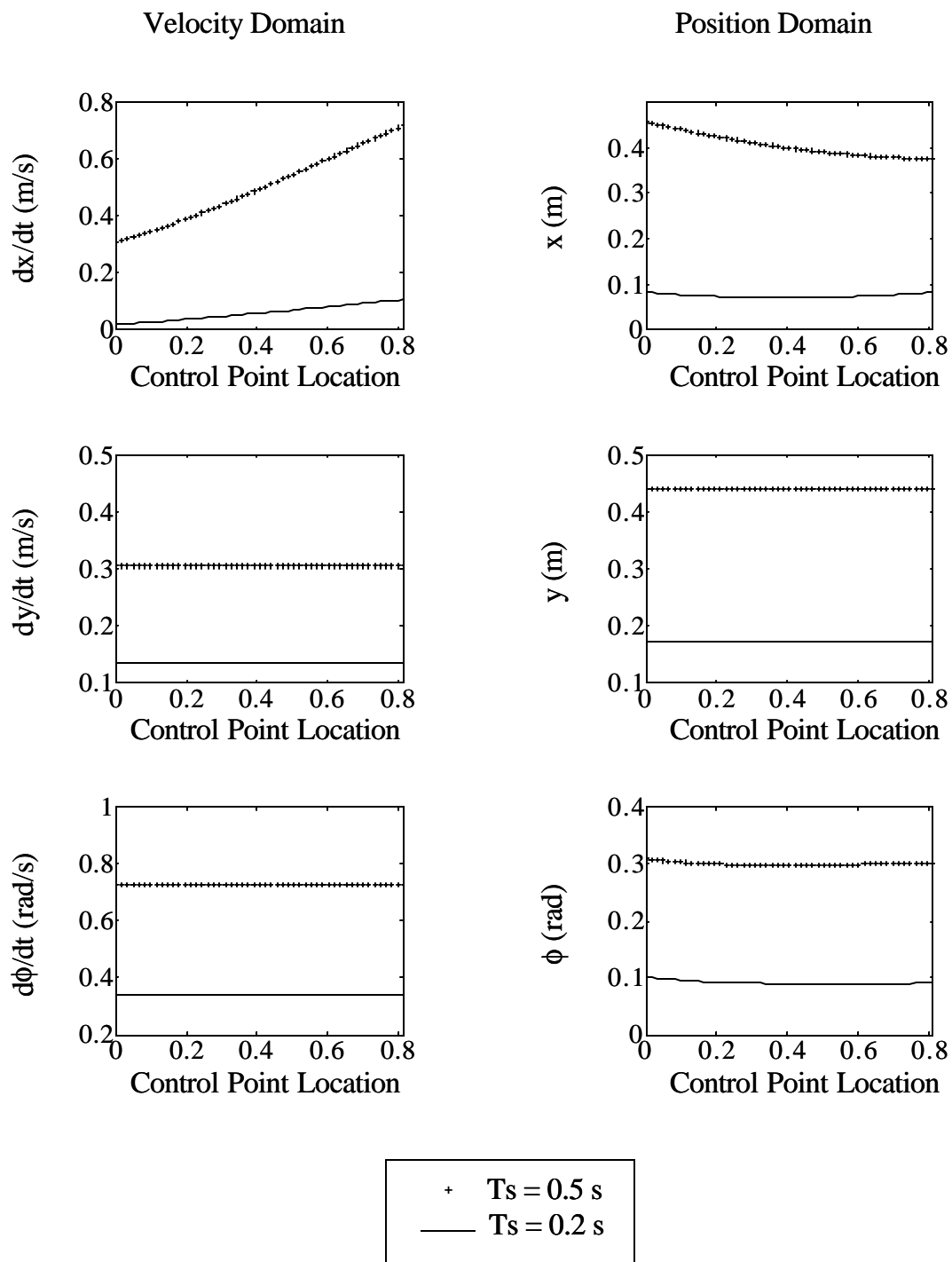


Figure 4.24. Results of the Closed-Loop Simulation Based on Lyapunov's Equations

4.4.3 Direct Simulation. Process and sensor noises can be generated with random numbers following a normal gaussian distribution. These are injected into the navigation system's simulation (Figure 4.23). As a result, direct simulations can be run for different parameter values, as illustrated Figure 4.25 for the best configuration. The final estimation with $T_S=0.2s$ confirms that the cross track standard deviation remains below 10cm, as suggested by the previous analysis based on Lyapunov's equations (Table 4.2).

The importance of the sample time is again demonstrated. Satisfying results are obtained choosing $T_S = 0.2$ seconds. For the moment, a reasonable range has been established (between 0.2s and 0.5s), but the only known limiting factor is the bandwidth of the GPS receiver tracking loops (10 Hz). From Figure 1.1 describing the DGPS process, considering that processing time may be negligible (~10msec), the lower limit for T_S is fixed by the time needed to transfer data from the reference station to the user. Before making any further assumptions in this regard, the data link must be implemented and tested. If all the delays add up to less than 0.2s, the dynamic performance is very promising. Otherwise, if it is in the range of 0.5s, further tuning of the LQG's parameters may be needed to improve the performance.

4.5 Conclusion

The goal of designing a navigation system is reached. The simulations of the closed loop system have predictably shown worse results than the estimator covariance analysis since the controller is also taken into account. Indeed, the vehicle's configuration has been optimized for both state estimation and state control.

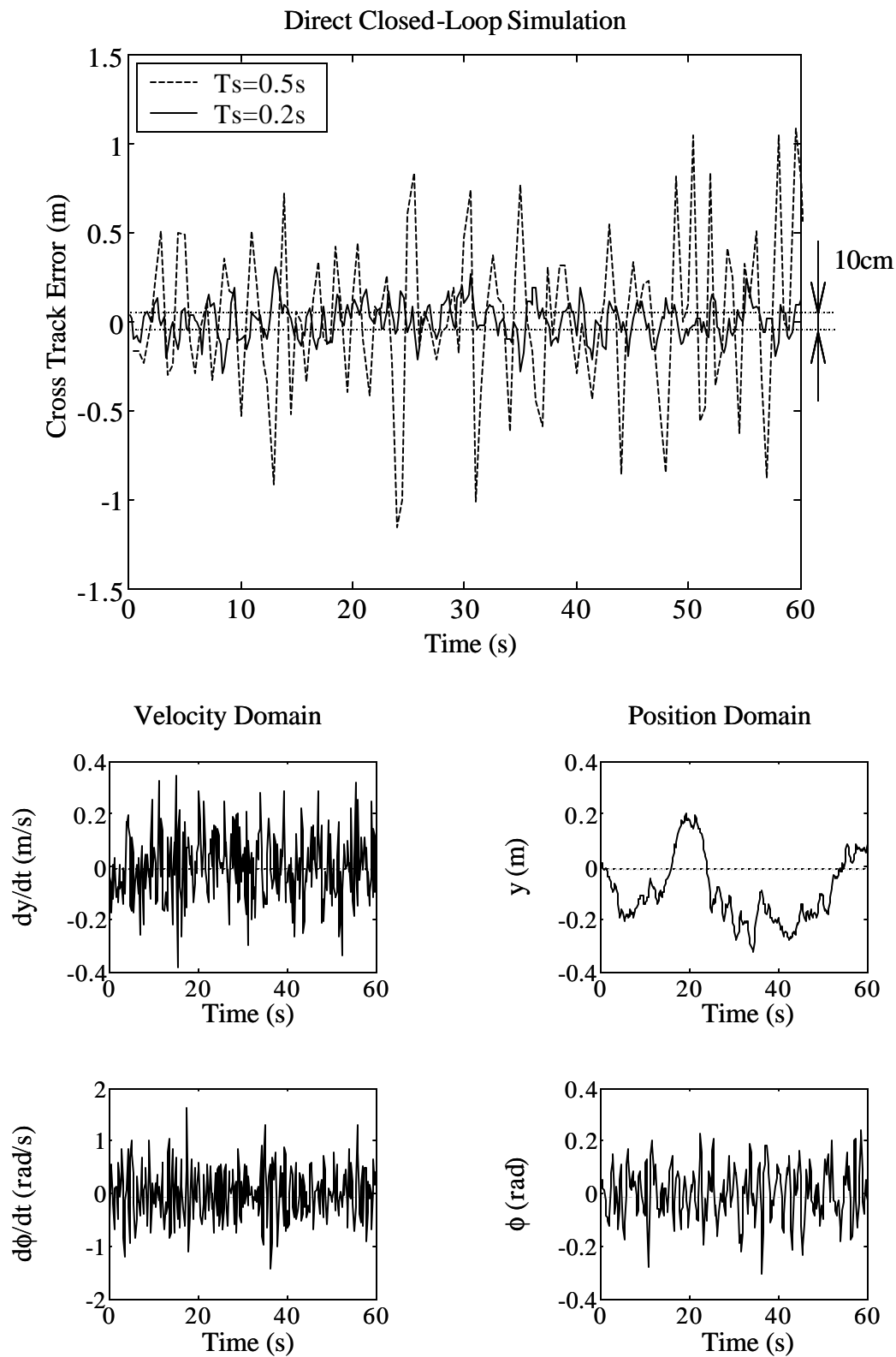


Figure 4.24. Results of the Direct Closed-Loop Simulation, for $T_s = 0.2\text{s}$

This project serves as a benchmark example of how controls system analysis can be used as an integrated element in overall vehicle design. The Figure 4.26 summarizes the method and can be used as a general guideline to design any servo-system.

However, the limits of the analysis have also been demonstrated. This work has reached the point where experimental data are definitely needed. Since all manufacturing parameters have been fixed, the construction of the real vehicle can begin. Once the system is put into operation, parameters like the sample time can be efficiently selected.

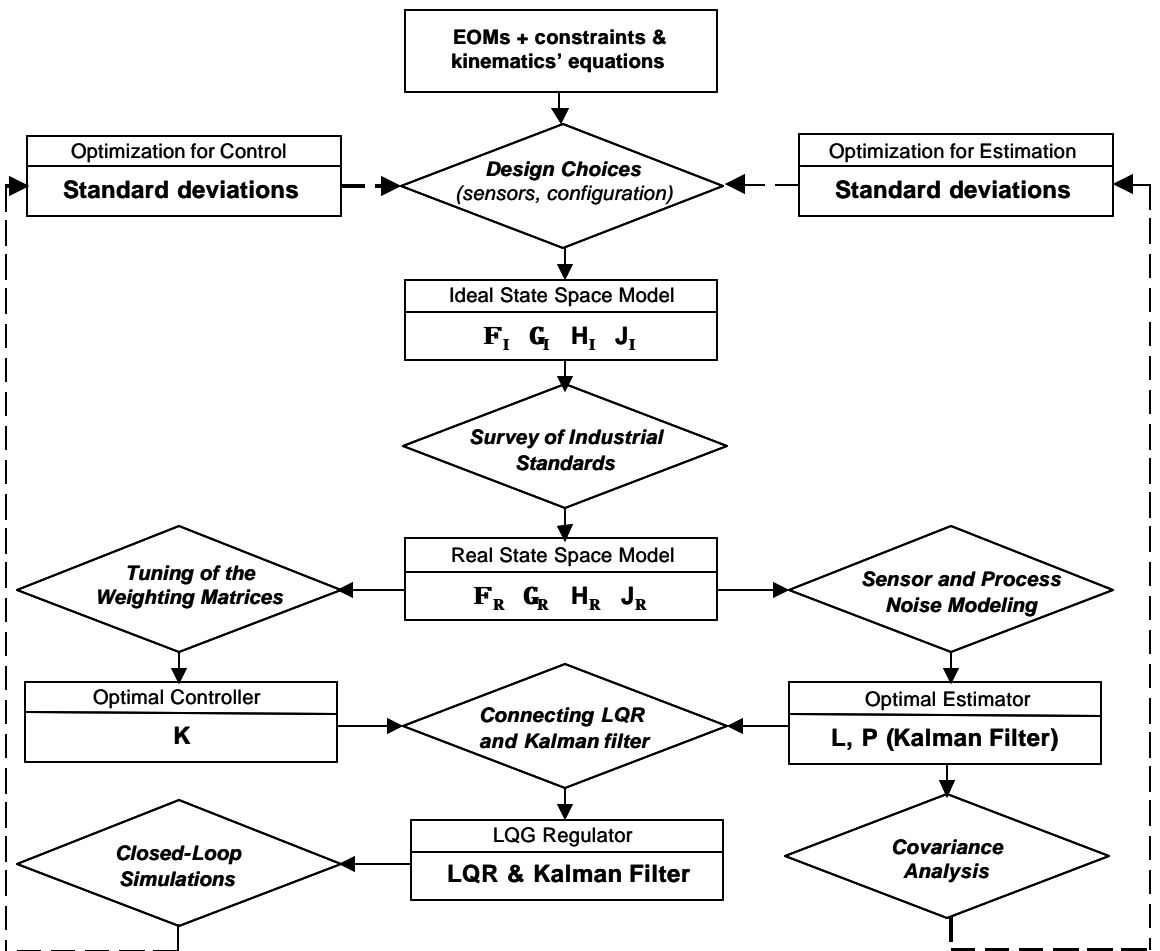


Figure 4.26. Method for Design through Controls

CHAPTER V

CONCLUSIONS AND PERSPECTIVES

The design of the automatic ground vehicle navigation system has finally been achieved. In the course of this study, many vehicle design parameters were optimized to obtain the best possible dynamic performance. At this point, a sufficient understanding of the vehicle has been acquired to begin the manufacturing phase and to plan for future experimental work.

5.1 Conclusions

This thesis describes the theoretical research behind the design of a GPS-based navigation system for an automated ground vehicle. The work was divided into three sections.

First, the Analytic Hierarchy Process was used to define a baseline design among numerous alternatives. Though more challenging because of the absence of prior literature, the differential drive design emerged as the most likely to meet our requirements.

Then, a dynamic model for the resulting non-holonomic system was derived independently using Newton, Kane and Lagrange's methods. Linearized about a nominal linear, constant velocity trajectory, the model including the motors was expressed as a state space realization appropriate for control system design.

Finally, the navigation system, which consists of a Linear Quadratic Gaussian regulator was developed. Covariance analyses and closed-loop simulations make it possible to optimize the system for both state estimation and state control. In this regard,

the positions of the center of mass and of the GPS antenna are selected to minimize the influence on the final performance due to variations in the location of the control point. In the same manner, appropriate encoders are selected and a first tuning of the control system is performed based on the simulations. Ultimate predictions on the vehicle's closed-loop behavior reveal that with a sample time of 0.2s, at a nominal velocity of 10mph, a cross track standard deviation less than 10cm is achievable.

Leonard's final design was the result of several iterations between these three steps. When simulations in the third step did not give satisfying results with respect to the dynamic performance, the first step was reconsidered and the necessary design modifications were made.

5.2 Future Work

Leonard may be the first of a series of vehicles built for the Navigation and Guidance Laboratory. Future work may imply the following items:

First of all, the benefit of having real experimental data is multiple: (1) the assumptions made for the dynamic model can be validated and questions concerning the sample time can be answered, (2) the navigation system can be tuned, in particular the controller's weighting matrices, (3) the final dynamic performance can be demonstrated.

Then, since the dynamic model was only linearized along a straight line at constant velocity, future work may imply linearizations for more complex trajectories.

Also, it might be interesting to equip Leonard with an obstacle detection system, first with bumpers alerting in case of collision, later with vision systems capable of detecting

obstacles without contact. Elementary algorithms added to the navigation system should be sufficient to drive around the unevenness of the terrain.

Leonard's primary purpose was to serve as a mobile platform to carry out GPS-based experiments. It will be particularly useful to demonstrate the complementarities between GPS and inertial sensors.

Finally, networks of independent AGV's like Leonard may quickly find industrial applications such as the realization of synchronized tasks in hazardous environments.

5.3 Closing

Judging by the way indoor AGV's have been quickly and widely adopted in the automotive industry, there is little doubt that outdoor vehicles will know a similar expansion. New GPS technologies have made it possible to control and navigate these outdoor AGV's, enabling their use in high precision applications. They will be particularly efficient for highly detailed missions that are unsafe or too difficult for human operation, such as the localization and removal of hazardous chemical, explosive, or radioactive waste.

APPENDIX A
SUPPLIERS' SPECIFICATION SHEETS



248-640 oz-in Continuous Torque

Key Performance Features

- UL Recognized
- CE Compliant
- Smooth 4-Pole Performance
- Dynamically Balanced Armatures
- 42 Bar Commutator
- Round or NEMA 42 Mounting
- ISO 9001:2001†

C40 BRUSHED
SERVO
MOTOR
SERIES

Motor Characteristics

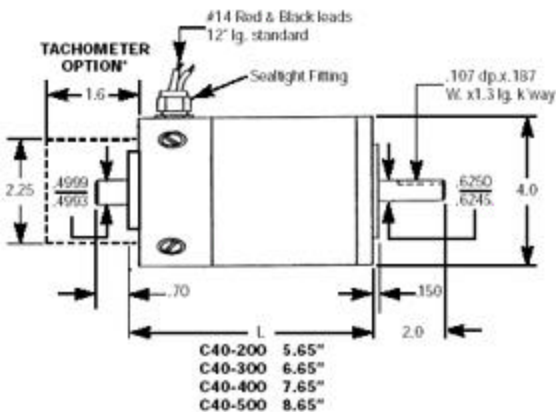
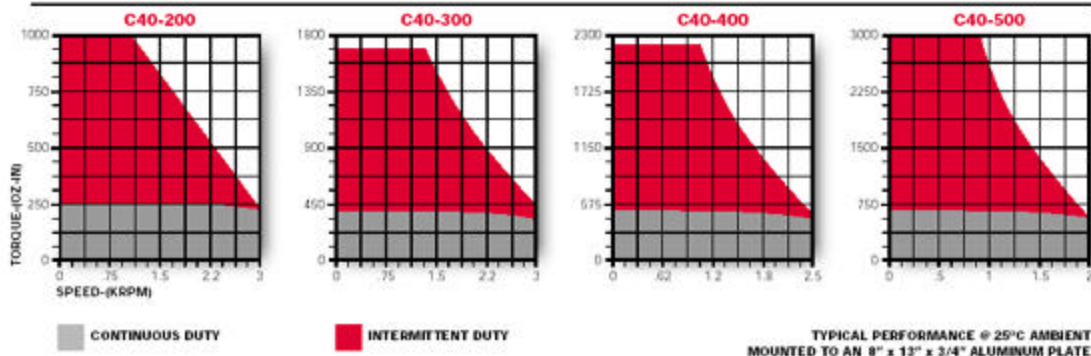
FRAME SIZE	STACK LENGTH	Peak Stall Torque (Tp) oz-in	Cont. Stall Torque (Tc) oz-in	Rotor Inertia (Jm) oz-in-sec ²	Friction Torque (Tf) oz-in	Thermal Resistance (Rth) degC/Watt	Max Recommend Speed RPM	Max Winding Temp C°	Elect Time Constant (Te) msec	Length (L) in.	Weight (W) lb.
C40 - 200		1200	248	.16	12	2.0	3,000	155	5.3	5.8	10
C40 - 300		1984	416	.24	14	1.3	3,000	155	5.5	6.8	13
C40 - 400		2480	512	.30	16	.98	2,500	155	5.7	7.8	15
C40 - 500		3040	640	.37	18	.79	2,000	155	5.9	8.8	17

Sample Windings

	C40-200				C40-300				C40-400				C40-500			
	A	C	E	G	A	C	E	G	A	C	E	G	A	C	E	G
Torque Constant (Kt) oz-in/amp	15.2	26.4	40.8	64.4	23.0	39.5	62.2	98.4	30.4	46.1	73.3	122.4	38.0	59.5	94.1	152.2
Voltage Constant (Ke) Volts/Krpm	11.2	19.5	30.2	47.6	17.0	29.2	46.0	72.7	22.4	34.1	54.2	90.5	28.1	44.0	69.6	112.5
Arm. Resistance (Ra) Ohms (cold)	.14	0.5	1.1	2.3	0.2	0.6	1.4	3.0	.28	.7	1.8	4.4	.35	.85	2.1	5.5
Peak Current (A) Amps	70	45	28	18	80	48	32	20	80	50	32	20	75	50	30	20
Cont. Current (A) Amps	15.6	10	6.3	4.0	17.3	11.1	7.0	4.4	17.0	10.7	6.8	4.3	17	14.5	6.8	4.3

CONSULT MAGMOTOR APPLICATION STAFF FOR OTHER AVAILABLE WINDINGS

▼ Performance Curves



Series M21 Encoder



- Modular, Incremental Encoder for Stepper and Small Servo Motor Feedback
- Phased Array Sensor Technology Provides High Temperature and Operating Frequency and Allows 0.020" (0.5 mm) of Axial Play
- Resolutions to 2048 PPR with Index Standard; Optional 4, 6, or 8 Pole Commutation Tracks for Brushless Servo Motors
- Easy Installation and Removal without Special Tools or Parts

The Dynapar brand M21 modular encoder provides high-performance, cost effective feedback for stepper and servo motor controls.

Using industry standard package dimensions, the M21 is easily installed onto the motor without time-consuming adjustments or special tools. Its unique mechanical design automatically centers and gaps the disc during installation.

For Brushless DC (BLDC) servo control, optional 3 phase commutation tracks replace the traditional Hall Effect sensors. These optically-generated signals provide higher accuracy and reliability, improving the performance and reliability of the servo system.

! **Dynapar Exclusive:** The M21 design operates up to 120°C. The high temperature plastics, phased array sensor, and low current requirements stabilize the output signals over a wide range of input voltage, ambient temperature, or output frequencies.

! **Dynapar Exclusive:** The M21 provides 30 degrees of adjustment to align the signal outputs to the shaft position. Using an industry standard Size 21 modular mounting pattern, the index mark on the disc hub can be coarse aligned to the index sensor position on the housing. The housing rotates to allow further adjustment of the index or fine alignment of the commutation channels to the BLDC motor windings.

! **Dynapar Exclusive:** The M21 enclosure is dirt-tight, rated NEMA 1 / IP50. The cover is gasketed to seal the disc and optics from contamination. Additionally, the base can be sealed to the motor for further environmental protection.

! **Dynapar Exclusive:** The M21 outputs are protected from short circuits, and operate on 5 or 12 VDC power.

SPECIFICATIONS

Electrical	
Code:	Incremental
Resolution:	Incremental: 500 to 2048 pulses per revolution (PPR) Commutation: 2, 3, or 4 pulses per revolution (PPR)
Accuracy:	Incremental: ± 5 arc-mins. max. edge to edge; Commutation: ± 6 arc-mins. max.
Sense: (viewing encoder mounting surface)	Incremental: A leads B by 90° for CCW rotation of motor shaft; Commutation: U leads V, V leads W by 120° for CW rotation of motor shaft
Phasing:	Incremental: $90^\circ \pm 18^\circ$ electrical Commutation: 8 Pole: 30° ; 6 Pole: 40° ; 4 Pole: 60° mechanical Index to U Channel: $\pm 1^\circ$ mechanical - Index center to U channel edge
Symmetry:	Incremental: $180^\circ \pm 18^\circ$ electrical Commutation: 8 Pole: 45° ; 6 Pole: 60° ; 4 Pole: 90° mechanical
Index Pulse Width:	$180^\circ \pm 36^\circ$ electrical (Gated with B low) standard
Input Power Requirements:	Incremental: 5 or 12 VDC $\pm 10\%$ at 100 mA max. (excluding output load); Incremental w/Commutation: 5 or 12 VDC $\pm 10\%$ at 75 mA max. (excluding output load)
Output Signals:	ET7272 Line Driver: 40 mA sink/source max.; Open Collector w/2.0 k ohm pull-ups: 16 mA sink max.
Frequency Response :	200 kHz min.
Termination:	Connector: PCB mounted dual row head with 0.1" x 0.1" pin spacing, 10 pins (incremental only), 14 pins (w/commutation); Cable: conductors - 28 AWG, stranded (7/36), insulation - black, PVC; Shield: aluminum/ polyester foil plus tinned, copper drain wire (28 AWG, 7/36)
Noise Immunity:	Conforms to EN50082-1 Light Industrial for Electro-Static Discharge, Radio Frequency Interference, Electrical Fast Transients, Conducted Interference, and Magnetic Fields (for models or applications with shielded cable)

Mechanical

Weight:	Connector: 1 oz. (28 gm) typ. Connector w/cover: 1.5 oz. (43 gm) typ. Cable: 2.5 oz (71 gm) typ. Cable w/cover: 3.0 oz. (85 gm) typ.
Dimensions:	Outside Diameter: 2.1" (53 mm) max. w/cover, 2.0" (51 mm) max. without cover; Height: 0.8" (20.3 mm) max. (w/cover, excluding connector); Emitter to Detector Gap: 0.070" (1.8 mm) min.
Material:	Base, Housing, & Cover: high temperature, glass filled polymer; Hub: Aluminum; Disk: 0.030" thick glass
Finish:	Base & Housing: black; Cover: RAL 7010 (dark gray)
Moment of Inertia:	6.64×10^{-5} in-oz sec. ² (4.7 gm-cm ²)
Hub Diameters:	1/4", 3/8", 7/16", 1/2", 6 mm, 8 mm, 10 mm, 12 mm nominal
Hub Dia. Tolerance:	+0.001"/-0.000" (+0.026 mm/-0.000 mm)
Mating Shaft Length:	0.45" (12 mm) min.; blind hub lamp screw, 0.65" (16.5 mm) exposed hub clamp screw; 0.75" (19 mm) max. inside cover
Mating Shaft Runout:	0.002" (0.05 mm) max. (Includes shaft perpendicularly to mounting surface)
Motor Shaft Endplay:	+0.005"/-0.015" (+0.13 mm/-0.38 mm) nominal ("+" indicates away from mounting face)
Mounting:	Base: (2) #4-40 (M2.5) #1 Phillips fillister head cap screw on 1.812" (46 mm) B.C., 0.01" (0.254 mm) true position to shaft. Shaft: split hub w/collar clamp, #2-56 hex socket cap screw (5/64" hex wrench included)
Electrical/Mechanical Alignment Range:	± 15° mechanical
Acceleration:	100,000 rad/sec. ² max.
Velocity:	12,000 RPM max.

Environmental

Operating Temperature:	-40° to +120°C
Storage Temperature:	-40° to +85°C
Shock:	50 G's for 11 msec. duration
Vibration:	2.5 G's at 5 to 2000 Hz
Relative Humidity:	90% non-condensing
Enclosure Rating:	NEMA 1/IP50 dirt-tight (for models with cover)

APPENDIX B

JOHN CHRIST'S DRAWINGS FOR THE VEHICLE

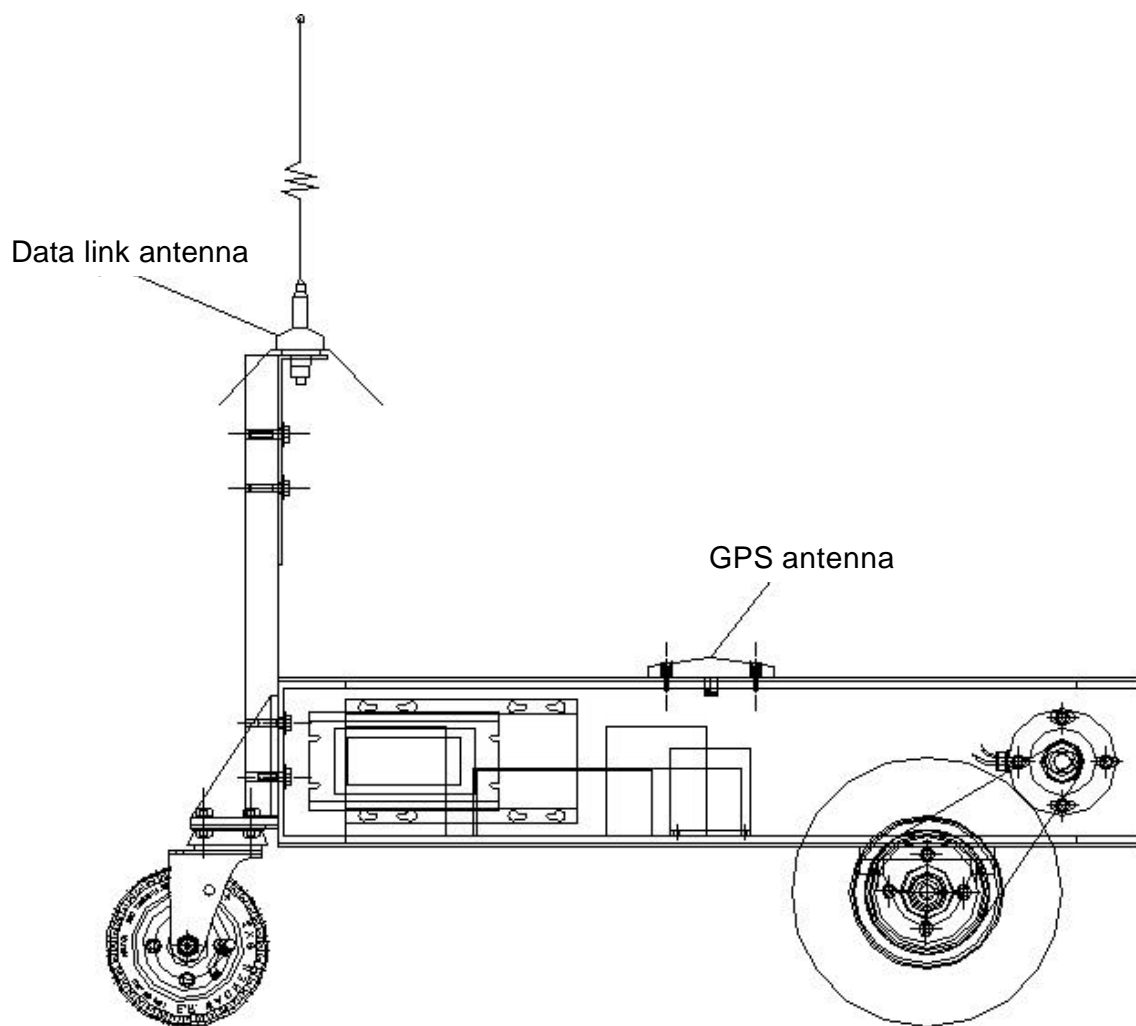


Figure B.1. Leonard Assembly, Side View (Drawing Courtesy of John Christ)

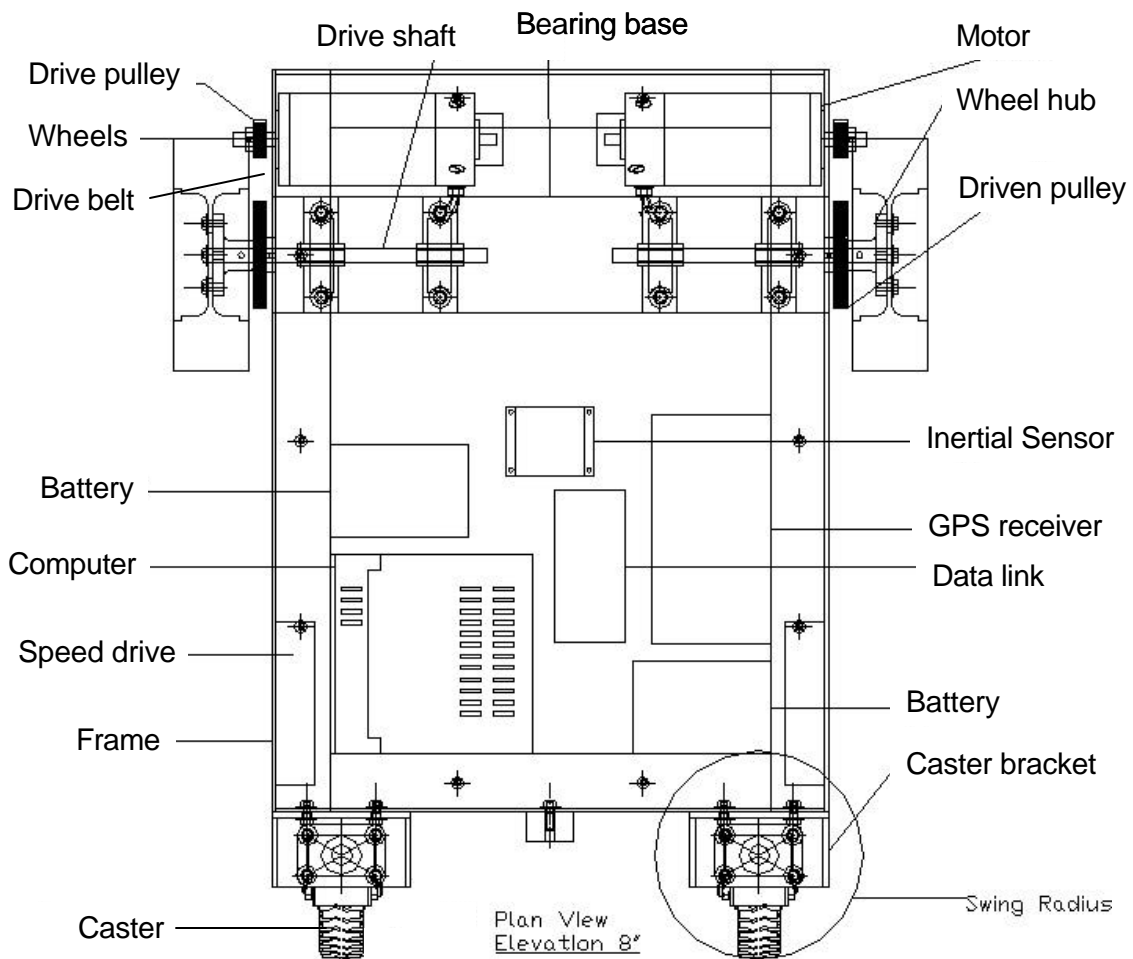


Figure B.2. Leonard Assembly, Top View (Drawing Courtesy of John Christ)

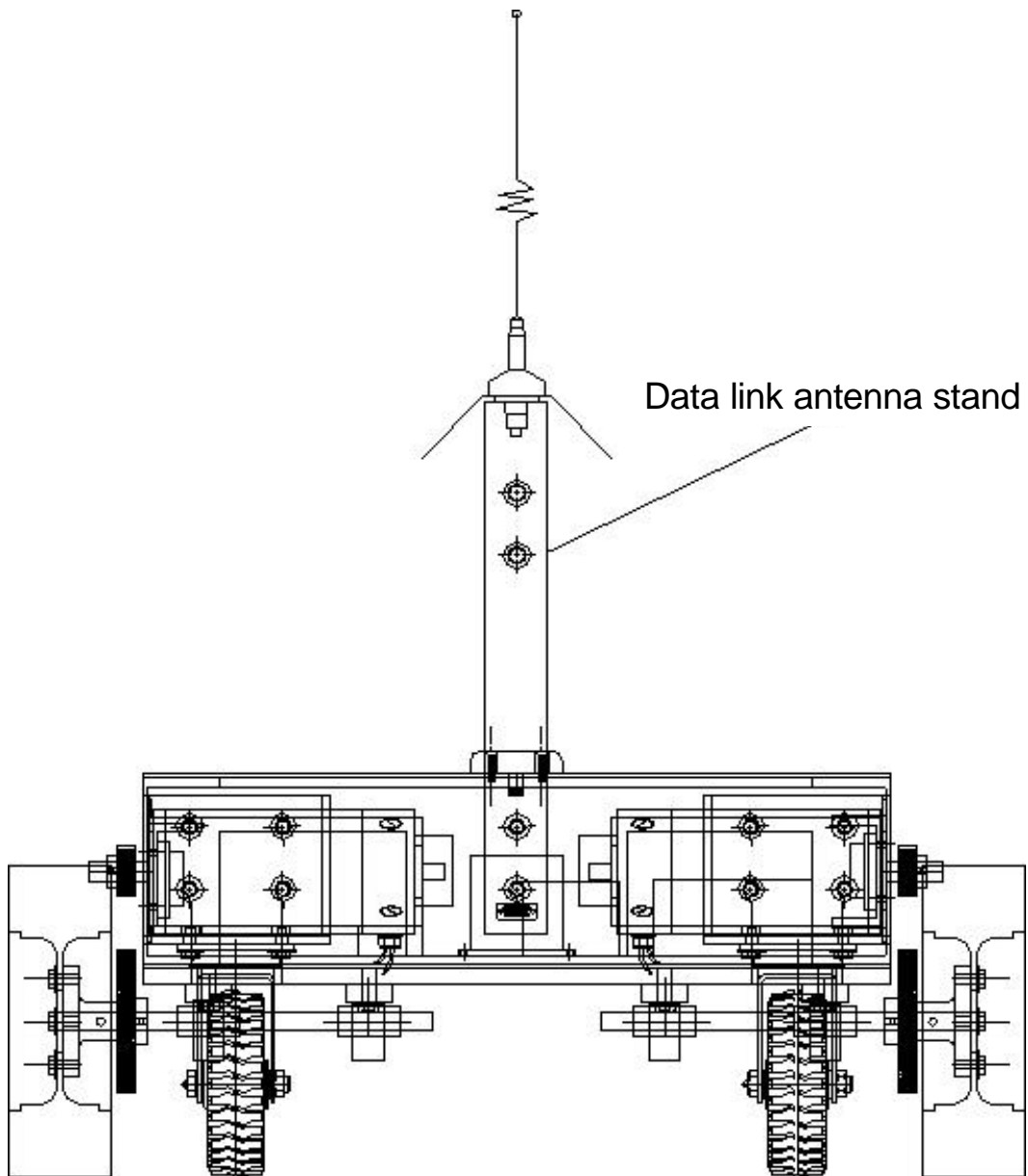


Figure B.3. Leonard Assembly, Front View (Drawing Courtesy of John Christ)

APPENDIX C
VERIFICATIONS OF THE DYNAMIC MODEL

The equations (12), (14) and (21) from Section 3.1.1.3 are confirmed using Lagrange's method and to Kane's equations:

With Lagrange's equations:

Leonard is subjected to non-holonomic constraints and to non conservative forces. The three generalized coordinates are:

$$\begin{aligned} q_1 &= x \\ q_2 &= y \\ q_3 &= \phi \end{aligned}$$

where x , and y define the position of the control point C , and ϕ is the heading angle.

Calculation of the Lagrangian:

- Kinetic energy of the half cylinder:

$$\overline{\omega^B} = -\dot{\phi} \hat{i}_3 \quad \text{and} \quad \overline{J_{B^*}^B} \otimes J_{zz} = \frac{1}{12} m (L^2 + W^2)$$

where $\overline{J_{B^*}^B}$ is the inertia dyadic of body B at B^* , and J_{zz} is the moment of inertia of body B at B^* about \hat{i}_3 .

$$(1) \rightarrow \overline{V^{B^*}} = \begin{bmatrix} \hat{e} & \dot{x} \cos \phi - \dot{y} \sin \phi + \dot{\phi} L_B & \dot{u} \\ \hat{e} & \dot{x} \sin \phi + \dot{y} \cos \phi & \dot{u} \\ \hat{e} & 0 & \dot{u}_s \end{bmatrix}$$

$$\text{Therefore, as} \quad T = \frac{1}{2} m \overline{V^{B^*}} \cdot \overline{V^{B^*}} + \frac{1}{2} \overline{\omega^B} \cdot \overline{J_{B^*}^B} \cdot \overline{\omega^B},$$

the kinetic energy is:

$$T = \frac{1}{2} m (\dot{x}^2 + \dot{y}^2 + \dot{\phi}^2 L_B^2 + 2(\dot{x} \dot{\phi} L_B \cos \phi - \dot{y} \dot{\phi} L_B \sin \phi)) + \frac{1}{2} \dot{\phi}^2 J_{zz} \quad (C.1)$$

- Potential energy: $V = 0$ (flat surface) (C.2)

→ As $L = T - V$, we find out that the Lagrangian is (using (C.1) and (C.2)):

$$L = \frac{1}{2} m (\dot{x}^2 + \dot{y}^2) + m L_B \dot{\phi} (\dot{x} \cos \phi - \dot{y} \sin \phi) + \frac{1}{2} \dot{\phi}^2 (J_{zz} + m L_B^2) \quad (C.3)$$

Constraint equation: We obtain the same constraint equations as before (written in velocity form):

$$(21) \rightarrow \dot{x} \cos \phi - \dot{y} \sin \phi + L_A \dot{\phi} = 0$$

In other words, using the appropriate notations for Lagrange's method, the constraint coefficients relative to this equation for each generalized coordinate are:

$$a_x = \cos \phi, \quad a_y = -\sin \phi, \quad a_\phi = L_A$$

Using the standard form of the Lagrange's equations:

$$\frac{d}{dt} \frac{\partial \mathbf{L}}{\partial \dot{\mathbf{q}}_k} - \frac{\partial \mathbf{L}}{\partial \mathbf{q}_k} = Q_k^{\text{NC}} + \sum_{j=1}^m \dot{\lambda}_j a_{jk}$$

Referring to the (Figure 3.3), we may note that the system is subjected to the non contributing constraint forces F_{NR} and F_{NL} (we have: $F_{\text{N}} = F_{\text{NR}} + F_{\text{NL}}$) and to the forces exerted by the ground on each driving wheel (F_{R} and F_{L}) which are non conservative. Therefore, we have to introduce the Lagrange multiplier (λ) to deal with the non-holonomic constraint:

$$\frac{d}{dt} \frac{\partial \mathbf{L}}{\partial \dot{\mathbf{q}}_k} - \frac{\partial \mathbf{L}}{\partial \mathbf{q}_k} = Q_k^{\text{NC}} + \lambda a_k \quad (\text{C.4})$$

for the first generalized coordinate. Using (C.3), we obtain:

$$\begin{aligned} \bullet \quad \frac{\partial \mathbf{L}}{\partial \dot{x}} &= m \left(\dot{x} + \dot{\phi} L_B \cos \phi \right) \\ \bullet \quad \frac{d}{dt} \frac{\partial \mathbf{L}}{\partial \dot{x}} &= m \left(\ddot{x} + \ddot{\phi} L_B \cos \phi - \dot{\phi}^2 L_B \sin \phi \right) \end{aligned} \quad (\text{C.5})$$

$$\bullet \quad \frac{\partial \mathbf{L}}{\partial x} = 0 \quad (\text{C.6})$$

Finally, substituting (C.5) and (C.6) into (C.4) (and dividing by m),

$$m \left(\ddot{x} + \ddot{\phi} L_B \cos \phi - \dot{\phi}^2 L_B \sin \phi \right) = Q_x^{\text{NC}} + \lambda \cos \phi \quad (\text{C.7})$$

for the second generalized coordinate. Using (C.3), we obtain:

$$\begin{aligned} \bullet \quad \frac{\partial \mathbf{L}}{\partial \dot{y}} &= m \left(\dot{y} - \dot{\phi} L_B \sin \phi \right) \\ \bullet \quad \frac{d}{dt} \frac{\partial \mathbf{L}}{\partial \dot{y}} &= m \left(\ddot{y} - \ddot{\phi} L_B \sin \phi - \dot{\phi}^2 L_B \cos \phi \right) \end{aligned} \quad (\text{C.8})$$

$$\bullet \quad \frac{\partial \mathbf{L}}{\partial y} = 0 \quad (\text{C.9})$$

Finally, substituting (C.8) and (C.9) into (C.4) (and dividing by m),

$$m \left(\ddot{y} - \ddot{\phi} L_B \sin \phi - \dot{\phi}^2 L_B \cos \phi \right) = Q_y^{\text{NC}} - \lambda \sin \phi \quad (\text{C.10})$$

for the third generalized coordinate. Using (C.3), we obtain:

$$\begin{aligned} \frac{\mathbf{1}L}{\mathbf{1}\dot{\phi}} &= mL_B (\dot{x}\cos\phi - \dot{y}\sin\phi) + \dot{\phi}(J_{zz} + mL_B^2) \\ \frac{d}{dt} \frac{\mathbf{1}L}{\mathbf{1}\dot{\phi}} &= mL_B (\ddot{x}\cos\phi - \ddot{y}\sin\phi - \dot{\phi}(\dot{x}\sin\phi + \dot{y}\cos\phi)) + \ddot{\phi}(J_{zz} + mL_B^2) \end{aligned} \quad (C.11)$$

$$\frac{\mathbf{1}L}{\mathbf{1}\dot{\phi}} = -mL_B \dot{\phi}(\dot{x}\sin\phi + \dot{y}\cos\phi) \quad (C.12)$$

Finally, substituting (C.11) and (C.12) into (C.4),

$$mL_B (\ddot{x}\cos\phi - \ddot{y}\sin\phi) + \ddot{\phi}(J_{zz} + mL_B^2) = Q_\phi^{NC} + \lambda L_A \quad (C.13)$$

Calculation of the non-conservative forces: For each generalized coordinate, we have:

$$Q_k^{NC} = \overrightarrow{F}^{NC} \times \frac{\mathbf{1}^I \overrightarrow{V}^{B*}}{\mathbf{1}\dot{q}_k} + \overrightarrow{M}_{B*}^{NC} \times \frac{\mathbf{1}^I \overrightarrow{\omega}^B}{\mathbf{1}\dot{q}_k} \quad (C.14)$$

Recall the Figure 3.3 Section 3.1.1.2. Assume:

\overrightarrow{F}^{NC} is the resultant of all external non conservative forces applied on body B,
(here: $\overrightarrow{F}^{NC} = (\overrightarrow{F}_R + \overrightarrow{F}_L) \overline{s}_2$)

$\overrightarrow{M}_{B*}^{NC}$ is the moment due to the external active forces and torques acting on body B
(here, $\overrightarrow{M}_{B*}^{NC} = \frac{W}{2} (\overrightarrow{F}_R - \overrightarrow{F}_L) \overline{s}_3$)

for the first generalized coordinate. From (C.14) and using (1), we have:

$$\begin{aligned} \frac{\mathbf{1}^I \overrightarrow{V}^{B*}}{\mathbf{1}\dot{x}} &= \cos\phi \overline{s}_1 + \sin\phi \overline{s}_2 \\ \overrightarrow{F} &= (\overrightarrow{F}_R + \overrightarrow{F}_L) \overline{s}_2 \\ \frac{\mathbf{1}^I \overrightarrow{\omega}^B}{\mathbf{1}\dot{x}} &= \overline{0} \end{aligned}$$

Therefore:
$$Q_x^{NC} = (\overrightarrow{F}_R + \overrightarrow{F}_L) \sin\phi \quad (C.15)$$

for the second generalized coordinate. From (C.14) and using (1), we have:

- $\frac{\mathbf{1}^I \overline{\mathbf{V}^{B*}}}{\mathbf{1}^I \dot{\mathbf{y}}} = -\sin \phi \overline{\mathbf{s}}_1 + \cos \phi \overline{\mathbf{s}}_2$
- $\overline{\mathbf{F}} = (\mathbf{F}_R + \mathbf{F}_L) \overline{\mathbf{s}}_2$
- $\frac{\mathbf{1}^I \overline{\boldsymbol{\omega}^B}}{\mathbf{1}^I \dot{\mathbf{y}}} = \overline{\mathbf{0}}$

Therefore:
$$Q_y^{\text{NC}} = (\mathbf{F}_R + \mathbf{F}_L) \cos \phi \quad (\text{C.16})$$

for the third generalized coordinate. From (C.14) and using (1), we have:

- $\frac{\mathbf{1}^I \overline{\mathbf{V}^{B*}}}{\mathbf{1}^I \dot{\phi}} = L_B \overline{\mathbf{s}}_1$
- $\overline{\mathbf{F}} = (\mathbf{F}_R + \mathbf{F}_L) \overline{\mathbf{s}}_2$
- $\frac{\mathbf{1}^I \overline{\boldsymbol{\omega}^B}}{\mathbf{1}^I \dot{\phi}} = -\overline{\mathbf{s}}_3$
- $\overline{\mathbf{M}}_{B*} = \frac{W}{2} (\mathbf{F}_R - \mathbf{F}_L) \overline{\mathbf{s}}_3$

Therefore:
$$Q_\phi^{\text{NC}} = -\frac{W}{2} (\mathbf{F}_R - \mathbf{F}_L) \quad (\text{C.17})$$

Calculation of the generalized constraint forces: For each generalized coordinate, we have:

$$C_k = \dot{\mathbf{a}} \sum_{j=1}^m \lambda_j a_{jk} \quad (\text{C.18})$$

$$C_k = \overline{\mathbf{F}}^C \times \frac{\mathbf{1}^I \overline{\mathbf{V}^{B*}}}{\mathbf{1}^I \dot{\mathbf{q}}_k} + \overline{\mathbf{M}}_{B*}^C \times \frac{\mathbf{1}^I \overline{\boldsymbol{\omega}^B}}{\mathbf{1}^I \dot{\mathbf{q}}_k} \quad (\text{C.19})$$

$\overline{\mathbf{F}}^C$ is the resultant of all external constraint forces applied on body B,
(here : $\overline{\mathbf{F}} = (\mathbf{F}_{\text{NR}} + \mathbf{F}_{\text{NL}}) \overline{\mathbf{s}}_1$)

$\overline{\mathbf{M}}_{B*}^C$ is the moment due to all external constraint forces and torques applied on the body
(here, $\overline{\mathbf{M}}_{B*} = (L_B - L_A) (\mathbf{F}_{\text{NR}} + \mathbf{F}_{\text{NL}}) \overline{\mathbf{s}}_3$)

Note that as we only use \mathbf{F}_{NR} and \mathbf{F}_{NL} as a sum, we assume: $\mathbf{F}_N = \mathbf{F}_{\text{NR}} + \mathbf{F}_{\text{NL}}$

Therefore
$$\overline{\mathbf{F}}^C = F_N \overline{\mathbf{s}}_1 \quad \text{and} \quad \overline{\mathbf{M}}_{B*}^C = (L_B - L_A) F_N \overline{\mathbf{s}}_3$$

for the first generalized coordinate. From (C.18), we have:

$$C_x = \lambda \cos \phi \quad (\text{C.20})$$

From (C.19) and using (1), we have:

- $\frac{\mathbf{1}^I \overline{V^{B^*}}}{\mathbf{1}^I \dot{\mathbf{x}}} = \cos \phi \overline{s_1} + \sin \phi \overline{s_2}$
- $\overline{F^C} = F_N \overline{s_1}$
- $\frac{\mathbf{1}^I \overline{\omega^B}}{\mathbf{1}^I \dot{\mathbf{x}}} = 0$

Therefore: $C_x = F_N \cos \phi \quad (\text{C.21})$

And substituting (C.21) into (C.20): $\lambda \cos \phi = F_N \cos \phi \quad (\text{C.22})$

for the second generalized coordinate. From (C.18) we have:

$$C_y = -\lambda \sin \phi \quad (\text{C.23})$$

From (C.19) and using (1), we have:

- $\frac{\mathbf{1}^I \overline{V^{B^*}}}{\mathbf{1}^I \dot{\mathbf{y}}} = -\sin \phi \overline{s_1} + \cos \phi \overline{s_2}$
- $\overline{F^C} = F_N \overline{s_1}$
- $\frac{\mathbf{1}^I \overline{\omega^B}}{\mathbf{1}^I \dot{\mathbf{y}}} = 0$

Therefore: $C_y = -F_N \sin \phi \quad (\text{C.24})$

And substituting (C.24) into (C.23): $-\lambda \sin \phi = -F_N \sin \phi \quad (\text{C.25})$

for the third generalized coordinate. From (C.18), we have:

$$C_\phi = \lambda L_A \quad (\text{C.26})$$

From (C.19) and using (1), we have:

- $\frac{\mathbf{1}^I \overline{V^{B^*}}}{\mathbf{1}^I \dot{\phi}} = L_B \overline{s_1}$
- $\overline{F^C} = F_N \overline{s_1}$
- $\frac{\mathbf{1}^I \overline{\omega^B}}{\mathbf{1}^I \dot{\phi}} = -\overline{s_3}$
- $\overline{M_{B^*}^C} = (L_B - L_A) F_N \overline{\mathbf{x}_3}$

Therefore: $C_\phi = L_A F_N \quad (\text{C.27})$

And substituting (C.27) into (C.26): $\lambda L_A = L_A F_N \quad (\text{C.28})$

We end up with a set of three equations (C.22), (C.25) and (C.28):

$$\begin{aligned}\lambda \cos \phi &= F_N \cos \phi \\ -\lambda \sin \phi &= -F_N \sin \phi \\ \lambda L_A &= L_A F_N\end{aligned}$$

from which we deduce the value of the Lagrange's multiplier: $\lambda = F_N$ (C.29)

Back to the equations of motion: Substituting (C.15), (C.16) and (C.17) respectively into (C.7), (C.10) and (C.13) and considering (C.29), we end up with three equations of motion:

$$m \left(\ddot{x} + \ddot{\phi} L_B \cos \phi - \dot{\phi}^2 L_B \sin \phi \right) = (F_R + F_L) \sin \phi + F_N \cos \phi \quad (\text{C.30})$$

$$m \left(\ddot{y} - \ddot{\phi} L_B \sin \phi - \dot{\phi}^2 L_B \cos \phi \right) = (F_R + F_L) \cos \phi - F_N \sin \phi \quad (\text{C.31})$$

$$m L_B \left(\ddot{x} \cos \phi - \ddot{y} \sin \phi + \ddot{\phi} L_B \right) + \ddot{\phi} J_{zz} = -\frac{W}{2} (F_R - F_L) + L_A F_N \quad (\text{C.32})$$

Now, we perform the following calculations:

$$(\text{C.33}) = (\text{C.30}) \sin \phi + (\text{C.31}) \cos \phi$$

$$(\text{C.34}) = (\text{C.30}) \cos \phi - (\text{C.31}) \sin \phi$$

$$m \left(\ddot{x} \sin \phi + \ddot{y} \cos \phi - \dot{\phi}^2 L_B \right) = (F_R + F_L) \quad (\text{C.33})$$

$$m \left(\ddot{x} \cos \phi - \ddot{y} \sin \phi + \ddot{\phi} L_B \right) = F_N \quad (\text{C.34})$$

Substituting (C.34) into (C.32) (for F_N):

$$\ddot{\phi} \times J_{zz} = m (L_A - L_B) \left(\ddot{x} \cos \phi - \ddot{y} \sin \phi + \ddot{\phi} L_B \right) - \frac{W}{2} (F_R - F_L)$$

That is:

$$\ddot{\phi} \times \left(J_{zz} - m L_B (L_A - L_B) \right) = m (L_A - L_B) \left(\ddot{x} \cos \phi - \ddot{y} \sin \phi \right) - \frac{W}{2} (F_R - F_L) \quad (\text{C.35})$$

Again, adding the constraint equation (21), we have found the same equations of motion (12),(14) and (21) as with Newton's method.

(12) \rightarrow	$m \left(\ddot{x} \sin \phi + \ddot{y} \cos \phi - \dot{\phi}^2 L_B \right) = (F_R + F_L)$
(14) \rightarrow	$\ddot{\phi} \times \left(J_{zz} - m L_B (L_A - L_B) \right) = m (L_A - L_B) \left(\ddot{x} \cos \phi - \ddot{y} \sin \phi \right) - \frac{W}{2} (F_R - F_L)$
(21) \rightarrow	$\dot{x} \cos \phi - \dot{y} \sin \phi + L_A \dot{\phi} = 0$

With Kane's method:

Kinematics. Again, we use some kinematics derived before:

$$\begin{aligned} \overline{V}^{B*} &= \begin{matrix} \hat{e} & \dot{x}\cos\phi - \dot{y}\sin\phi + \dot{\phi}L_B & \dot{u} \\ \hat{e} & \dot{x}\sin\phi + \dot{y}\cos\phi & \dot{u} \\ \hat{e} & 0 & \dot{u}_s \end{matrix} & \overline{\omega}^B &= -\dot{\phi}\overline{i}_3 \\ \overline{a}^{B*} &= \begin{matrix} \hat{e} & \ddot{x}\cos\phi - \ddot{y}\sin\phi + \ddot{\phi}L_B & \ddot{u} \\ \hat{e} & \ddot{x}\sin\phi + \ddot{y}\cos\phi - \dot{\phi}^2L_B & \ddot{u} \\ \hat{e} & 0 & \ddot{u}_s \end{matrix} & \overline{\alpha}^B &= -\ddot{\phi}\overline{i}_3 \end{aligned}$$

Adding the constraint :

$$\rightarrow (21) \quad \dot{x}\cos\phi - \dot{y}\sin\phi + L_A\dot{\phi} = 0$$

Since we have one constraint, we work with two generalized coordinates selected beyond the three states; we chose y and ϕ . We have:

$$\dot{x} = \dot{y}\tan\phi - \frac{L_A}{\cos\phi}\dot{\phi}$$

Therefore:

$$\overline{V}^{B*} = \begin{matrix} \hat{e} & \dot{\phi}(L_B - L_A) & \dot{u} \\ \hat{e} & \frac{1}{\cos\phi}\dot{y} - \dot{\phi}L_A \tan\phi & \dot{u} \\ \hat{e} & 0 & \dot{u}_s \end{matrix} \quad \overline{\omega}^B = -\dot{\phi}\overline{i}_3$$

Partial Velocities : Deriving the partial velocities and partial angular velocities:

$$\begin{aligned} \overline{V}_\phi^{B*} &= (L_B - L_A)\overline{s}_1 - L_A \tan\phi \overline{s}_2 & \overline{\omega}_\phi^B &= -\overline{i}_3 \\ \overline{V}_y^{B*} &= \frac{1}{\cos\phi}\overline{s}_2 & \overline{\omega}_y^B &= \overline{0} \end{aligned}$$

Generalized Active Force : Recall that the resultant external active (non-conservative) force and momentum:

$$\overline{F}^{NC} = (\overline{F}_R + \overline{F}_L)\overline{s}_2 \quad \overline{M}_{B*}^{NC} = \frac{W}{2}(\overline{F}_R - \overline{F}_L)\overline{s}_3$$

Using the partial velocities, we find out that:

- $$F_\phi = \overline{F}^{\text{NC}} \overline{\mathbf{x}}_{\dot{\phi}}^{\text{B}^*} + \overline{M}_{\text{B}^*}^{\text{NC}} \overline{\boldsymbol{\omega}}_\phi^{\text{B}} = -L_A \tan \phi (F_R + F_L) - \frac{W}{2} (F_R - F_L)$$
- $$F_y = \overline{F}^{\text{NC}} \overline{\mathbf{x}}_y^{\text{B}^*} + \overline{M}_{\text{B}^*}^{\text{NC}} \overline{\boldsymbol{\omega}}_y^{\text{B}} = \frac{1}{\cos \phi} (F_R + F_L)$$

Generalized Inertia Force : Again, we use the differentiated angular momentum with respect to the inertial frame (same derivation as in the Newton Euler's method)

$$\overline{^I \dot{\mathbf{H}}_{\text{B}^*}^{\text{B}}} = \overline{J_{\text{B}^*}^{\text{B}}} \overline{\boldsymbol{\alpha}}^{\text{B}} + \overline{^I \boldsymbol{\omega}}^{\text{B}} \cdot \left(\overline{J_{\text{B}^*}^{\text{B}}} \overline{\boldsymbol{\omega}}^{\text{B}} \right) = -\ddot{\phi} J_{zz} \hat{\mathbf{i}}_3$$

Therefore, we obtain:

- $$F_\phi^* = -m \overline{^I \mathbf{a}}^{\text{B}^*} \overline{\mathbf{x}}_{\dot{\phi}}^{\text{B}^*} - \overline{^I \dot{\mathbf{H}}_{\text{B}^*}^{\text{B}}} \overline{\boldsymbol{\omega}}_\phi^{\text{B}}$$
- $$F_\phi^* = -m \hat{\mathbf{e}}_2 (L_B - L_A) (\ddot{x} \cos \phi - \ddot{y} \sin \phi + \ddot{\phi} L_B) - L_A \tan \phi (\ddot{x} \sin \phi + \ddot{y} \cos \phi - \phi^2 L_B) \hat{\mathbf{u}} - \ddot{\phi} J_{zz}$$
- $$F_y^* = -m \overline{^I \mathbf{a}}^{\text{B}^*} \overline{\mathbf{x}}_y^{\text{B}^*} - \overline{^I \dot{\mathbf{H}}_{\text{B}^*}^{\text{B}}} \overline{\boldsymbol{\omega}}_y^{\text{B}}$$
- $$F_y^* = -m \frac{1}{\cos \phi} (\ddot{x} \sin \phi + \ddot{y} \cos \phi - \phi^2 L_B)$$

Kane's Equations

- for ϕ : $F_\phi + F_\phi^* = 0$ implies:

$$L_A \tan \phi (F_R + F_L) + \frac{W}{2} (F_R - F_L) + m (L_B - L_A) (\ddot{x} \cos \phi - \ddot{y} \sin \phi + \ddot{\phi} L_B) - m L_A \tan \phi (\ddot{x} \sin \phi + \ddot{y} \cos \phi - \phi^2 L_B) + \ddot{\phi} J_{zz} = 0$$
- for y : $F_y + F_y^* = 0$ implies:

$$m (\ddot{x} \sin \phi + \ddot{y} \cos \phi - \phi^2 L_B) = F_R + F_L$$

Substituting the equation for y into the equation for ϕ (for $F_R + F_L$) eliminates the first and fourth terms in the equation for ϕ ; the result is the third equation of the following set of EOMs, the first being (21), the second, Kane's equation for y :

$$\begin{aligned} \ddot{x} \cos \phi - \ddot{y} \sin \phi + L_A \dot{\phi} &= 0 \\ m (\ddot{x} \sin \phi + \ddot{y} \cos \phi - \phi^2 L_B) &= F_R + F_L \\ \frac{W}{2} (F_R - F_L) + m (L_B - L_A) (\ddot{x} \cos \phi - \ddot{y} \sin \phi + \ddot{\phi} L_B) + \ddot{\phi} J_{zz} &= 0 \end{aligned}$$

Finally, isolating the term \ddot{x} in the third equation, and considering the differentiated form of (21), the equations of motion are recovered:

$$\begin{aligned}
 (21) &\rightarrow \dot{x}\cos\phi - \dot{y}\sin\phi + L_A\dot{\phi} = 0 \\
 (12) &\rightarrow m(\ddot{x}\sin\phi + \ddot{y}\cos\phi - \dot{\phi}^2 L_B) = (F_R + F_L) \\
 (14) &\rightarrow \ddot{\phi}(J_{zz} - mL_B(L_A - L_B)) = m(L_A - L_B)(\ddot{x}\cos\phi - \ddot{y}\sin\phi) - \frac{W}{2}(F_R - F_L)
 \end{aligned}$$

BIBLIOGRAPHY

- [Bel99] Bell, T., Precision Robotic Control of Agricultural Vehicles on Realistic Farm Trajectories, PhD Thesis, Stanford University, June 1999.
- [Bry75] Bryson, A. E., Ho, Y.-C. “Optimal Feedback Control”, Applied Optimal Control, Optimization, Estimation and Control, HPC, 1975.
- [Fra98] Franklin, G. F., Powell, J. D., Wokman, M., “Design Using State-Space Methods”, Multivariable and Optimal Control”, Digital Control of Dynamic Systems, Addison Wesley Longman, 1998.
- [Han01] Hannu, M., Outdoor Navigation of Mobile Robots, PhD Thesis, The Finnish Academies of Technology, pp. 1-15, November 2001.
- [Lon00] Longoria, R. G., Modeling of a Permanent-Magnet DC Motor, Lecture Notes, The University of Texas at Austin, Fall 2000.
- [Mis99] Misra, P., Burke, B. P., Pratt, M. M., “GPS Performance in Navigation”, Proceedings of the IEEE, Vol. 87, No. 1, January 1999.
- [Moo98] Moon, F. C., Applied Dynamics, John Wiley and Sons, 1998.
- [O’C97] O’Connor, M., Carrier-Phase Differential GPS for Automatic Control of Land Vehicles, PhD Thesis, Stanford University , December 1997.
- [Pap00] Papadopoulos, E., Poulakakis, J., “Trajectory Planning and Control for Mobile Manipulator Systems”, Proceedings 8th IEEE Mediterranean Conference on Control and Automation, Patras, Greece, July 2000.
- [Slo92] Slocum, A. H., “The Design of a Design Engineer”, Precision Machine Design, Society of Manufacturing Engineers, pp. 24-27, 1992.
- [sTS74] the Technical Staff, The Analytic Sciences Corporation, “Linear Dynamic Systems”, “Optimal Linear Filtering”, Applied Optimal Estimation, Gelb, 1974.
- [Whi97] White, J. R., “Dynamic Model of a Permanent Magnet DC Motor”, System Dynamics, Lecture Notes, Umass-Lowell, Spring 1997.